HYDROLOGICAL PROCESS AND CHARACTERIZATION OF LESSER HIMALAYAN CATCHMENTS

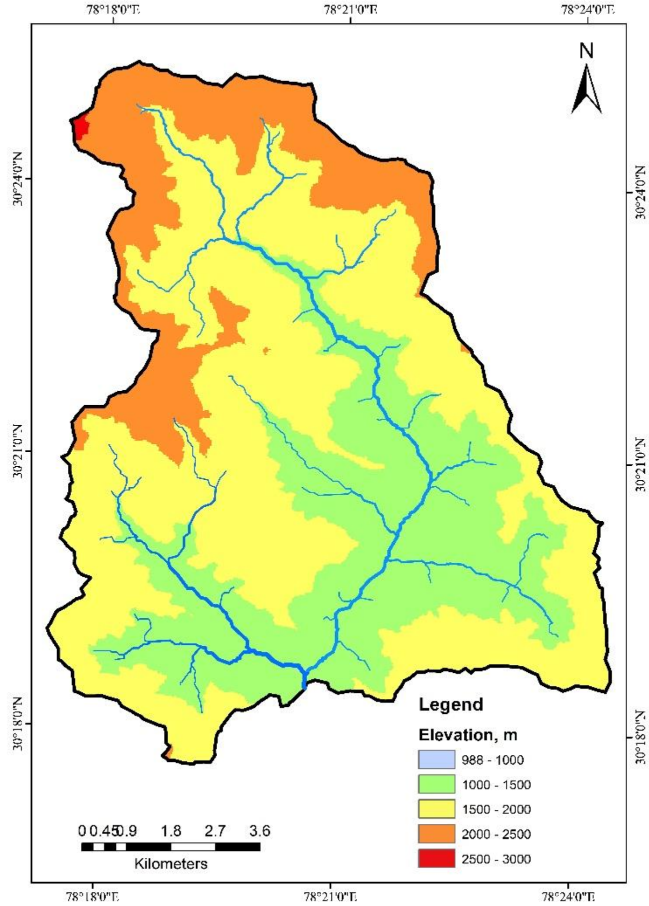

WATER RESOURCES SYSTEMS DIVISION

NATIONAL INSTITUTE OF HYDROLOGY
ROORKEE- 247 667, UTTRAKHAND, INDIA

May 2020

ABSTRACT

This study aims to develop a better understanding of climate-hydrology interaction in the lesser Himalayan experimental catchment. The primary objective of the project was to set up and operate a monitoring facility in lesser Himalayas.

The Hydro-meteorological instrumental monitoring setup was designed and established in the Henval watershed of the Upper Ganga basin within the state of Uttarakhand, situated near Chamba town in Tehri Garhwal district. This filed observatory is intended to measure various hydrological and meteorological variables of a catchment. Two broad crested rectangular weirs have been constructed to measure the discharge at the outlet of two streams namely Henval and Jijali stream. For the continuous monitoring of the water levels at Henval weir an automatic water level recorder (AWLR), has been installed at the outlet of Henval stream. AWLR is a fully computerized, digital and self-contained power source system. Three automatic weather stations (AWS) have been installed in the catchment at the Henval valley at Nagani village on March 23rd, 2016, at Kumargaon village and near the ridge of the catchment at Kanataal effective from January 04th, 2018. One COSMOS sensor has been installed at Nagani AWS location for soil moisture monitoring in the June 2017.

The second objective of the study was the field estimation of evapotranspiration (ET) and comparison with other methods such as RS/SEBAL, FAO56 method and Pan-evaporimeter. Estimation of ET using the field observed meteorological parameters has been carried out using different empirical methods such as FAO recommended Penman-Monteith (Allen et al. 1998), Priestley-Taylor method (Priestley and Taylor 1972), Hargreaves-Samani method (Hargreaves and Samani 1982, 1985), etc. Surface Energy Balance Algorithm for Land (SEBAL), a remote sensing method was also used for the estimation of ET in the catchment. The estimates of actual evapotranspiration using the eddy-covariance method were also compared with the ET computed by above two methods. Various components of water balance have been computed with the help of SWAT model in the Henval watershed.

TABLE OF CONTENTS

LIST OF FIGURES

LIST OF TABLES

CHAPTER 01: INTRODUCTION

1.1 GENERAL

A watershed is a basic unit at which the hydrologic processes are studied and is central to most of the concepts in hydrology. Watershed studies are conducted to understand the fundamental hydrologic and biogeochemical processes and their linkages with soils, vegetation, topography, climate, and management practices worldwide. Managing agricultural or forested watersheds for water quality and quantity improvement and productivity requires a detailed understanding of functional linkages between eco-hydrological processes and management practices. These studies mainly involve modelling the natural processes but the vibrancy of experimental hydrology broadly across the areas of subsurface and surface hydrology, and hydrometeorology still have a unique place of importance and no alternative.

In view of the state of affairs of existing models and studies addressing the problems of watershed hydrology, the significant limitations might be characterized as mainly twofold. First, study basin designs have been limited by the black box concept and many misconceptions (e.g., the linearity, non-heterogeneity, additivity of hydrologic systems, etc. Second, the operation has been substantially bounded by the hydraulic conception of these watersheds as isolated hydrological systems (Wei-Zu et al. 2013). Most of the watershed studies monitor only total runoff at the stream-outlet, and the subsurface responses of the watershed are only estimated by hydrograph separation, etc. These characteristics undermine the formulation of a unified theory of watershed hydrology (Sivapalan et al. 2005) and the development of watershed models (Kirchner, 2006; Mcdonnell et al., 2007). There is a clear need to move beyond the status quo and expand from this narrow hydrological perspective to generate hypotheses governing general behaviour across places and scales, with the ultimate aim to advance the science of hydrology.

In the Himalayan mountains, “naula” (1-2 m deep, approximately lined wells to get water from seepage) and "dhara" (springs) are the primary sources of water for drinking and household consumption. Deforestation, grazing and trampling by livestock, erosion of top fertile soil, forest fires and development activities (e.g. road-widening, mining, building construction, etc.) reduces the infiltration rate and sponge action of the land, which results in the unchecked flow of water during the monsoon to cause sudden swelling of streams and rivers so that there are floods in the foothills and even in the plains, and droughts in the villages located on the slope of the mountains. The difficulty to understand the nature of hilly areas possesses severe limitation on-ground observation. Field experimentation and information collection to develop planning activities for proper planning and management of water resources are therefore necessary.

Hydrological changes experienced by the Himalayan basins are very critical to the water security of the northern Indian plains. Rising temperatures, changing glaciers and reducing snow cover are indicative of the nature of the changing climate of the Himalaya in the recent past (Bhutiyani et al., 2007, 2010). While cryosphere components dictate the hydrology of the higher Himalayan region, the lesser Himalayan regions experience the highest precipitation across the Himalayan slopes. They have a more considerable influence on the basin hydrology. However, the climate- hydrology linkages of this critical region are least known. The climate of the Himalayan slopes is dictated by the orographic forcing and strong linkages between temperature distribution of the mountain slopes and atmospheric saturation conditions by summer/winter monsoon (Thayyen and Dimri, 2014). How these processes are impacting the present and future regional hydrology is the crucial question. Thorough understanding of the coupling between surface hydrologic systems and the overlying atmospheric system under orographic moisture flow is essential to address this question. An experimental research station with state-of-art instrumentation with a long-term research framework is being set up in the lesser Himalayan region to gain understanding on these issues. This research station is aimed to produce baseline data of weather and hydrology of the lesser Himalayan mountains leading to a better understanding of climate-hydrology interaction under changing climate of the region. Since the Himalayan tributaries play an essential role in maintaining the hydrologic regime of the Ganges River; sustained research from this experimental station will help in managing the water resources of Himalayan tributaries of Ganges River under the climate change scenario.

1.2 OBJECTIVES

An experimental setup is proposed in the upper Ganga basin with a significant focus to develop a predictive understanding of the watershed and ecosystems response to changes in climate and land use. Monitoring and modelling evapotranspiration (ET) by using the latest available technology parameterization for the lesser Himalayan region is the core activity. Annual and inter-annual variability of water balance components to be assessed through ground-based hydro-meteorological monitoring. Apart from orographic precipitation, convective precipitation also plays a vital role in governing the microclimatic conditions of a mountainous watershed. Energy balance is considered to be an essential component of forested watershed hydrology. Monitoring soil heat flux in tandem with the net radiation above the canopy is proposed to gain a better understanding of this aspect. Additionally, isotopic samples, water quality samples of surface and groundwater, etc., are also proposed in the experimental set up to create a baseline database on hydrologic variables and processes. Keeping in view the above background, this study has been taken up with the following objectives:

1. To establish an instrumented and experimental setup to measure various hydrological and meteorological variables in a watershed in the upper Ganga basin in the state of Uttarakhand for better understanding of their behaviour and to study the dynamic linkages between the two.
2. To estimate evapotranspiration (ET) by different methods like RS/SEBAL, FAO56 method and actual field measurements and compare the results.
3. To study the various water balance components in the watershed.

The works done during the last five years are presented in this report in subsequent chapters.

CHAPTER 02: STUDY AREA

2.1 GENERAL

A small Himalayan hilly watershed of Henval River up to Devnagar has been selected in the upper Ganga basin in the state of Uttarakhand for the study. This study area consists of paired watersheds, one of them is a forested catchment (undisturbed), and the other one is an agricultural watershed with anthropogenic interventions including a semi-urban habitat at Chamba (Uttarakhand). The geographical extent of the study area is from 30^{0}17’N to 30^{0}26’N latitude and 78^{0}16’E to 78^{0}25’E longitude. This area is a typical representative of a combination of lesser Himalayan hilly temperate climatic conditions with an average annual rainfall range of 1200-1800 mm. The Himalayan subtropical forests yield to a belt of broad temperate leaf and mixed forest mainly comprising of pine forest. The total area under study is 102 km^2 approximately (26 km^2 forested catchment and 76 km^2 the other one) with an elevation range of 999-2676 m. The location map of the watershed within the Upper Ganga Basin is given in Fig. 2.1. The stream in the forested sub-catchment is the source of drinking water for 87 nearby villages. This stream is being pumped 24x7 by the state authorities at its outlet at Devnagar for drinking water supply to the villages.

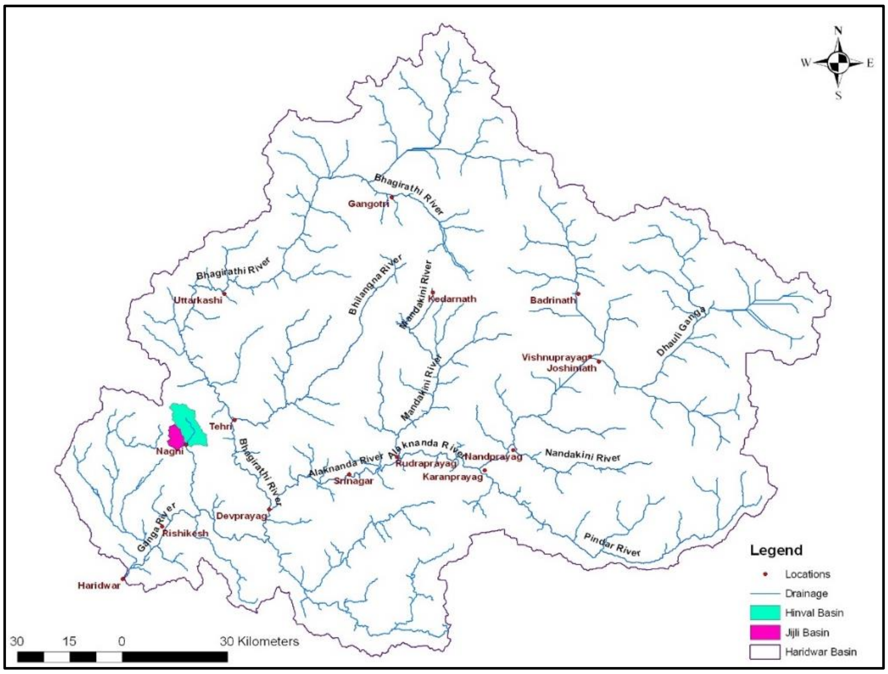

Fig. 2. 1 Location of the Henval watershed up to Devnagar within Upper Ganga Basin

2.2 CLIMATE

The climate of this region is generally humid temperate, but observed variations are attributed to physiographic aspects such as altitude, aspect, slope, drainage condition, vegetation, etc. The valleys are hot in summer and cold in winter. The average temperature generally varies from 3ºC to 30ºC. The average yearly rainfall varies from 1200 to 1800 mm. About 70 to 80% of the rainfall occurs during June and September. The rainfall in the study area starts during May and lasts up to November. It was noticed that the uniformity of rainfall was pronounced from the end of June to mid of September), whereas during the other period rainfall distribution is poor and erratic.

2.3 DIGITAL ELEVATION MODEL

The study area is a representative of the lesser Himalayas. To characterize the topographical features and delineate the catchment boundaries, Shuttle Radar Topographic Mission (SRTM) Digital Elevation Model (DEM) data of 30m spatial resolution has been used. The study area is characterized by very rugged topography, where the elevation ranges from 988m to 2686m (Fig. 2.2). Hypsometric analysis of the study catchments has also been done and presented in Table 2.1 and Fig. 2.3.

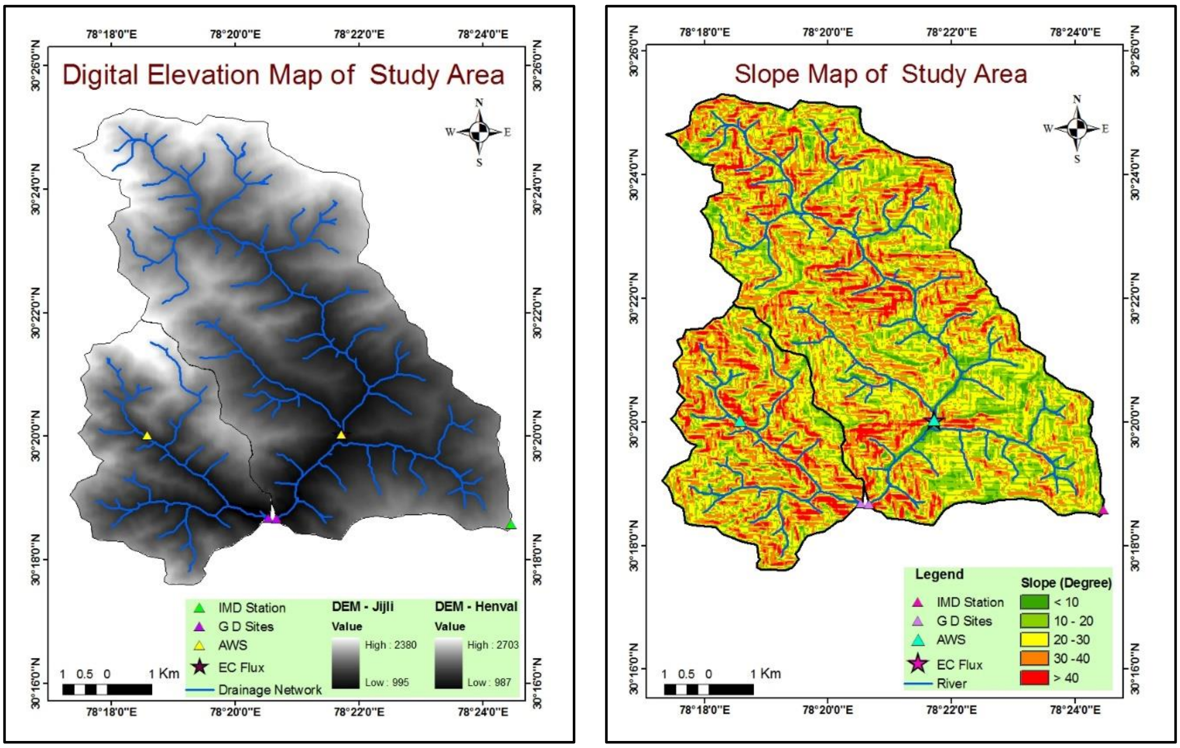

Fig. 2. 2 DEM and Slope Maps of the study Catchments

2.4 LAND USE LAND COVER

The forest is the major land-cover feature of both the catchments. But, Henval catchment is having a considerable coverage of agricultural and fallow land also (the year 2011) which represent considerable human interventions in the catchment, and Jijali catchment is more pristine in nature as compare to Henval. The land use land cover (LULC) maps of both the catchments have been prepared based on the multispectral satellite images of Landsat L8 Operational Land Imager (OLI) at a spatial resolution of 30-meters. LULC map of the watershed classifies the area in 5 different land cover, i.e. Dense forest, open forest, agricultural land, barren land and settlement (human settlement). Change of these land cover type in the course of a decade, i.e. from 2001 to 2011, is analysed in this section.

Table 2. 1 Area under various percentage slope classes for the study catchments

S. No.		The area under slope range (%)	
	Slope Range	Henval	Jijali
1	< 10	6.84	5.77
2	10-20	27.28	21.38
3	20-30	34.82	32.38
4	30-40	22.67	27.94
5	>40	8.40	12.53

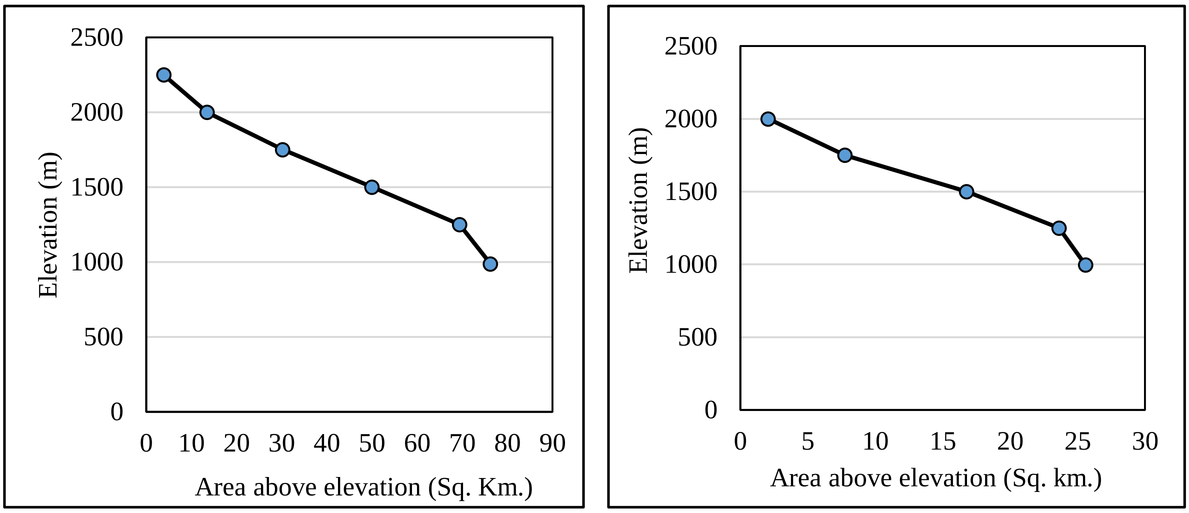

Fig. 2. 3 Hypsometry Curve of Henval (L) and Jijali (R) Catchments

LULC map of Jijali catchment (Fig. 2.4) shows three land cover types in 2001 and four land cover types in 2011. In 2001 Jijali catchment was observed to be cover with three land cover classes which were dense and open forests, and agricultural land. This land cover of three classes evolved to four classes in 2011, which were dense forests, open forests, agricultural land and barren land.

Fig. 2.4 shows an increase in dense forest, agricultural land and barren land, which was compensated with an appreciable decrease in the open forest area. It can be seen from the Table 2.2 that there is a decrease of 24.65%, which is 6.46 km^2 for Jijali catchment from the year 2001 to 2011 in the open forest land. No settlements were captured in both the years 2001 and 2011 on a scale of 30 m pixel size. Barren land also started growing in the higher elevation of the catchments, which have grown from 0% in 2001 to 2.44% in 2011.

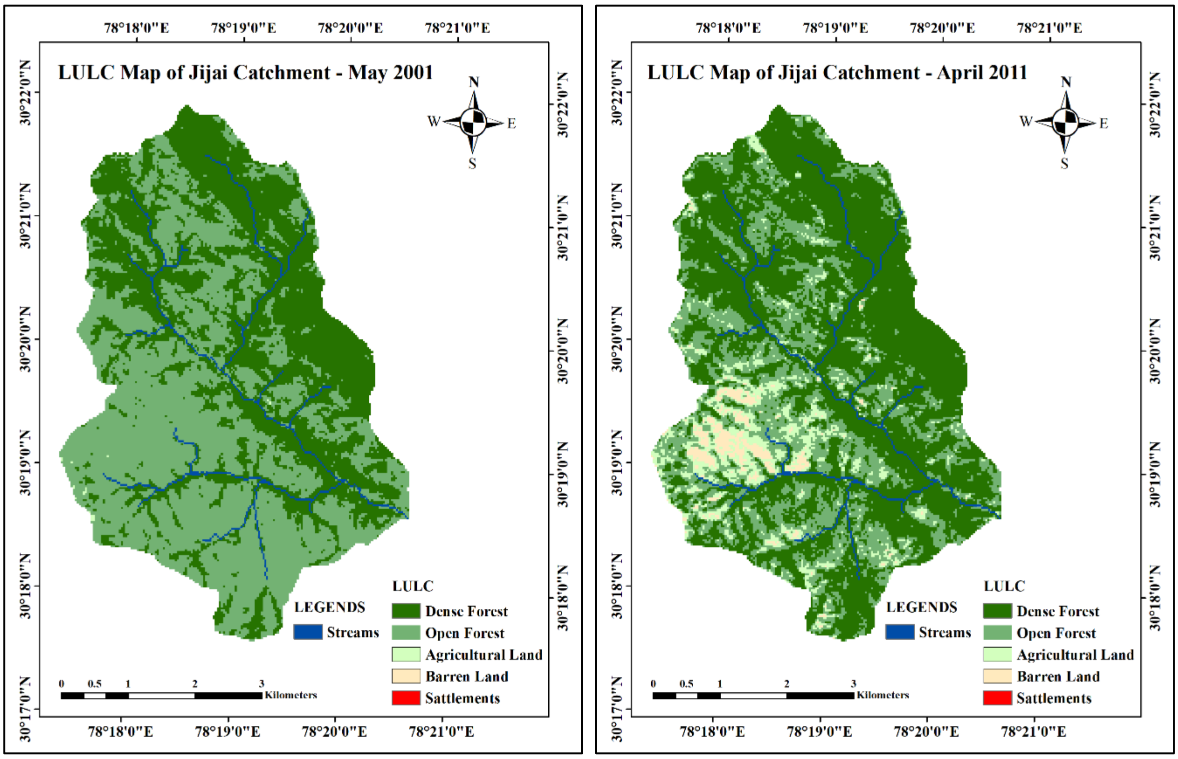

Fig. 2. 4 LULC Maps of the Jijali Catchments for the year 2001(L) and 2011(R)

Table 2. 2 Area of coverage by different land cover within the Jijali catchment

S. No.	Land cover Type	2001 (km^2)	2011 (km^2)	Change Area (km^2)	Change (%)
1	**Dense Forest**	11.76	15.5	3.74	14.27
2	**Open Forest**	14.44	7.98	-6.46	-24.65
3	**Agriculture**	0.02	2.1	2.08	7.94
4	**Barren Land**	0	0.64	0.64	2.44
	Total	26.22	26.22		

LULC map of Henval catchment shows 5 land cover classes (Fig. 2.5). A similar pattern was observed in land cover change like that in Jijali catchment. In Henval catchment also increase in dense forest, agricultural, barren land and land under the settlement was observes which was compensated by the decrease in open forest land.

Table 2.3 indicate the areal corage of various land uses in the year 2001 and 2011. In the year 2011, a decrease of 30.68% was seen in the open forest area, which accounts for 23.24 km^2 of Henval catchment. Approximately similar increases in the dense forest were noticed in both the catchments, i.e. of 15%.

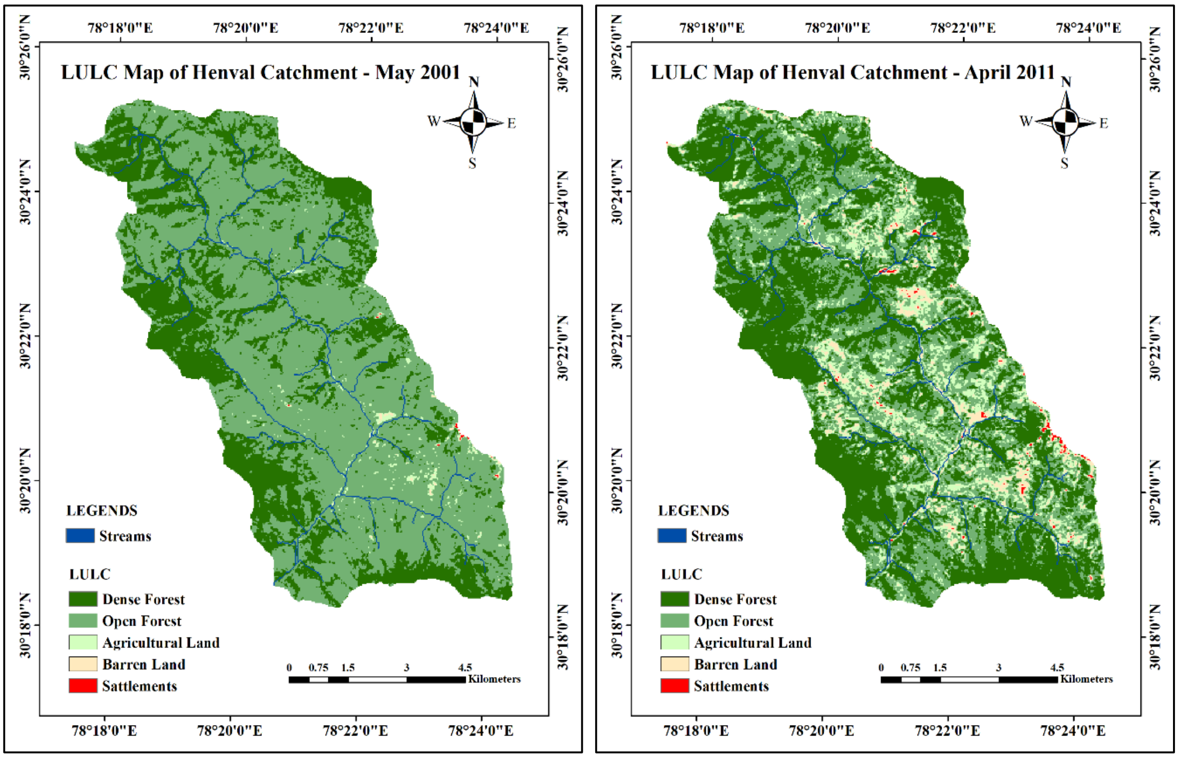

Fig. 2. 5 LULC Maps of the Henval Catchments for the year 2001(L) and 2011(R)

A combined LULC map of both the experimental watersheds is depicted in Fig. 2.6. Watershed, as a whole, shows significant changes from May-2001 to April-2011. All classes excluding open forest land shows an increase in the area. The turnout of the open forest into the dense forest (15.55%, i.e. 15.86 km^2) is the significant change that can be seen over time in the area.

Table 2. 3 Area of coverage by different land cover within the Henval catchment

S. No.	Land cover Type	2001 (km^2)	2011 (km^2)	Change Area (km^2)	Change (%)
1	**Dense Forest**	23.28	35.4	12.11	15.99
2	**Open Forest**	51.57	28.33	-23.24	-30.68
3	**Agriculture**	0.76	8.71	7.95	10.5
4	**Barren Land**	0.12	3.09	2.97	3.92
5	**Settlements**	0.03	0.23	0.21	0.27
	Total	75.76	75.76		

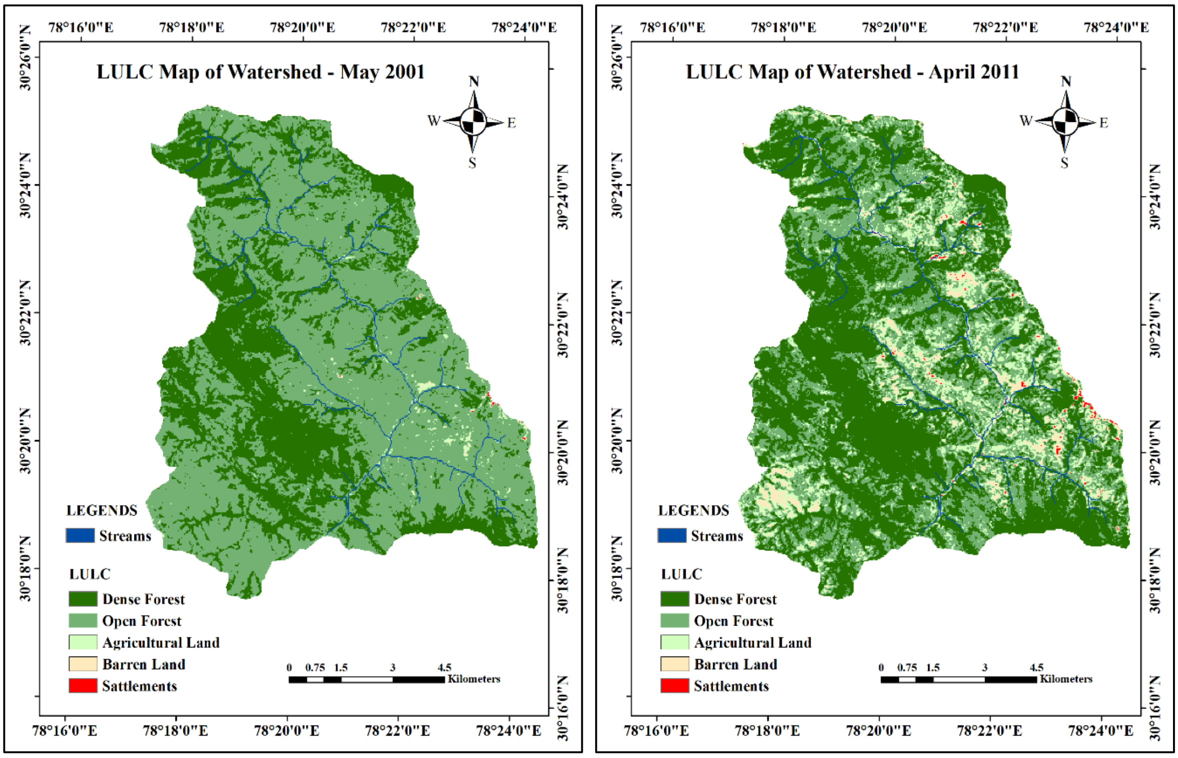

Fig. 2. 6 LULC Maps of the watershed for the year 2001(L) and 2011(R)

Agricultural land, Barren land and Settlements have also increased in the watershed, which is all due to decreased open forest land. The possible reason behind this decrease in open forest land and increase in all other land cover classes can be the unplanned restricted movement of the population in the open forest land for fuel or fodder for their livestock. The reason behind this unplanned restricted movement can be many such as availability of LPG which would limit the fuel consumption from the open forest, increased agricultural area which would help in supplementing food both for the livestock and the population living in the area.

CHAPTER 03: DATA AND INSTRUMENTATION

3.1 GENERAL

One of the primary objectives of the project is to generate various hydro-meteorological datasets for the study catchment for understanding the hydrological and climatic processes and their interactions. An experimental catchment has been designed with various instrumentations and established the project site at Henval catchment was done to achieve this objective.

3.2 CONSTRUCTION OF RECTANGULAR WEIRS

Discharge is an essential component and process of the hydrological cycle. Two broad crested rectangular weirs have been constructed to measure the discharge at the outlet of Henval and Jijali. Guidelines for ideal site selections for discharge monitoring were followed. After a survey of many possible gauging sites, a location near to the Uttarakhand Jal Sansthan (UJS) pumping station was identified for construction of a weir across the perennial stream. It was challenging to construct a permanent structure in a running stream, and the success of the structure depends on the skill of the workers. Construction of weir was done in two phases in the first phase the water was diverted to one side, and RCC work on the other side was completed. After two weeks in the second phase, the other side of the weir was casted with water diversion over the completed part.

The weir at Henval is constructed just upstream of the pedestrian cross-over bridge near the pumping station of UJS at Jijali-Devnagar. The length of the weir is 11m, the height is 1.0m (initially 0.7m), and the width of the crest is 0.5m. The weir at Henval was also provided with one staff gauge to measure the water level in the upstream of the weir.

The weir was operated for one entire year successfully, and it was noticed after the first monsoon that the majority of the weir is laden with the silt, boulders and many river bed materials. Thus, it was creating obstacles for proper monitoring of the water level. The issue was discussed within the project team, and it was decided to raise the height of the weir to one meter from 0.7 meters. Then, the second phase of construction works carried over the same weir, and after that, the monitoring was continued. Fig. 3.1 shows the evolution of the weir at Henval and various phases of its construction.

Fig. 3. 1 Various phases of construction of Weir at Henval

The second weir at Jijali stream of the forested catchment has been constructed about 250m upstream of the confluence of Jijali and Henval. The dimensions of this weir are 11.5m X 0.7m X 0.5m. The various phases of construction of a weir at Jijali area shown in Fig. 3.2. During the field visit on May 04th, 2016 it was found that the soon after its construction Jijali weir is thoroughly water submerged due to a water intake structure constructed by the Uttarakhand Jal Sansthan (UJS) just downstream of the weir. The situation was examined by the team of experts to resolve the issue. But the requisite free-flow condition for the Jijali weir could not be created in that location, so no observations are available fro Jijali weir. Submerged weir is also visible in the Fig. 3.2

Fig. 3. 2 Various phases of construction of Weir at Jijali

3.3 INSTALLATION OF AUTOMATIC WEATHER STATION AT NAGANI

One automatic weather station (AWS) with soil parameters monitoring station has been purchased from Campbell Scientific and installed in the agricultural catchment (Fig. 3.3) near village Nagani at 1090 m a.s.l.. Initially, the data at an interval of 30min were received at NIH servers through FTP from March 23rd, 2016 on a near real-time basis, but due to poor mobile network, it was shifted to email-based reporting. The various sensors their make and accuracy and other installation details are given in Table 3.1.

Table 3. 1 Details of the sensors, their accuracy and installation information plugged in in the AWS and the soil Monitoring Station at Nagani

Sensor	Symbol (Unit)	Make	Height/Depth (m)	Stated accuracy
Data loger		Campbell CR1000	NA	NA
AT/RH: Radiation Shield	Ta (^{0}C) RH (%)	Rotronics-HygroClip2	2.0m	±0.2^{0}C ±1.5% RH
Air temperature/Fan Aspirated	Ta (^{0}C)	Rotronics-HygroClip2	2.0m	±0.2^{0}C
Relative Humidity/ Fan Aspirated	RH (%)	Rotronics-HygroClip2	2.0m	±1.5% RH
Wind Speed	U (m s^{-1})	RM Young 05103-45	2.0, m	±0.3m/s
Wind Direction (WD2.0)	WD (^{0})	RM Young 05103-5	2.0 m	±0.3^0
Wind Speed (WS 63cm)	U (m s^{-1})	RM Young 05103-5	2.0m	±0.3m/s
Wind Direction (WD 63 cm)	WD (^{0})	RM Young 05103-5	2.0 m	±0.3^0
Four Component radiometer	(W m^{-2})	Kipp & Zonen (CNR4)	2.5 m	
Air pressure	hpa	Setra CS100 (500-1100hPa)		±0.3hpa
Rain Gauge	(m)	TE525MM	1.0	±1.0cm
Soil temperature (04 Nos.)	T (^{0}C)	107-L	2.0cm (L, R) 30 cm (L, R)	
Soil Moisture, Temp(TDR) Sensor (05 Nos.)		CS655	6.0 cm (L, R) 15 cm (Centre) 50 cm (Centre) 90 cm (Centre)	
Soil Heat flux plate (02 Nos)	(W m^{-2})	Hukseflux HFP01-L	8.0 cm (L, R)	

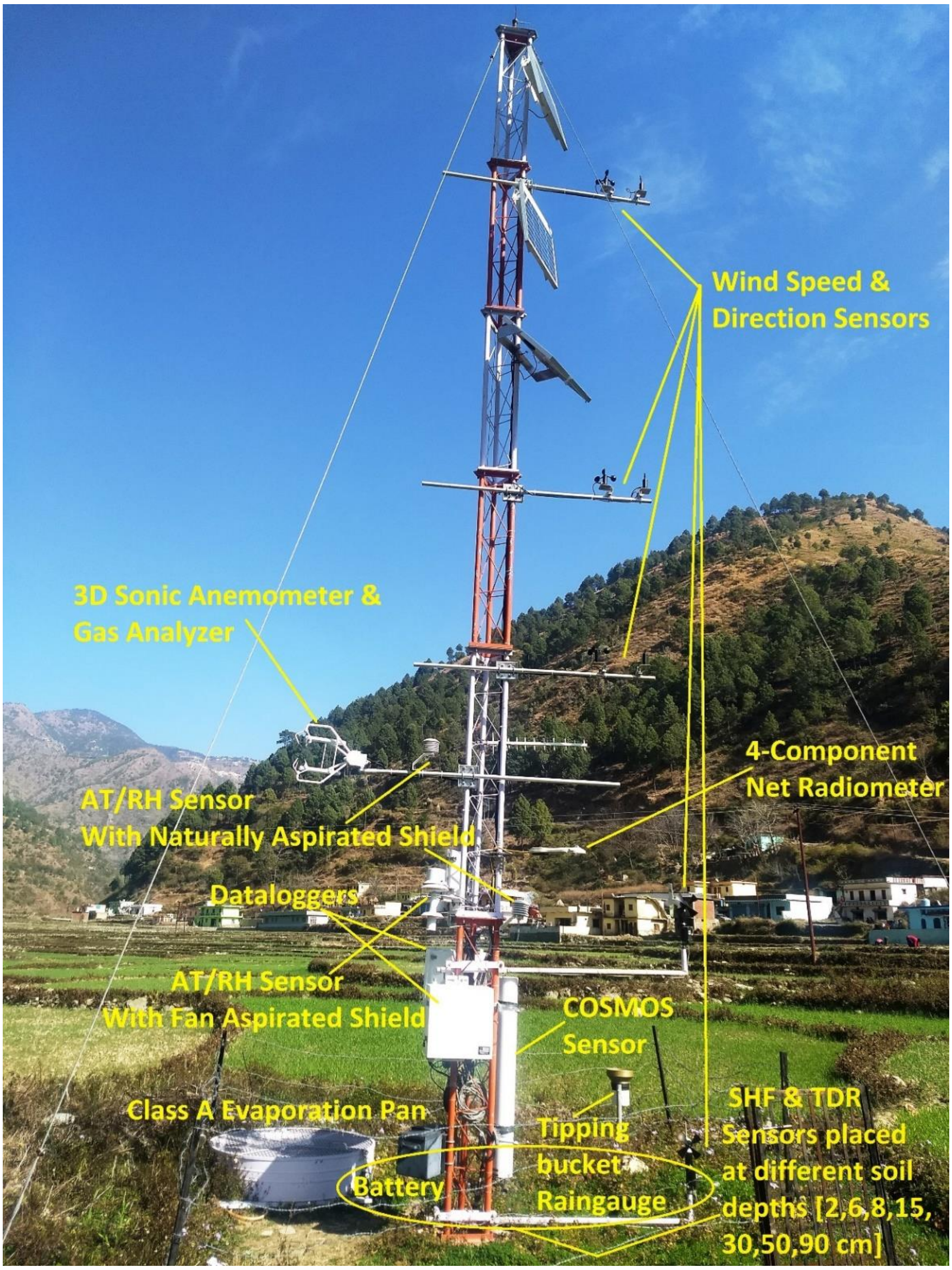

Fig. 3. 3 The automatic weather station (AWS) installed at Henval Catchment

The data received from March 23rd, 2016, has been processed, analysed, and the results are presented in this report.

3.4 INSTALLATION OF AUTOMATIC WEATHER STATION AT KANATAAL

Another automatic weather station (AWS) with soil parameters monitoring station has been procured from a sponsored project (MoES) and installed in the agricultural catchment (Fig. 3.4) at the Research and Extension Centre of Uttarakhand University of Horticulture and Forestry (UUHF), Kanataal (Tehri Garhwal) of on an elevation of 2590 m a.s.l. Meteorological, soil and solar data are being recorded at this AWS at a frequency of 30 min. The installation of this AWS tower was done on January 04th, 2018. The various sensors their make and accuracy and other installation details are given in the Table3.2. However, only the results of the analysis of the data received from AWS tower of Nagani are presented in this report.

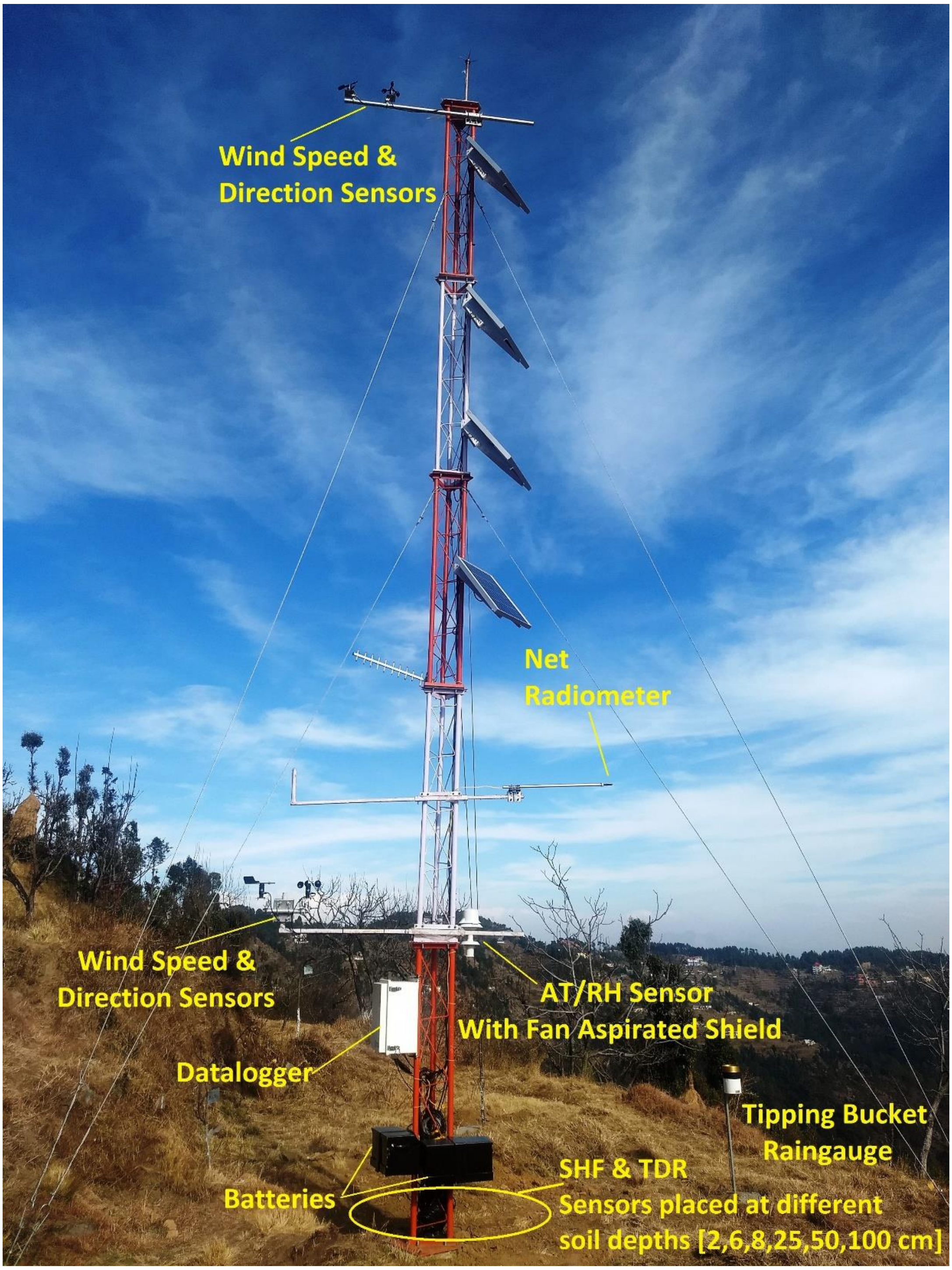

Fig. 3. 4 The automatic weather station (AWS) installed at Kanataal

Table 3. 2 Details of the sensors, accuracy and installation information plugged in the AWS and the soil Monitoring Station at Kanataal

Sensor	Symbol (Unit)	Make	Height/ Depth (m)	Stated accuracy
Data logger	-	Campbell CR3000	NA	NA
AT/RH Sensor	Ta (^{0}C) RH (%)	HC2S3-L-20pt	2 m	±0.1°C ±0.8% RH
Compact Aspirated Shield		43502	2 m	
Net Radiometer	(W m^{-2})	NRLite2	2 m	10 µV W-1 m2
Rain Gauge	(m)	TE-525-L25-PT	1 m	1.0% up to 50 mm/h
Heat Flux Sensor	(W m^{-2})	HFP01-L-25pt	2 m	± 3 % (k = 2)
Barometric Pressure Sensor	Mb	CS-106		±0.3 mb
Soil sensor	Ta (^{0}C)	CS-665-L-66pt	2, 6, 25, 50, 100 m	±0.1°C
Wind Speed Sensor	U (m s^{-1})	FST200-201	2, 10 m	±0.5 m/s
Wind Direction Sensor	WD (^{0})	FST200-202	2, 10 m	±3 °

3.5 INSTALLATION OF AUTOMATIC WATER LEVEL RECORDER (AWLR)

For the measurement of discharge at the outlet of Henval, a weir has been constructed as discussed in section 3.1. An automatic radar type water level recorder with telemetric arrangement has been purchased and installed (Fig. 3.4) to monitor the water levels (head over the weir). It is a non-contact device which looks down toward the river water. The installation of AWLR was not easy. A complete telescopic cantilever with a perpendicular balancing arrangement with stay-wires was fabricated at the NIH workshop. The cantilever transported to the project site and fixed with a masonry civil structure with many humanitarian efforts.

Installation of AWLR is in the upstream of pedestrian cross-over bridge near the pumping station of UJS at Jijali-Devnagar. AWLR is a fully computerized, digital and self-contained power source system, fitted with data logger and battery charging solar panel with rechargeable batteries with sealed waterproof enclosure for the data logger. The data logger is placed on the rooftop of the nearby residential quarter of UJS employee.

Fig. 3. 5 The digital water level recorder (DWLR) installed on the outlet of Henval stream

3.6 EDDY FLUX TOWER

Variables describing the turbulent transport such as three components of the 3-dimensional wind speed (u, v, w), sonic temperature (Ts), the concentration of the gas of interest, and water vapour serves the requirement of eddy covariance method for the computation of evapotranspiration. These measurements have to be fast to be able to compute the gas flux and are captured by an eddy covariance station. The term “fast” usually refers to devices capable of adequately measuring processes at about 10 Hz (10 times per second). The instrumentation consists of a **3-dimensional sonic anemometer** and an **open-path gas analyser**. The gas analyser is usually positioned at or slightly below the sonic anemometer level. The vertical and horizontal separation between the anemometer and other instruments should be kept to a minimum, preferably not exceeding 15 to 20 cm.

3.6.1 Sonic Anemometer (3-Dimensional)

A 3-dimensional sonic anemometer uses 3 pairs of transducers to measure the speed of sound for each pair. Three vector components of wind speed are then computed, and the vertical wind speed component (w) is used for the eddy covariance calculations. The three main types of the physical arrangement of sonic anemometers most used in eddy covariance are:

1. Omni-directional design with u, v and w components measured in the same physical space by non-orthogonal off-axis pairs of transducers (e.g., not at 90° to each other),
2. Non-Omni directional c-clamp design with u, v and w components measured in the same physical space by non-orthogonal pairs of transducers,
3. C-clamp design with u, v and w components measured in the same or different physical spaces by orthogonal transducers, with w measured by a pair of vertically aligned transducers.

3.6.2 Gas Analyser

There are many different ways to measure gas content in the air. These may be based on chemical, electric, optical and other types of technology. However, not all of these measurements are suitable for eddy covariance. In the eddy covariance method, fast fluctuations in atmospheric gas concentration need to be sampled with high resolution at a frequency of about 10 Hz. Chemical sensors are usually too slow for such sampling, and electric sensors generally do not work well with the low concentrations of gases typically found in the atmosphere. Optical analysers, however, can be sufficiently fast for use in eddy covariance, depending on the performance of the specific instruments.

The flux tower arrangement installed at the site in Henval valley contains a 3-D sonic anemometer, i.e**.** **CSAT-3A** by Campbell scientific (Fig 3.3), for the measurements of the turbulent fluctuations of horizontal and vertical wind, and an open-path gas analyser, i.e. **EC 150** by Campbell scientific (Fig 3.3), specially designed for eddy-covariance carbon and water flux measurements. As a stand-alone analyser, it simultaneously measures absolute carbon-dioxide and water-vapour densities, air temperature, and barometric pressure.

Fig. 3. 6 The Eddy covariance sensor installed at Nagani AWS station

CHAPTER 04: BASIC ANALYSIS OF THE DATA

4.1 PREPARATION OF BASE MAP

A base map for the study area has been prepared from the Toposheet No. 53 J/7 on scale 1:50000, acquired from Survey of India (SOI), as shown in Fig. 4.1. The significant features such as the location of villages, roads and their types, river, nature of streams and spot heights are depicted in the map. Henval is the principal river which drains the study area. It mainly flows from north to south. The prepared map is shown in Fig. 4.1

4.2 DELINEATION OF SUB-WATERSHEDS

Shuttle Radar Topographic Mission (SRTM) Digital Elevation Model (DEM) data of 30m resolution obtained from the website of https://lta.cr.usgs.gov/SRTM, has been used to represent topographical characteristics and delineate watersheds within the study area. The study area is characterized by very rugged topography, where the elevation ranges from 988m to 2686m (Fig. 4.2).

The three different watersheds of varying sizes are delineated based on the suggestions of working group members. These are Henval Watershed (75.59km^2), Jijali Watershed (26.02km^2) and Upstream Watershed (28.57km^2), respectively. The primary purpose behind such delineations is to study the effect of land-use types on different hydrological processes under similar hydro-metrological conditions.

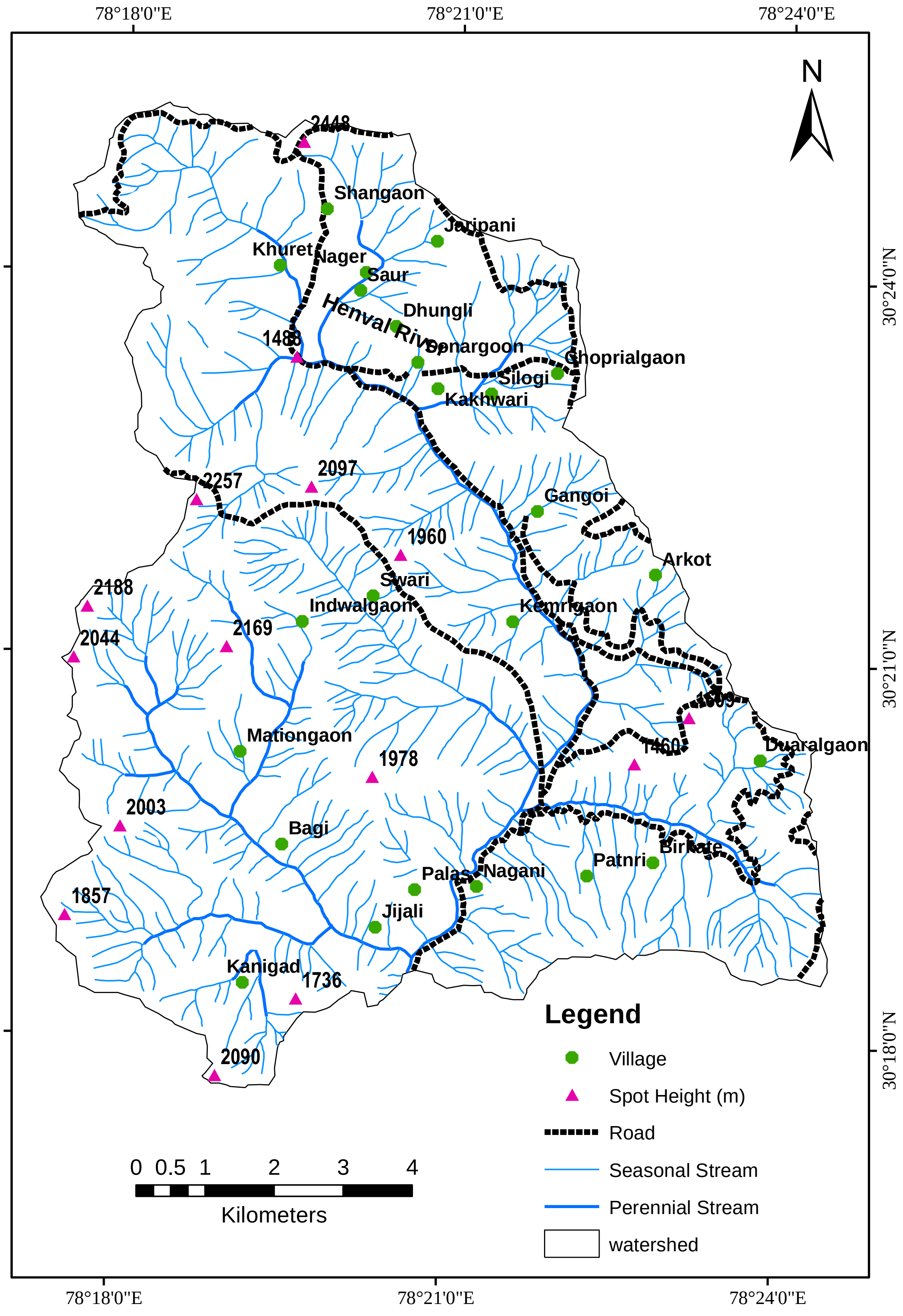

Fig. 4. 1 Base map of the study area

4.3 GENERATION OF STREAM ORDER MAP

A stream order map for the study area has been prepared using Strahler's method, from the SRTM DEM of 1 arc sec resolution under ArcGIS 10 environment (Fig. 4.4). The maximum fourth-order stream is found within the study area.

4.4 VARIATION OF RECORDED VARIABLE AND PARAMETERS AT HENVAL

4.4.1 Air Temperature

The daily, monthly and annual variation of each parameter was computed for Henval site and are discussed in the subsequent sections. The variations of the daily mean value of air temperature (naturally aspirated and fan aspirated) are shown in Fig. 4.4 and monthly mean value are shown in Fig. 4.5, which shows that air temperature is comparatively higher in the months of May to September, which is closely linked to the increase in solar radiation. It is also found more fluctuating during the months of March – June for all the years. The range of the daily mean air temperature is given in table 4.1. It can be seen from the table that there is a significant difference in the values or air temperature from the same sensor but t=with different type of shields. It can be noted from the that the temperature values as lower in case of fan-aspirated shield sensor compared to the naturally aspirated sensor or the radiation shield sensor.

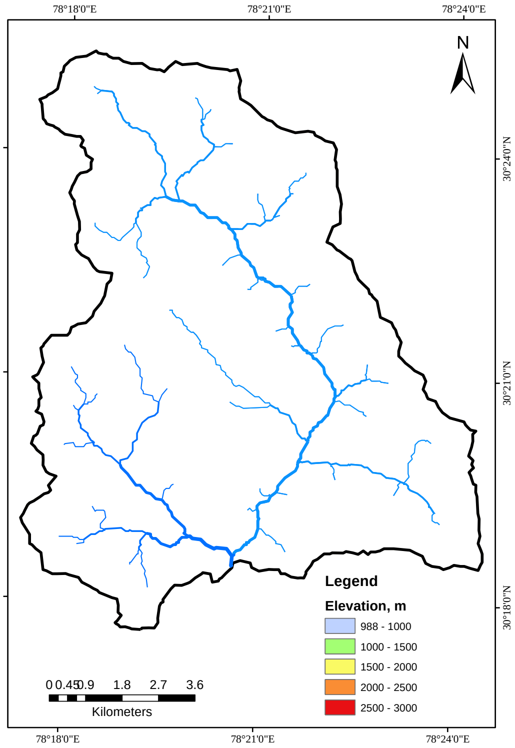

Fig. 4. 2 Map showing the topographical characteristics of the study area

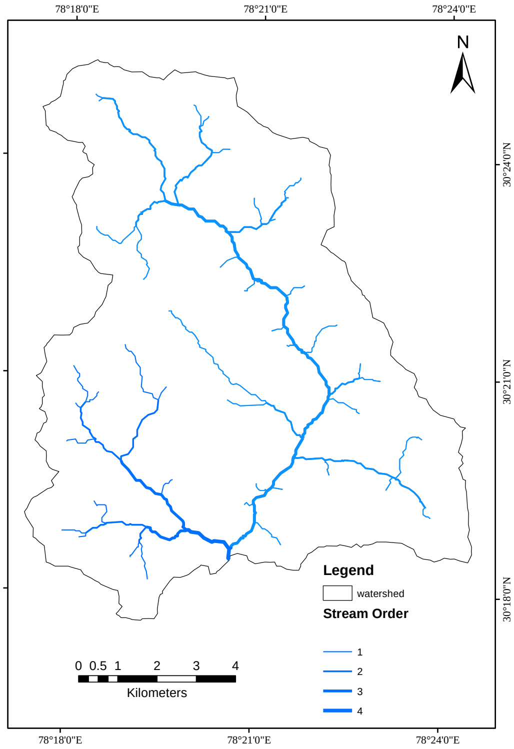

Fig. 4. 3 The Stream order map of the catchment

Table 4. 1 Range of the Air temperature at Henval valley

Air Temperature	Mini. Value (^{0}C)	Maxi. Value (^{0}C)	Average Value (^{0}C)
Naturally Aspirated	4.99	29.86	18.44
Fan Aspirated	4.26	29.82	17.98

4.4.2 Relative Humidity

Similar to the air temperatures, the observations for a relative humidity of air (naturally aspirated and fan aspirated) are obtained and as shown in Fig. 4.6 (daily mean RH) and Fig. 4.7 (mean monthly RH). It is found that relative humidity of air is comparatively higher in the months of July to October. The fluctuations are comparatively higher during the non-monsoon months for all the years. Interannually there is not much variation in the relative humidity, except for the year 2019 which show some more substantial variation, particularly in May and June. The relative humidity varies from 24% to 100% in the Henval valley. Values of relative humidity from the fan-aspirated sensor were found to be a bit higher as compared to the values from naturally aspirated sensors.

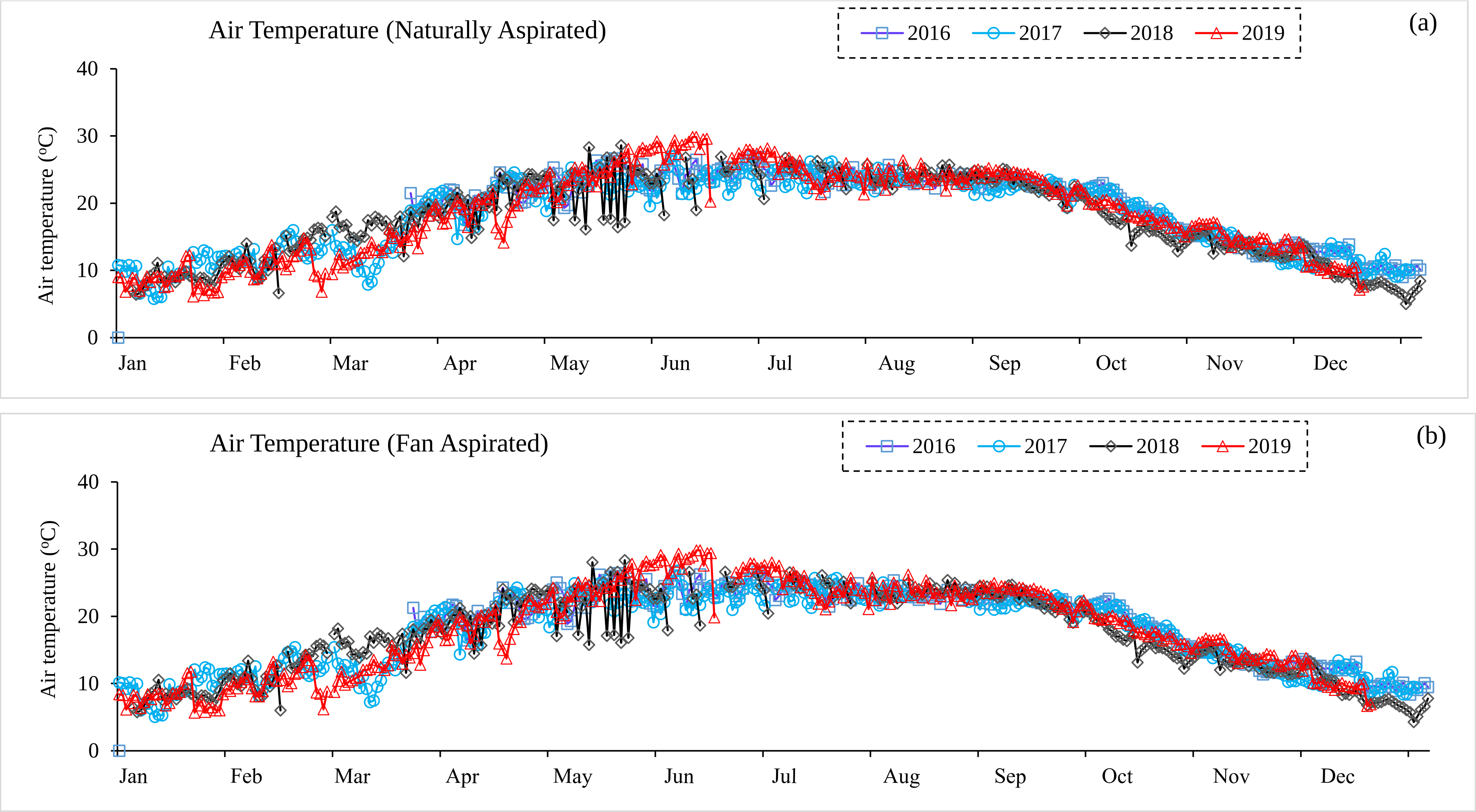

Fig. 4. 4 Variations of the daily mean air temperature for naturally and fan aspirated sensors for different years

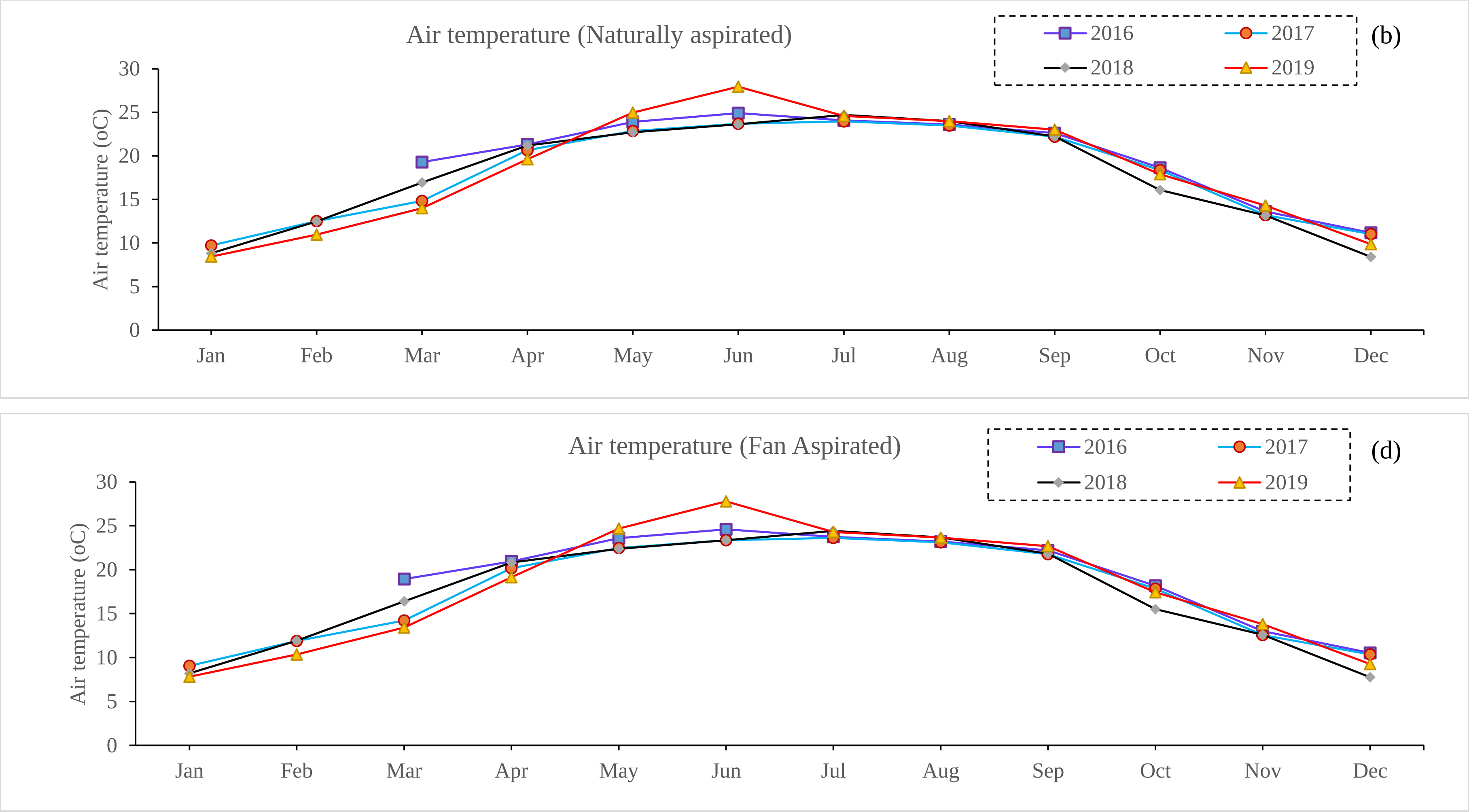

Fig. 4. 5 Variations of the mean monthly air temperature for naturally and fan aspirated sensors for different years

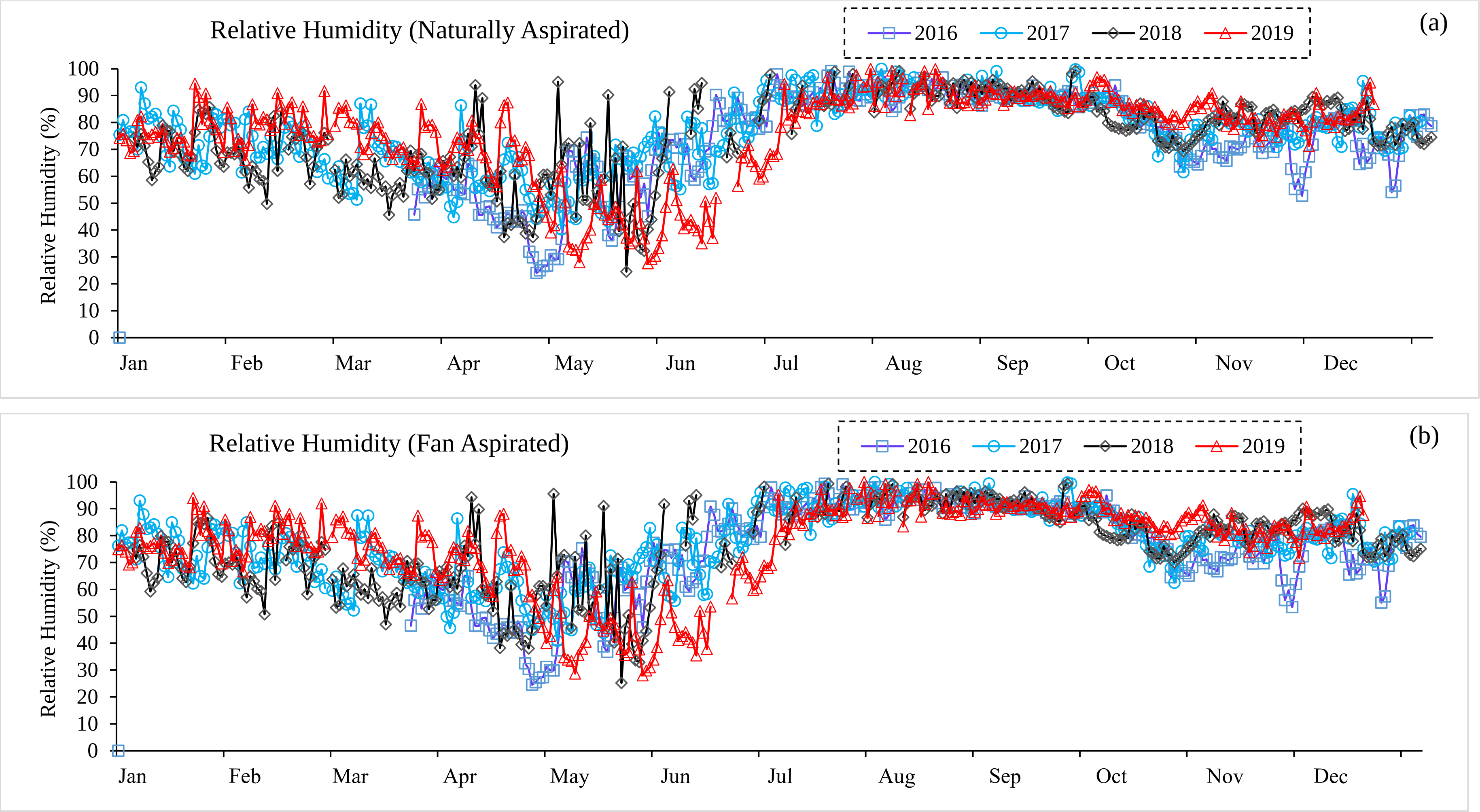

Fig. 4. 6 Variations of the daily mean relative humidity for naturally and fan aspirated sensors for different years

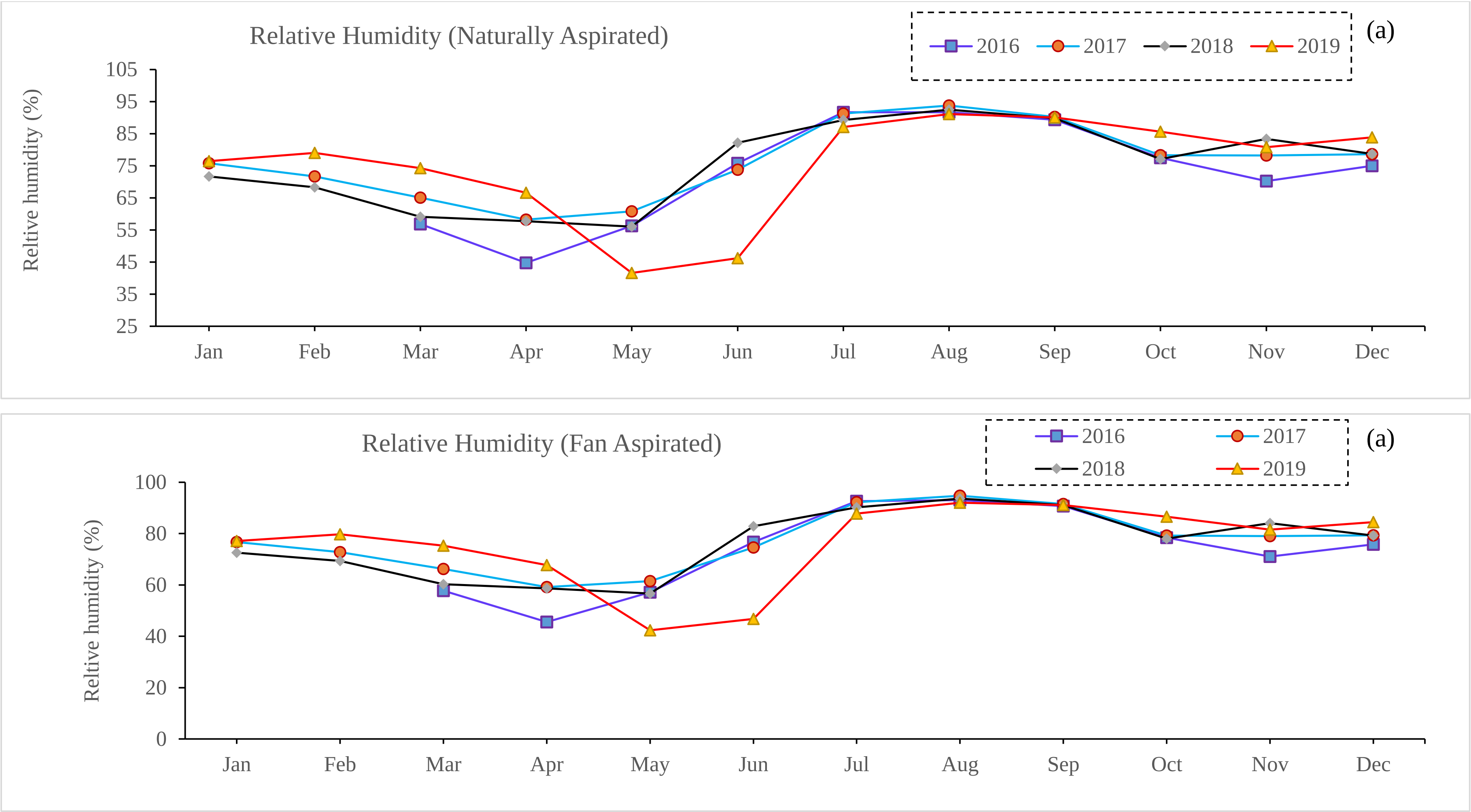

Fig. 4. 7 Variations of the mean monthly relative humidity for naturally and fan aspirated sensors

4.4.3 Wind Speed

Henaval valley is located in Lesser Himalayas with an altitude of 1000m at the valley bottom and surrounded by high hills and a there is the south-northern opening of the valley. The geographical conditions of the valley create unique and well-defined wind profiles. There is adiabatic wind flow in the day time, and catabatic wind occurs in the night. A vertical wind profiling is being attempted at Henval valley by putting wind sensors at different heights.

Fig 4.8 shows the variation of mean daily wind speed at different heights (0.5 m, 2 m, 4 m, 6 m and 10 m). The wind speed is observed maximum in the months of May-June whereas it is found minimum in July - September at the height is 50 cm and 2 m. The wind speed data at 4 m, 6 m and 10 m were not recorded regularly due to technical error continuously and hence challenging to analyze. The average wind speed increases with the increase in height. Mean monthly values for different years are plotted and presented in Fig. 4.9. The average wind speed at 0.2m height was found to be 0.95km/hr and 1.83km/hr at the height of 2m at the Henval valley. The data analysis indicates that the values of the wind speed become more significant as the height of measurement goes up.

4.4.4 Rainfall

Rainfall is an essential component of the hydrological cycle and pre-requisite for any kind of hydrological studies. A tipping bucket type of rain gauge has been installed at the Henval valley to capture the rainfall records. Fig. 4.10 (b) shows the observed pattern of daily rainfall which indicates the highest rainfall (higher peaks) during the monsoon season.

The monthly rainfall is also plotted for all recorded four years in Fig. 4.10 (a). Almost no rain is observed in October and November in all the years. Frequent rainfall is observed with lesser magnitudes from January to May in 2016 and 2017. The year 2017 was found to be a wet year with a total annual rainfall of 1414mm whereas, the year 2018 received only 720mm of annual rainfall. Based on the four years records, the average annual rainfall was estimated as 985mm. The share of the monsoonal rainfall was found to b 79% of the total annual rainfall in the catchment.

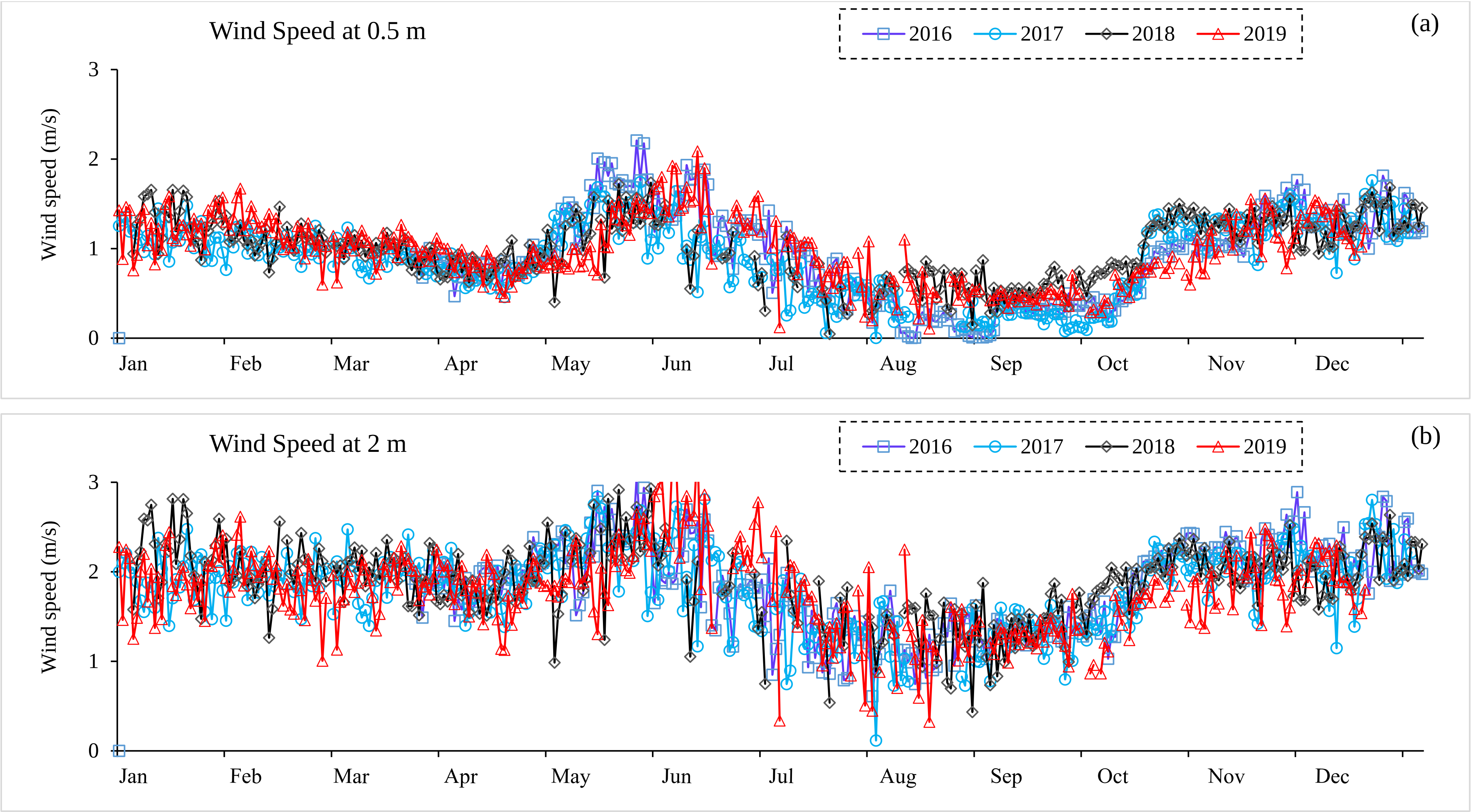

Fig. 4. 8 Variations of the mean daily wind speed at 0.5m and 2m height

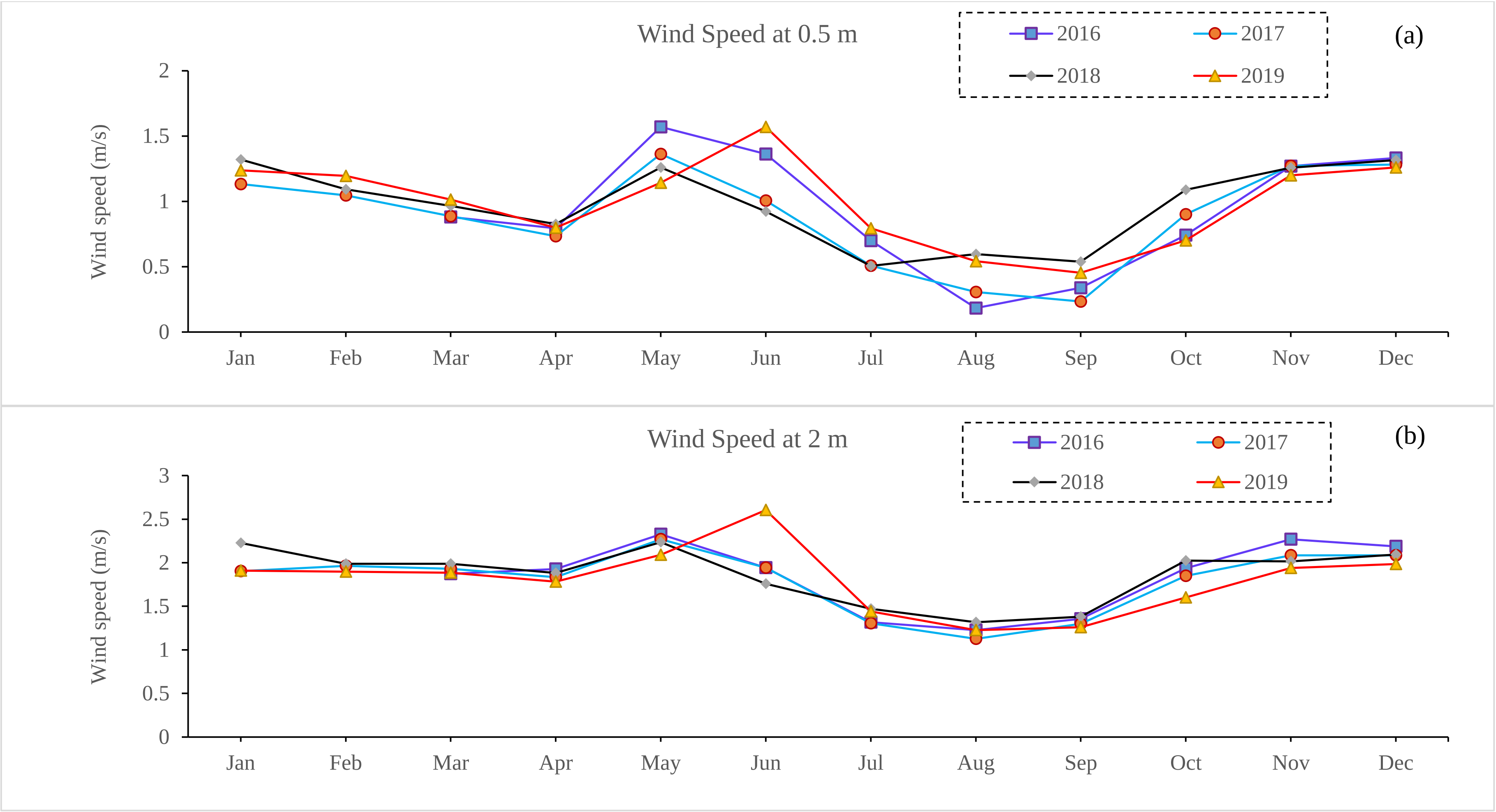

Fig. 4. 9 Variation of the mean monthly wind speed at 0.5m and 2m height

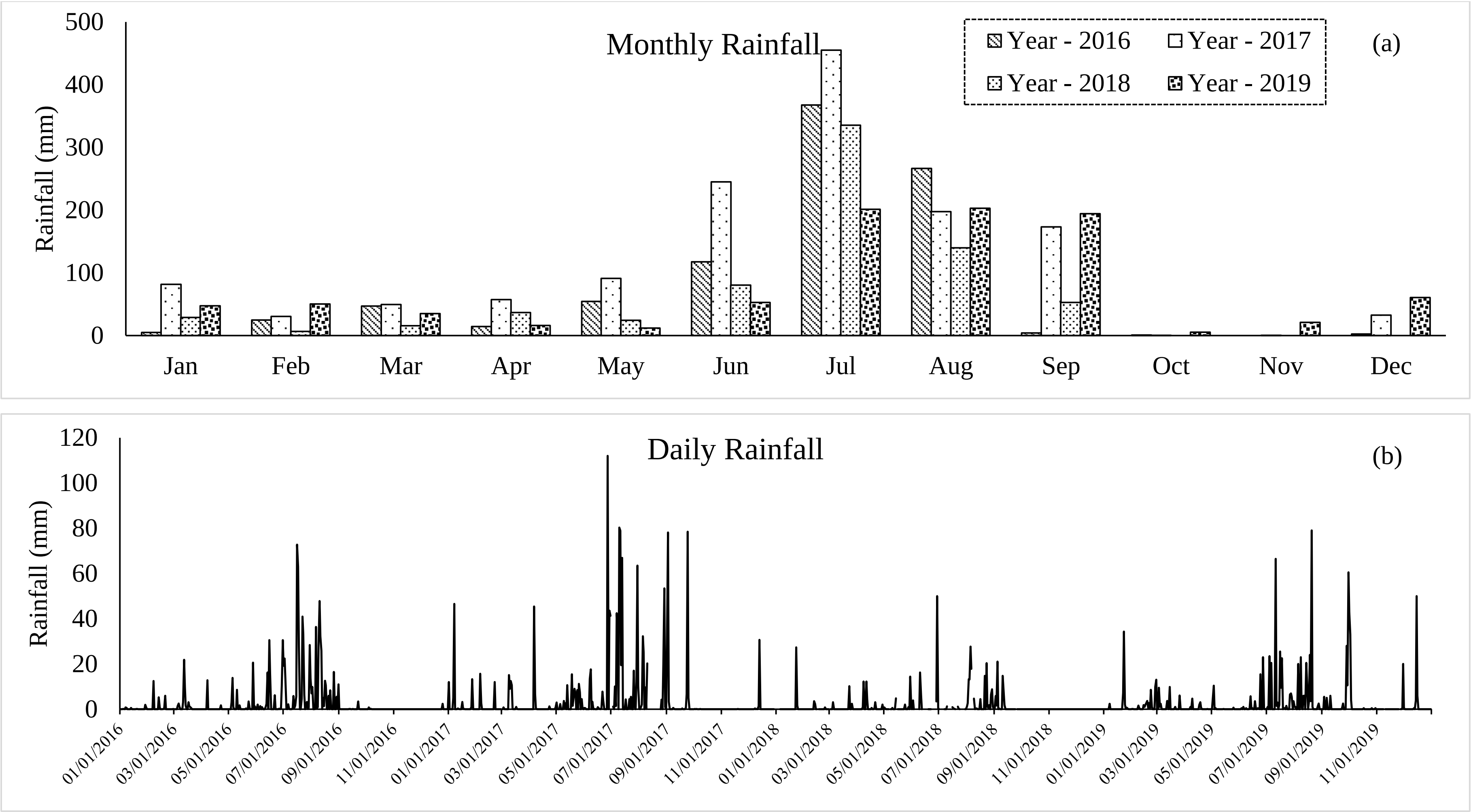

Fig. 4. 10 (a) Variations of the monthly rainfall in different years and (b) Daily rainfall time series at Henval valley.

4.4.5 Soil Moisture and Soil temperature

Soil plays an essential role in the water balance of a catchment. The physical properties of soil mainly soil moisture and soil temperature are critical for seed germination, plant growth and productivity of the land. The soil temperature affects plant growth indirectly by affecting water and nutrient uptake as well as root growth. At a constant moisture content, a decrease in temperature results in a decrease in water and nutrient uptake. At low temperatures, transport from the root to the shoot and vice versa is reduced. Apart from this, the change in the soil moisture in terms of storage is essential for the water balance equation. At Heval valley TDR probes are being used for monitoring the soil moisture and soil temperature, which also provides information about the soil electrical conductivities.

The mean daily soil moisture is recorded at different depths 6 cm, 15 cm, and 50 cm below the ground surface, as shown in Fig 4.11. The mean monthly soil moisture values are also plotted and presented in Fig. 4.12. The results indicate that the soil moisture near the ground surface (6 cm, 15 cm and 50 cm) is highest in the months of July-September and lowest in the months of May and June. This variation of soil moisture is attributed to the occurrence of rainfall in the rainy season. The increase in soil moisture near the ground surface in non-rainy months is due to irrigation. The fluctuations in soil moisture decrease with the increase in depth due to the lesser effect of meteorological phenomena. Similar to soil moisture, electrical conductivity is also recorded at different depths (6 cm, 15 cm and 50 cm) below the ground surface.

Daily soil temperature is recorded at different depths (6 cm, 15 cm, and 50 cm) below the ground surface. Fig. 4.13, and Fig. 4.14 shows the variation of the daily and monthly soil temperature, respectively. From the figures, it can be observed that the soil temperature starts increasing in the month of April and reaches the maximum in the month of June- July, and starts decreasing from October onwards in all the years which is closely linked to the occurrence of rainfall events, increase in solar radiation and clear sky in summer and monsoon months. Soil permittivity increases with increasing water content in the soil.

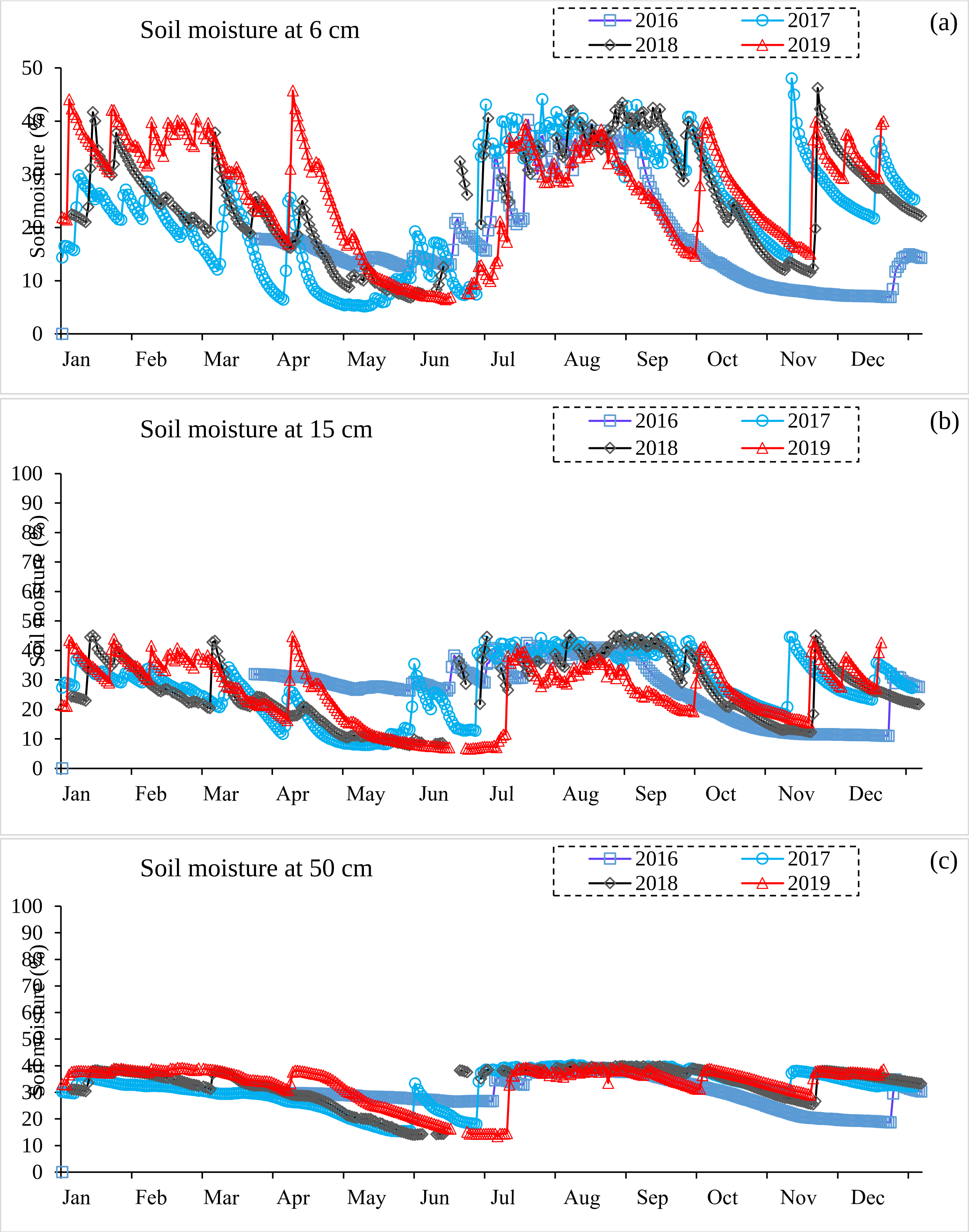

Fig. 4. 11 Variation of the daily soil moisture at different depths

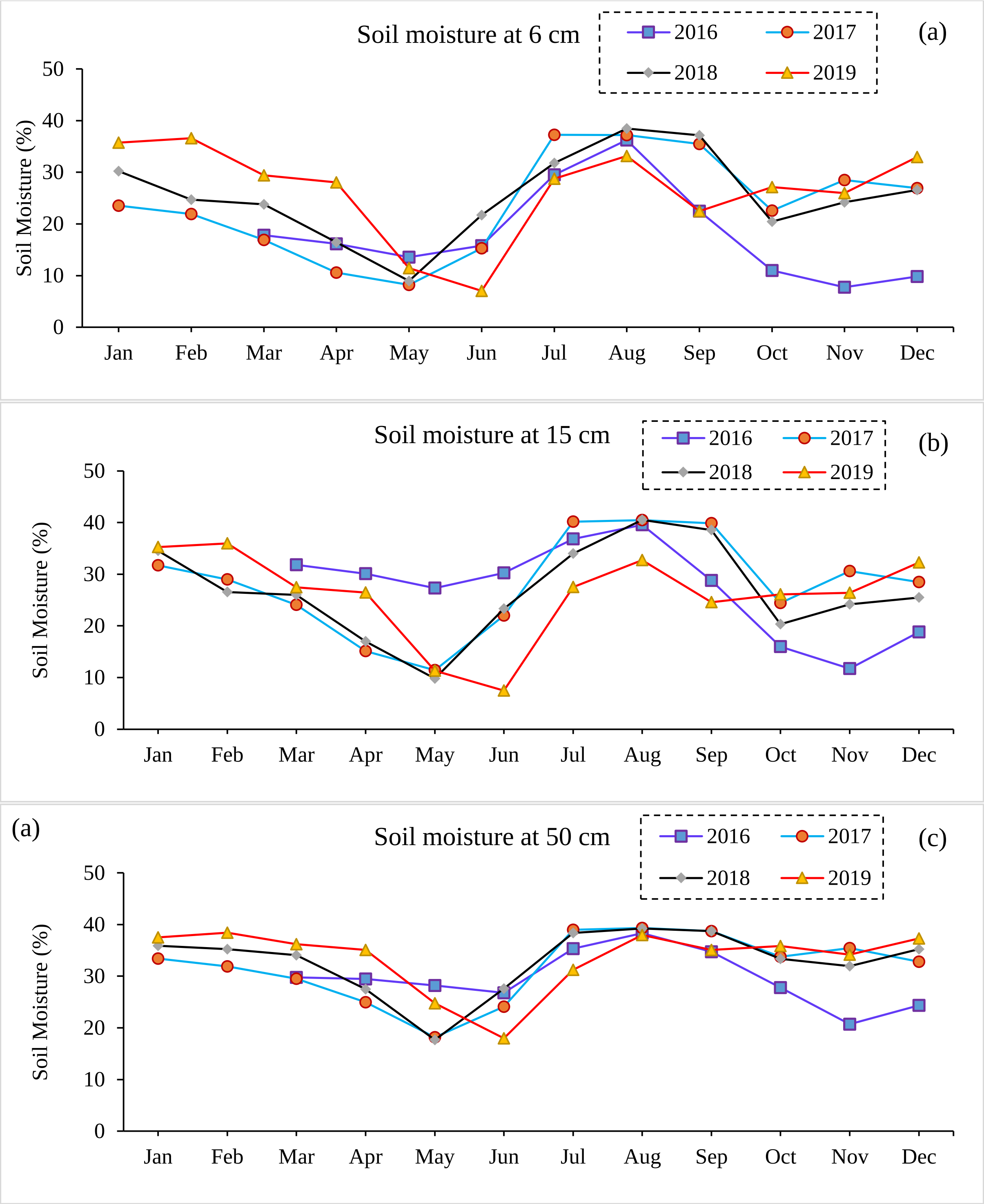

Fig. 4. 12 Variation of the mean monthly soil moisture at different depths

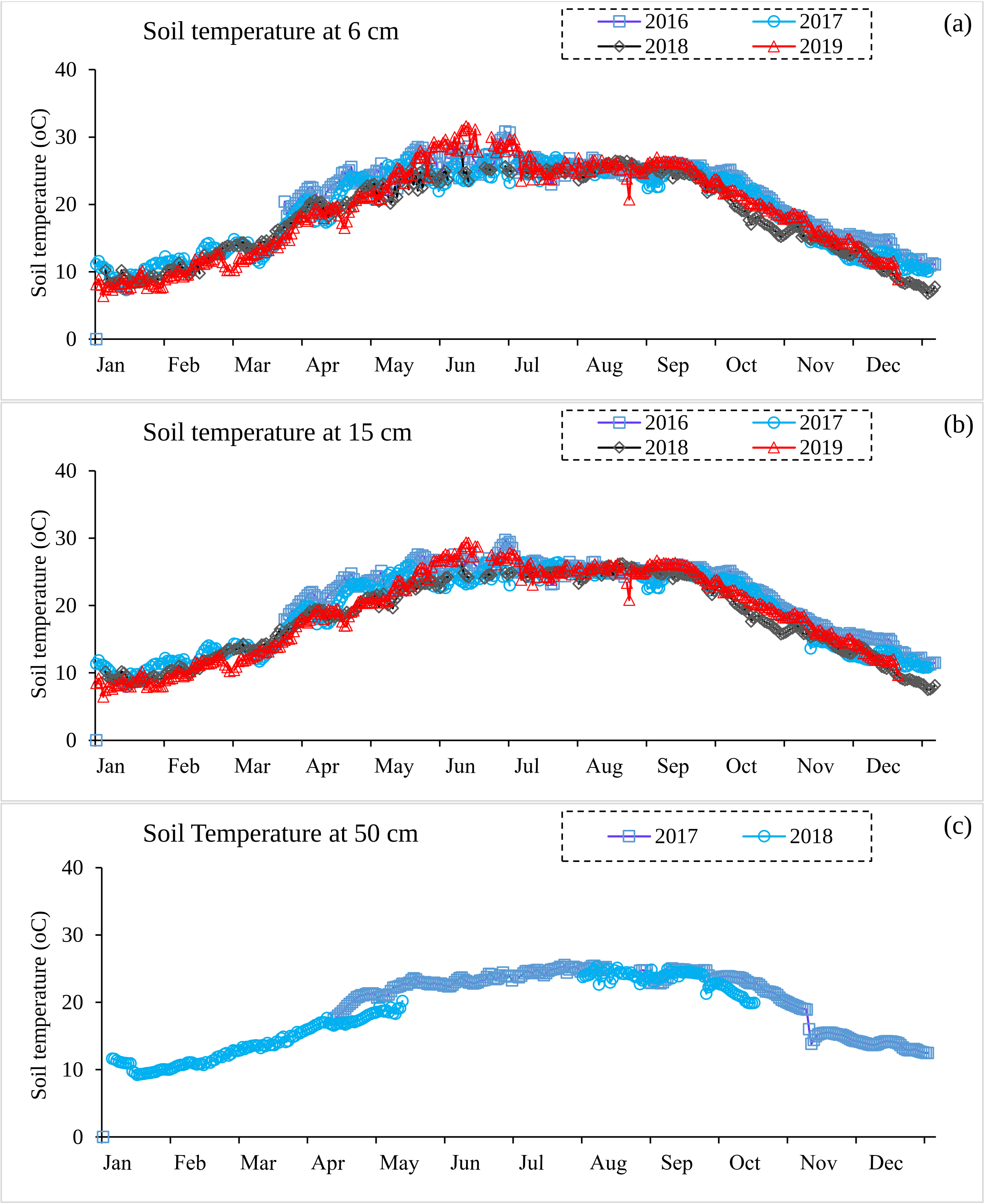

Fig. 4. 13 Variations of the daily soil temperature at different depths

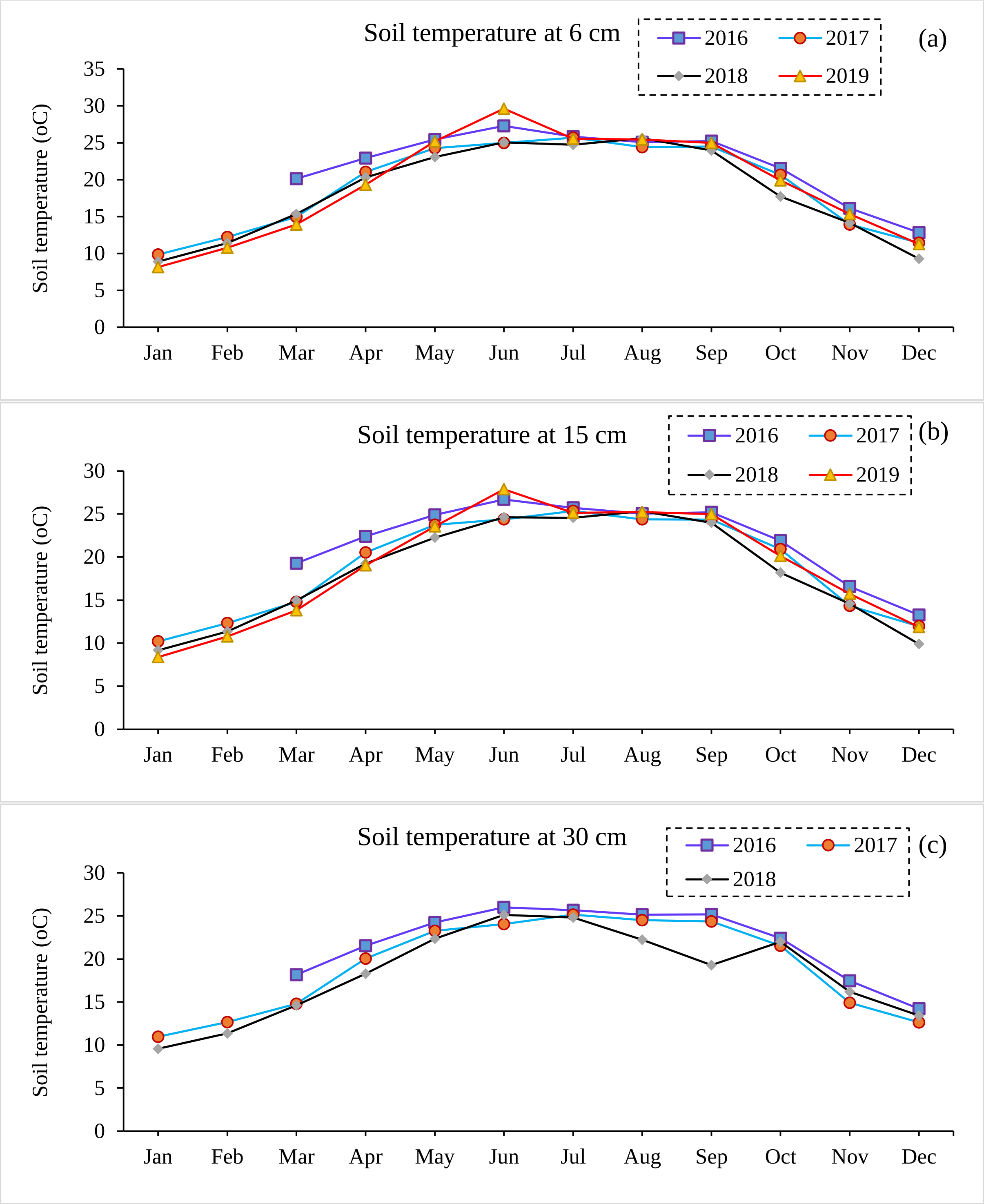

Fig. 4. 14 Variations of the mean monthly soil temperature at different depths

4.4.6 Other Data

Apart from the aforesaid described variable, some other data like atmospheric pressure and solar radiations are also being monitored at Henval valley. Fig. 4.15 shows the variation of atmospheric pressure throughout the year. Here, it follows a smooth trend for all the years, and the seasonal variation is almost negligible. The atmospheric pressure is comparatively high for the year 2016 and 2017, whereas, for the year 2018 and 2019, it is observed low.

Fig. 4.16 shows the variation of net radiation which indicates that the highest net radiation is available in the months of April-September. The increased net radiation in this period is attributed to the increased incoming solar radiation in the summer season as well as the clear sky in the rainy season. The fluctuations are also very high during this period for all the years, which may be due to cloud cover.

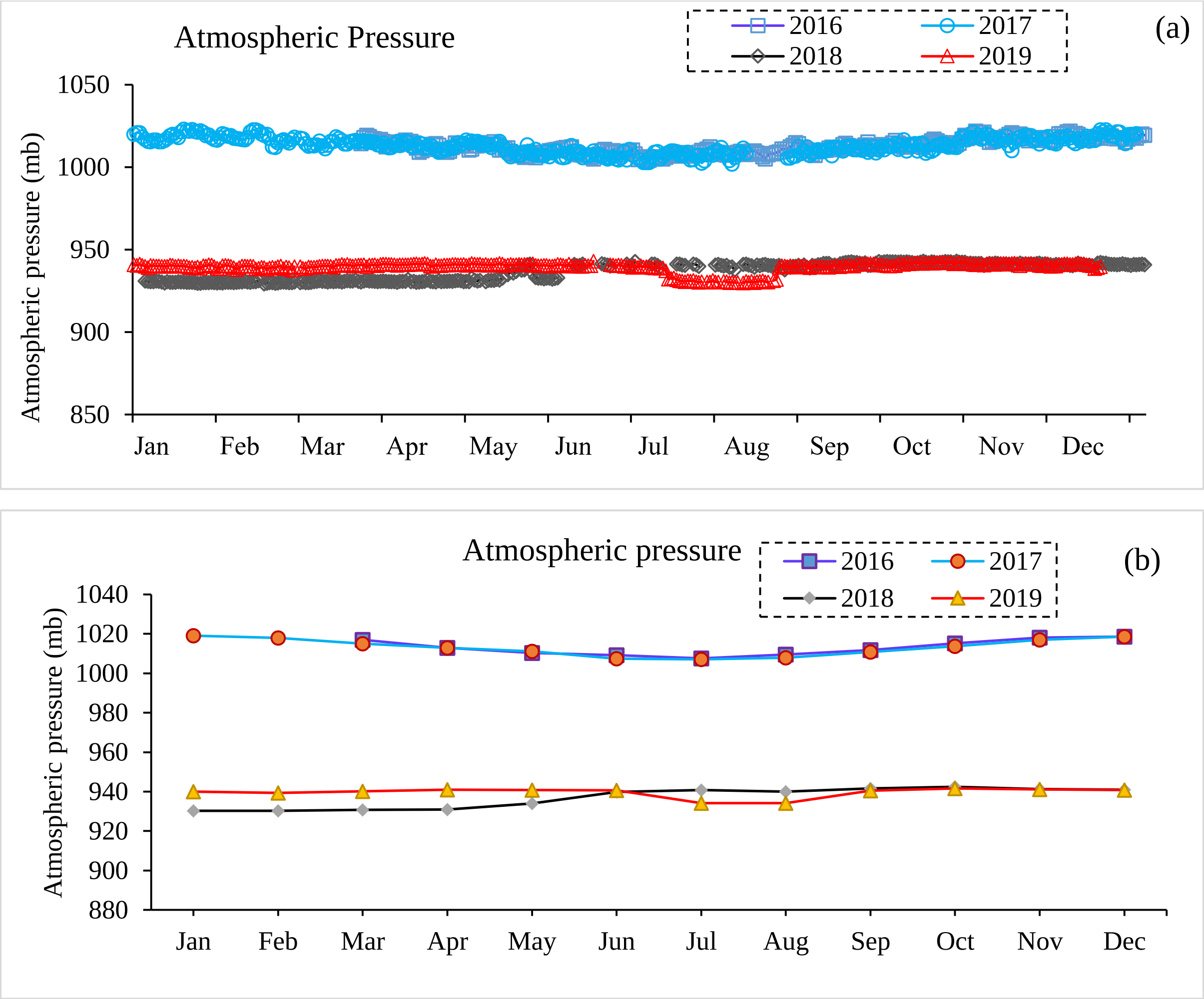

Fig. 4. 15 Variations of the atmospheric pressure

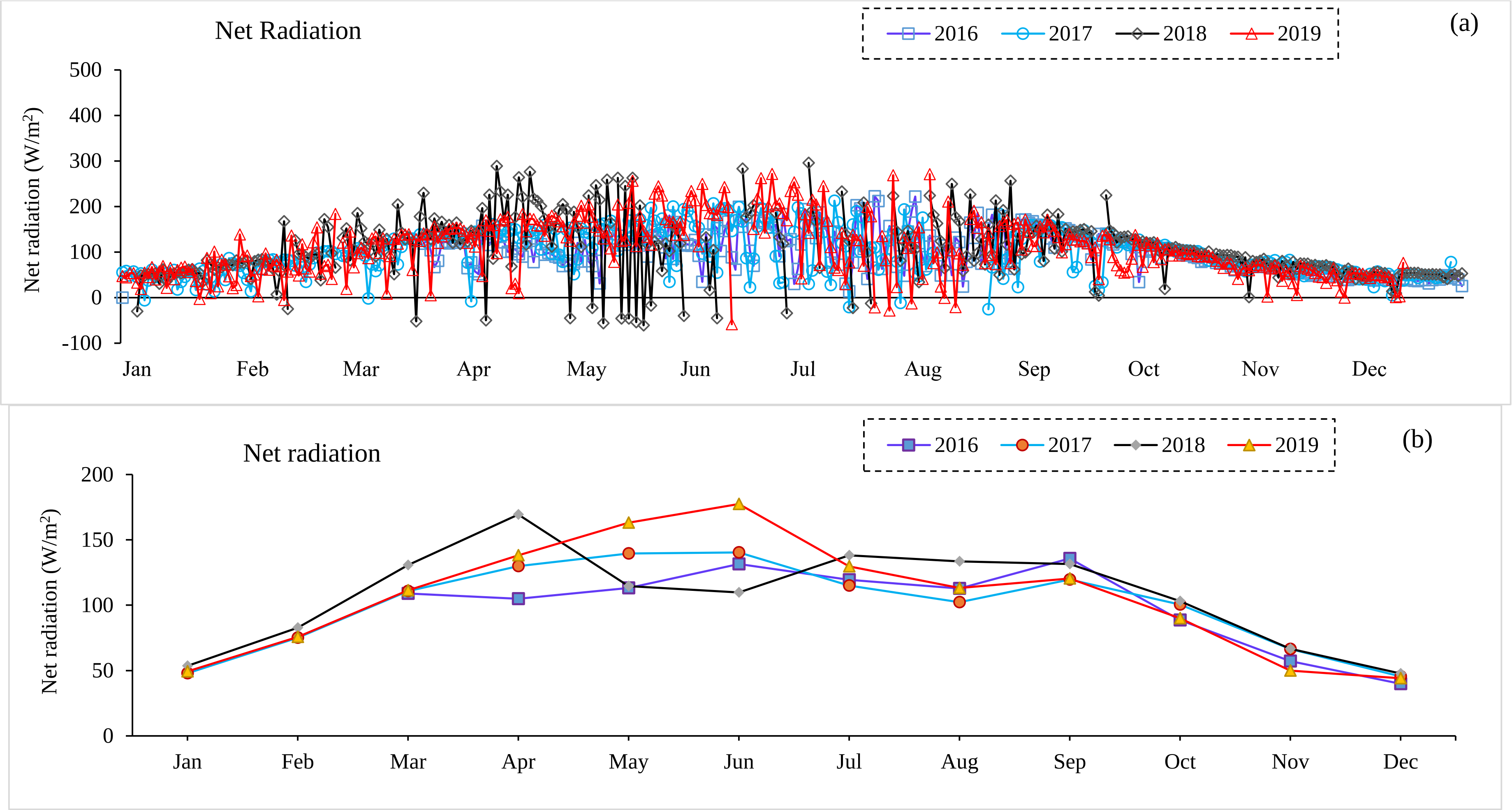

Fig. 4. 16 (a) Daily variations of the net radiation and (b) mean monthly variation of net radiation

4.5 DIURNAL AND DAILY VARIATION IN ATRH MEASURED BY DIFFERENT SENSORS

The variation (diurnal and daily) in average air temperature, measured at the height of 2m from the surface by two different sensors: Sensor with Radiation Shield and Fan aspirated Shield has been studied to find a discrepancy in measurement if it exists. The temperature recorded by these sensors during 21-22 August 2019 has been plotted to see the diurnal variation in air temperature (Fig. 4.17).

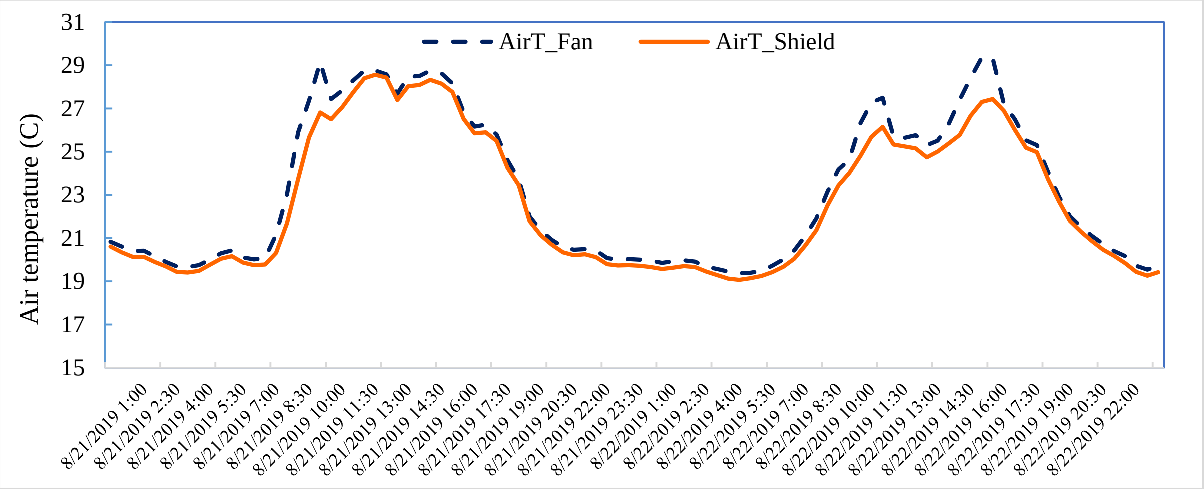

Fig. 4. 17 Diurnal variations in average air temperature measured by radiation shield and fan aspirated shield sensor at Nagani

The temperature measured by the two sensors, in general, follows the same curve and no significant difference in the magnitudes are observed. However, at peak hours, the sensor having fan aspirated shield measures a slightly higher temperature than the sensor having a radiation shield. A more or less similar pattern is also observed in case of daily variation of temperatures, recorded from these sensors (Fig. 4.18). The relative humidity recorded from March 23rd, 2016 to December 31st, 2019 by these sensors is also plotted to examine its daily pattern of variation, as shown in Fig. 4.19. Similar to the temperature, no significant difference in the amount of relative humidity is found.

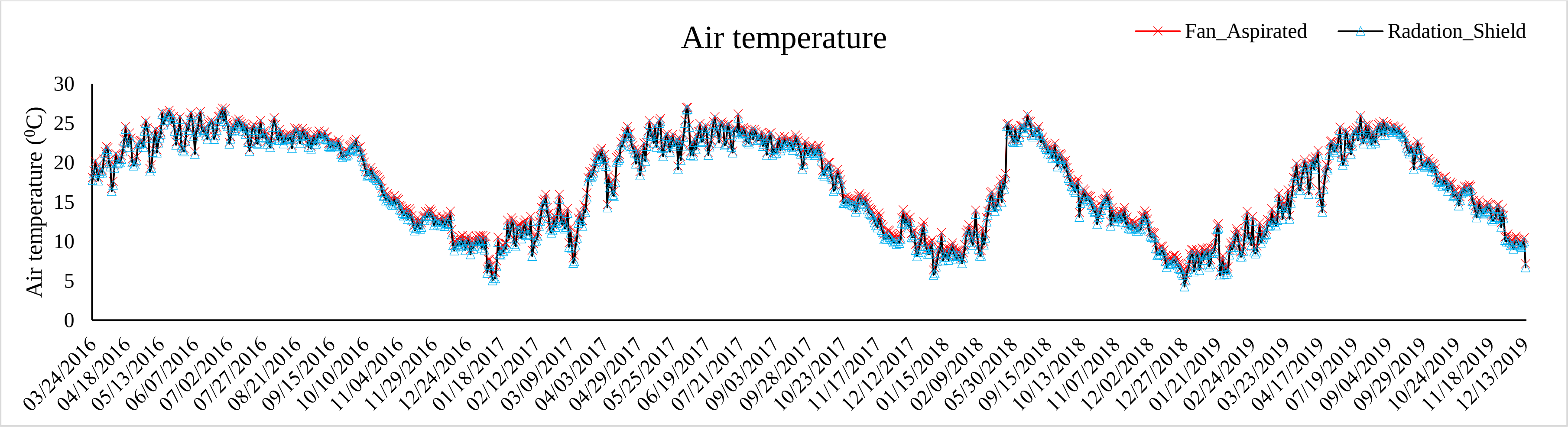

Fig. 4. 18 Daily variations in average air temperature measured by radiation shield and fan aspirated shield sensor at Nagani

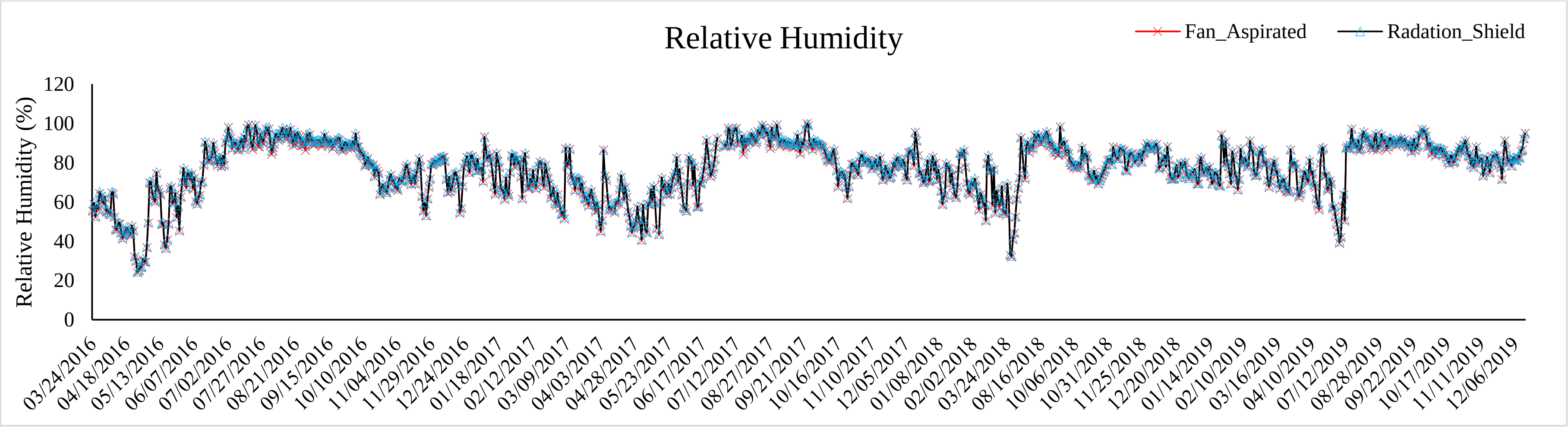

Fig. 4. 19 Daily variations in relative humidity measured by radiation shield and fan aspirated shield sensor at Nagani

4.6 DIURNAL AND DAILY VARIATION IN WIND SPEED MEASURED AT DIFFERENT HEIGHTS

The effect of altitude on the speed of wind has been assessed by the sensors installed at a different height from the surface, respectively. A considerable variation in the pattern of wind speeds (WS_50cm WS_2m, WS_4m, WS_6m and WS_10m) are observed over time due to differences in altitude. This has been shown in Fig. 4.20 (diurnal variation) and Fig. 4.21 (daily variation), respectively. The speed of wind measured near-surface (WS_50cm, WS_2m) is characterised by relatively low speed due to resistance imposed by the surface with respect to wind speed sensed at higher heights.

4.7 DAILY VARIATION IN DIFFERENT COMPONENTS OF SOLAR RADIATION

The daily variation in different components of solar radiation such as Incoming Shortwave Radiation (SW_IN), Outgoing Short Wave Radiation (SW_OUT), Long Wave UP (LW_UP) and Long Wave down (LW_DN) has been examined to study nature of heat flux transfer mechanism between surface and atmosphere (Fig. 4.22). The highest flux has been recorded for SW_IN whose values ranges between 0 to 1132 W/m^2 whereas the values for SW_OUT has been found in the range of 0 to 202 W/m^2 over the surface of the earth. The values of LW_IN and LW_OUT are found in the middle of 310 to 621.3 W/m^2, and 244.7 to 448.2 W/m^{2,} respectively.

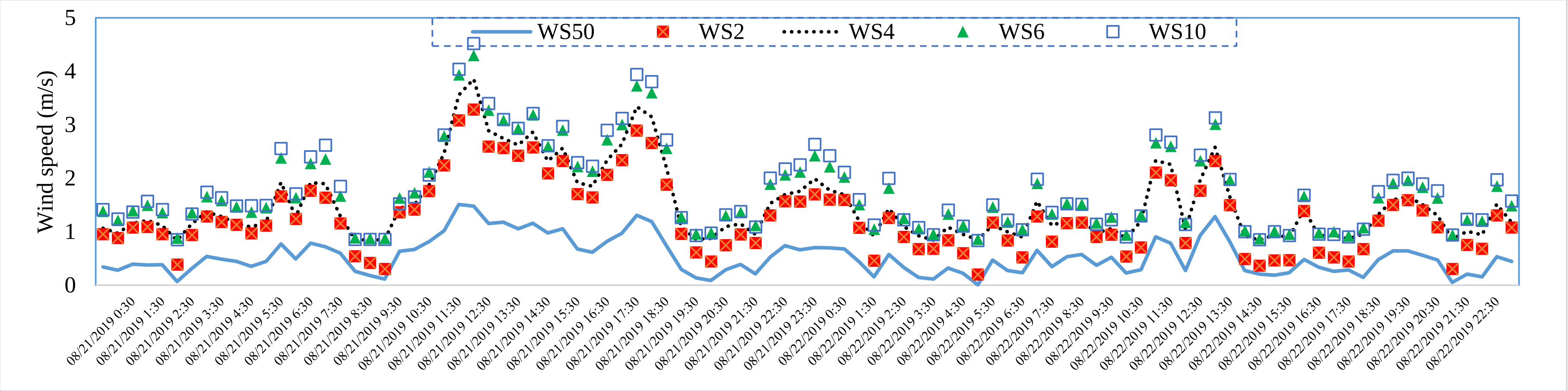

Fig. 4. 20 Diurnal variations in average wind speed measured at different heights at Nagani

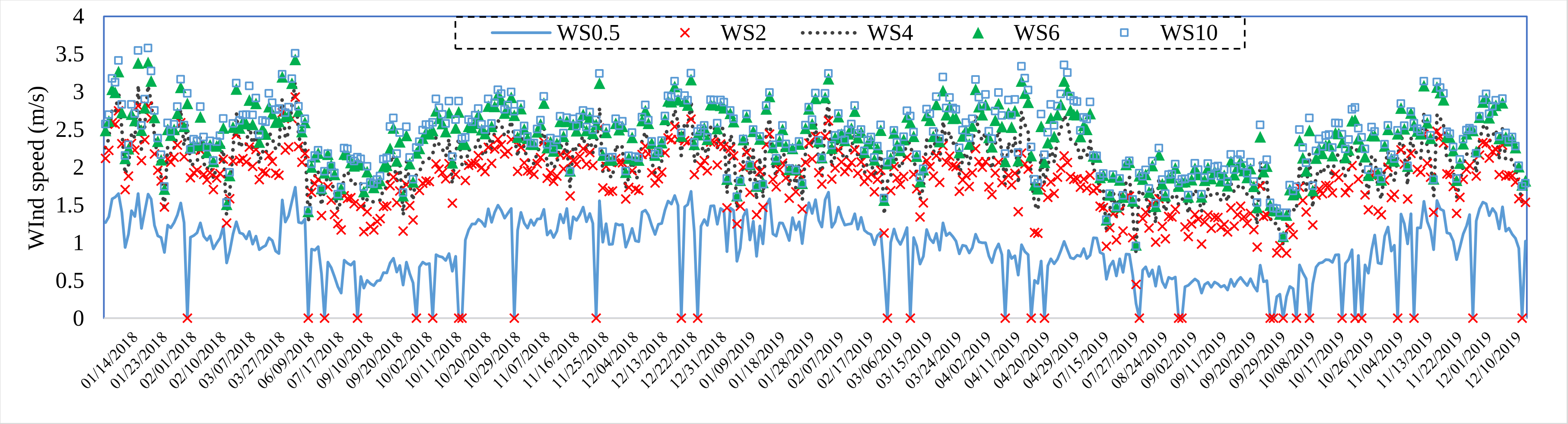

Fig. 4. 21 Daily variations in average wind speed measured at different heights at Nagani

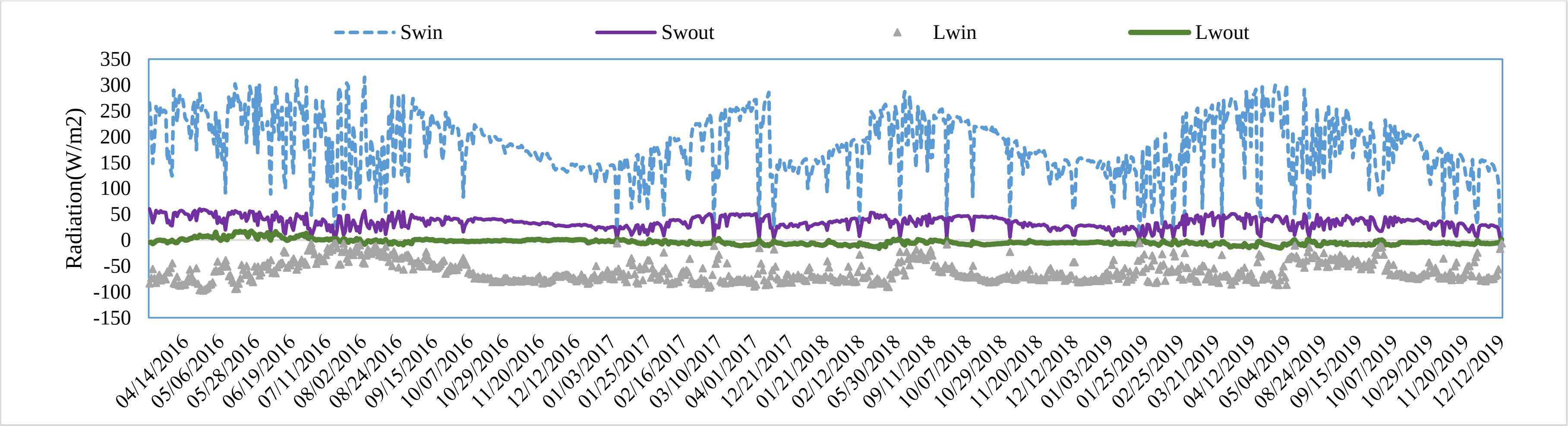

Fig. 4. 22 Daily variations in different components of solar radiation at Nagani

4.8 ESTIMATION OF SOIL HEAT FLUX

The amount of thermal energy that moves through the soil in an area a unit of time is the soil heat flux or heat flux density (G). Soil heat flux is vital in micrometeorology because it effectively couples energy transfer processes at the surface (surface energy balance) with energy transfer processes in the soil (soil thermal regime). G is positive when the soil is warming and contrary, when the soil is cooling. The surface Heat Flux of Soil (G) is determined from measurements of heat flux at plates (Gz_p) which are placed at a depth of z_p and the heat stored (S_{Soil}) by the soil between the surface and z_p as described by Onsley et al, 2007:

$$G = S_{Soil} + Gz_p \qquad \dots (4.1)$$

The value of Gz_p is obtained directly by the sensor, whereas, the value of S_{Soil} is obtained from the following equation:

$$S_{Soil} = -c_{Soil} z_p \times \frac{dT_{soil}}{dt} \qquad \dots (4.2)$$

Where,

$$C_{Soil} = \rho_{water} \times Q_{soil} \times c_{water+} \, \rho_{soil.dry} \times c_{soil.dry} \qquad \dots (4.3)$$

where, T_{soil} is the soil temperature, C_{Soil} is heat capacity of soil, ρ_{water} is density of water, Q_{soil} is volumetric soil moisture fraction, c_{water} is heat capacity of water, and $\rho_{soil.dry}$ and $C_{soil.dry}$ are density and heat capacity of dry soil, respectively.

After estimating the values of surface soil heat flux (G) from the equations as discussed above, its relation with net radiation (R_n), air temperature measured at 2m height (AirT) from the surface, and volumetric water content (VWC) measured at a depth of 6cm, on diurnal and daily time steps has been studied. Diurnal variation of G for August 21st and 22nd, 2019 at Nagani station follows more or less the similar patterns as shown by R_n and AirT. G shows a gradual increase in its values over time and attains its peak values (35 W/m^2) at around noon, and then starts declining and reaches its lowest values after an evening at Nagani.

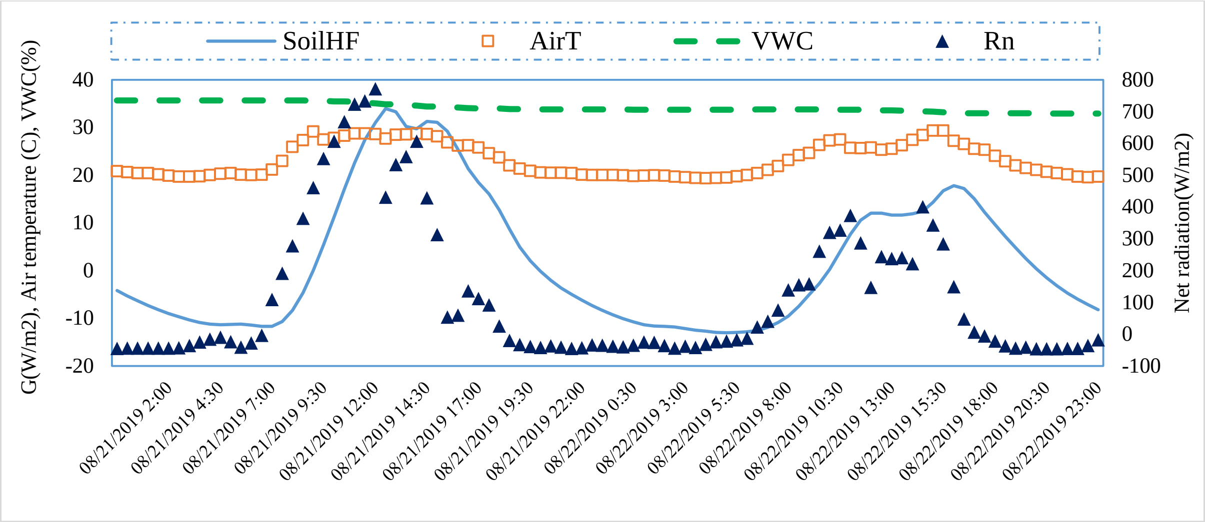

Fig. 4. 23 Diurnal variations in the soil heat flux, Air_Temp, VWC and Net radiation

A relatively straight line observed in VWC shows that there is no significant change in soil moisture content during a day for this short period. However, this is not the case as VWC varies significantly over time and the straight line observed here is due to the scale on which it has been represented along with other parameters. Fig. 4.23 shows the variation on net radiation, air temperature and VWC over a period of 48 hours, i.e. two days (August 21st and 22nd, 2019). Similarly, the daily patterns of these parameters have also been plotted and analysed, which is shown in Fig. 4.24. In general, peaks of G and AirT which follow the peaks of R_n, are lagged by an average of 2 hours and 20 minutes, and 44 minutes respectively. The soil moisture content (VWC), however, gradually declines over time. The peaks observed in VWC during intermediate days are generally associated with rainfall events that have occurred on these days.

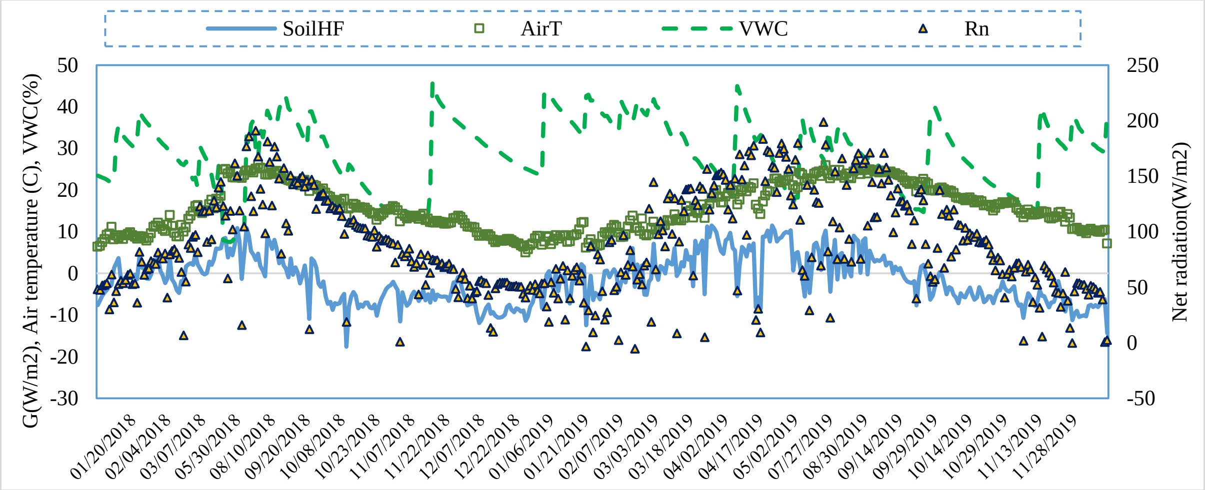

Fig. 4. 24 Daily variations in the soil heat flux, Air_Temp, VWC and Net radiation

The nature of diurnal and daily variations in soil heat flux (G) has also been investigated with respect to soil temperatures measured at different depths such as T_6cm, T_15cm, T_50cm and T_90cm at Nagani and T_2cm, T_6cm, T_25cm, T_50cm and T_100cm at Kanataal. The diurnal pattern of G concerning different soil temperatures has been plotted for August 21st and 22nd, 2019 and shown in Fig. 4.25 Surface Soil Heat Flux follows a pattern of a sinusoidal cycle where sharp increase and fall in its values are observed over time compared to the soil temperature. Among the soil temperatures, T_2cm, T_6cm is characterised by the relatively sharp peak, and more substantial variability whereas T_90cm and T_100cm has not shown any significant variation over time. It is represented by a straight line which shows that soil temperature does not vary as depth increases. Fig. 4.26 shows the daily pattern of variation in G with respect to T_6cm, T_15cm, T_50cm and T_90cm.

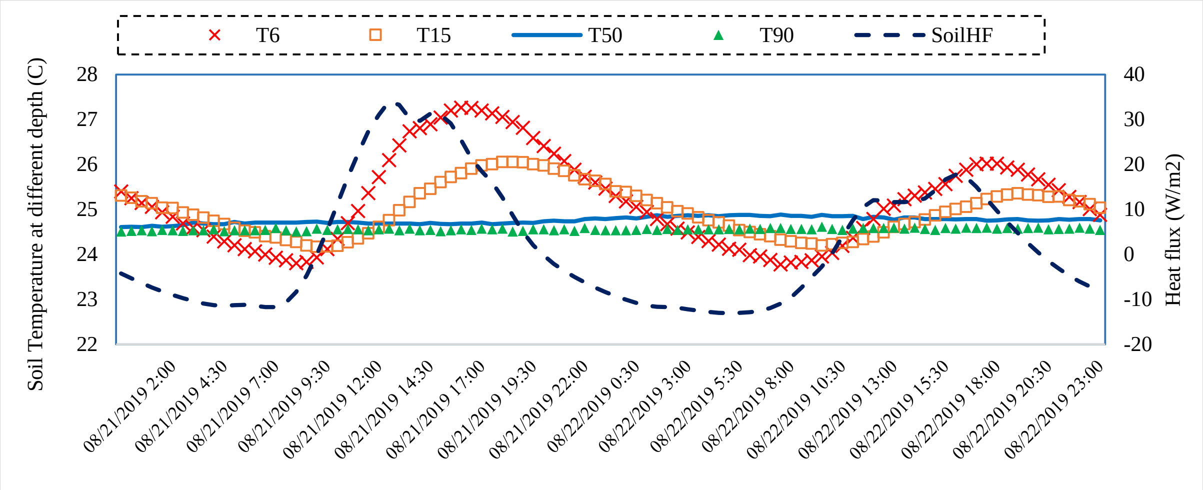

Fig. 4. 25 Diurnal variations in the soil heat flux to soil temperatures at different depths

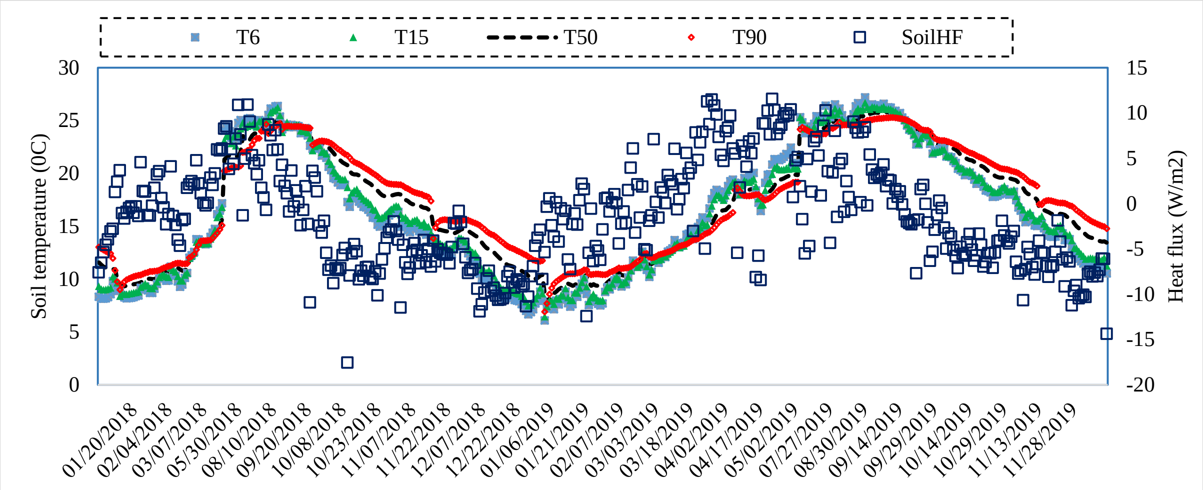

Fig. 4. 26 Daily variations in the soil heat flux to soil temperatures at different depths

The soil heat flux recorded at 8 cm below the ground surface is shown in Fig. 4.27 (a-b) which indicates its variation is higher during April to September months in all the years, which may be attributed to the various reasons such as cloud cover, vegetation cover, etc.

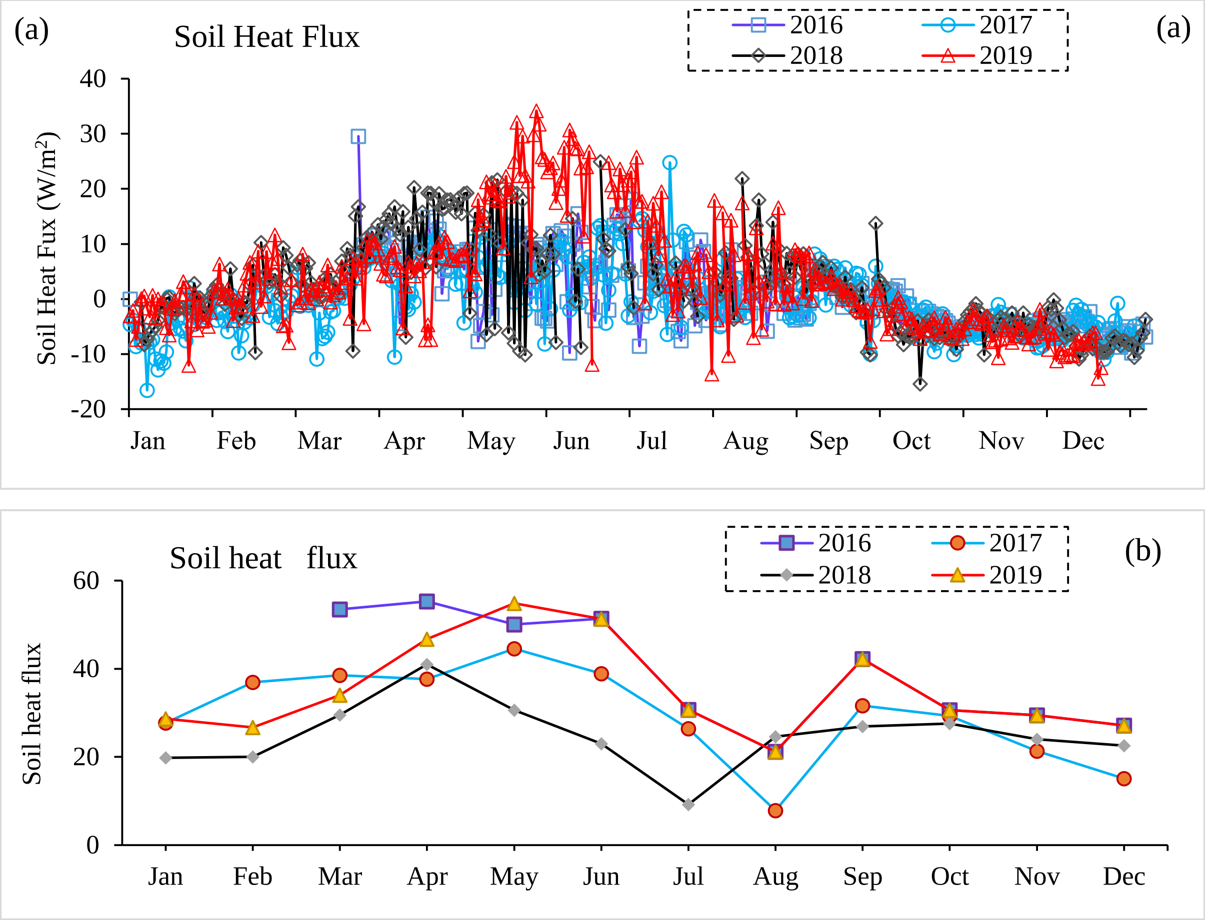

Fig. 4. 27 Variations of the soil heat flux (a) daily and (b) mean monthly at Nagani AWS Site

CHAPTER 05: EVAPOTRANSPIRATION ESTIMATION

5.1 GENERAL

Evapotranspiration (ET) is one of the major components to identify the behaviour of the hydrologic cycle. Correct estimation of reference evapotranspiration (ET_0) is necessary for determining irrigation demands, irrigation scheduling, water resources management, and environmental impact assessment, water balance studies at regional and local levels, and modelling of various rainfall-runoff and ecosystem models. Further, the actual ET can be determined using crop coefficients, which is mainly a function of various crop characteristics and local environmental conditions. This paper deals only with the estimation of ET_0. Inaccurate estimates of ET_0 can lead to unproductive use of water, false calibrations of hydrological models, and erratic assessments of groundwater recharge. There are many empirical equations available for estimating ET_0, but their cogency is sometimes restricted to particular geographic locations or /and specific climatic conditions. Allen et al. (1998) defined ET_0 as “the rate of evapotranspiration from a hypothetical crop with an assumed crop height (0.12 m) and a fixed canopy resistance (70 s/m) and albedo (0.23) which would closely resemble evapotranspiration from an extensive surface of green grass cover of uniform height, actively growing, completely shading the ground and not short of water. The Food and Agriculture Organization (FAO) of the United Nations recently adopted a standardized form of the Penman-Monteith equation (FAO56 PM) in an effort to provide a common, globally valid standard for estimating ET_0, developing crop coefficients, and evaluation/calibration of other ET_0 methods when Lysimeter measurements are unavailable (Allen et al. 1998). There are more than twenty established methods available for estimating of ET_0. These can be broadly classified into three groups temperature-based approaches (i.e. Hargreaves-Samani and Thornthwaite), radiation-based approaches (i.e. Priestley-Taylor and Turc) and combination approach (i.e. Penman-Monteith). Most of these methods and physically based and need a variety of input data.

ET mapping has many applications, including crop water management, climate change impact assessment, hydrological modelling, groundwater recharge studies, irrigation performance, and land use planning. At field scales, ET can be measured over a homogenous surface using conventional techniques such as the Bowen ratio (BR), eddy covariance (EC), water balance, and lysimetric systems; however, these systems do not provide spatial trends at the regional scale, especially in heterogeneous landscapes. Generally, large weighing lysimeters are considered the most accurate instrument for direct ET measurement in the field, while the tower-based measurements of EC and BR, and water balance methods are commonly employed; each differs in their achievable accuracy range and operational capabilities. With the advent of earth-observing satellites, numerous remote sensing-based ET (RS-ET) algorithms were developed and validated. SEBAL is considered as one of the typical RS-ET algorithms that have continuously evolved and received broader acceptance around the world. According to the developers, by 2005, SEBAL was applied in more than 30 countries for mapping ET, indicating that SEBAL is one of the widely used RS–ET algorithms.

5.2 EMPIRICAL METHODS

Evapotranspiration is the important factor in water balance as mentioned above and actual evapotranspiration that is directly measured by methods such as lysimeter, eddy covariance, water balance etc. also calculated using reference evapotranspiration and crop coefficient. There are a variety of methods to get reference evapotranspiration based on climatic parameter availability. Some of the widely used methods are discussed below.

The reference evapotranspiration has been estimated using temperature-based methods (Hargreaves-Samani and Blaney-Criddle) and radiation-based methods (Priestley-Taylor and Makkink method). The ETo estimated using methods described above have been compared with the corresponding value of the Food and Agriculture Organization, Irrigation and drainage paper 56 (FAO-56) Penman-Monteith (PM) method. Table 5.1 gives details about the parameters required in the above-discussed methods.

Table 5. 1 Input parameters required for ETo estimation

	Input parameters			
Methods	**Air Temperature**	**Radiation**	**Wind Speed**	**Relative Humidity**
FAO-56 Penman-Monteith	✓	✓	✓	✓
Hargeaves-Samani (1985)	✓	-	-	-
FAO-24 Blaney-Criddle (1986)	✓	-	-	-
Priestley-Taylor (1972)	✓	✓	-	-
Makkink	✓	✓	-	-

5.2.1 Penman-Monteith (FAO-56 Method)

Penman-Monteith (PM) FAO56 method for estimating ET is a physically-based method that unambiguously integrates both physiological and aerodynamic parameters (Xu et al., 2006). It is supposed to be the most consistent and worldwide accepted method for ET estimation under various types of climate. The most common form of the PM method in computing ET is given as (Allen et al., 1998):

$$ET = \frac{0.408\Delta(R_n - G) + \gamma\frac{900}{T+273}u_2(e_s - e_a)}{\Delta + \gamma(1 + 0.34u_2)} \qquad \ldots (5.1)$$

Where γ is psychrometric constant (kPa/oC), Δ is slope vapour pressure curve (kPa/oC), and es and ea are saturation and actual vapour pressure (kPa) respectively. The FAO Penman-Monteith equation determines the evapotranspiration from the hypothetical grass reference surface and provides a standard to which evapotranspiration in different periods of the year or in other regions can be compared and to which the evapotranspiration from other crops can be related (Allen et al., 1998). In figure 5.1, the pattern of daily ET can be seen that shows ET value starts from minimum (~3mm/day) in January month and goes highest (~7mm.day) in mid months (July- August) and it follows the same pattern every year.

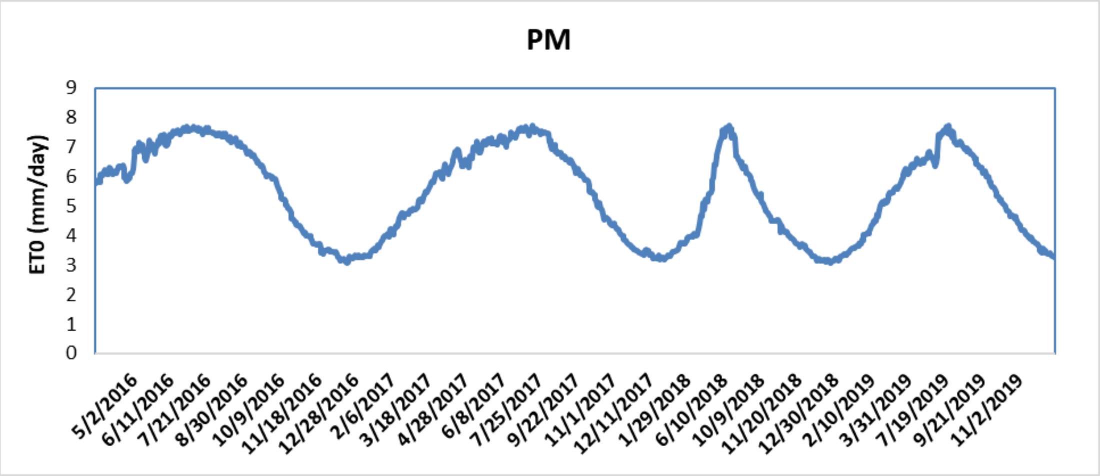

Fig. 5. 1 ET - Penman-Monteith FAO 56 method (MAR 24, 2016-DEC 12, 2019)

5.2.2 Hargreaves Method

Hargreaves and Samani (1982, 1985) proposed many improvements to the Hargreaves (1975) equation for the estimation of grass-related reference ET (mm/d), one of them has the following form as equation 5.2

$$ET = aR_aTD^{0.5}(T_a + 17.8) \qquad \ldots (5.2)$$

where *a* is constant having value 0.00023, *TD* is the difference between the maximum and minimum daily temperature (^{o}C), R_a is the extra-terrestrial radiation. In Fig. 5.2, the ET values are in good correlation with maximum temperature. In this method, ET value starts from minimum (~2mm/day) in January month and goes highest (~7mm.day) in mid months (May-June), and it follows the same pattern every year, but it shows too many fluctuations within a month on a daily basis.

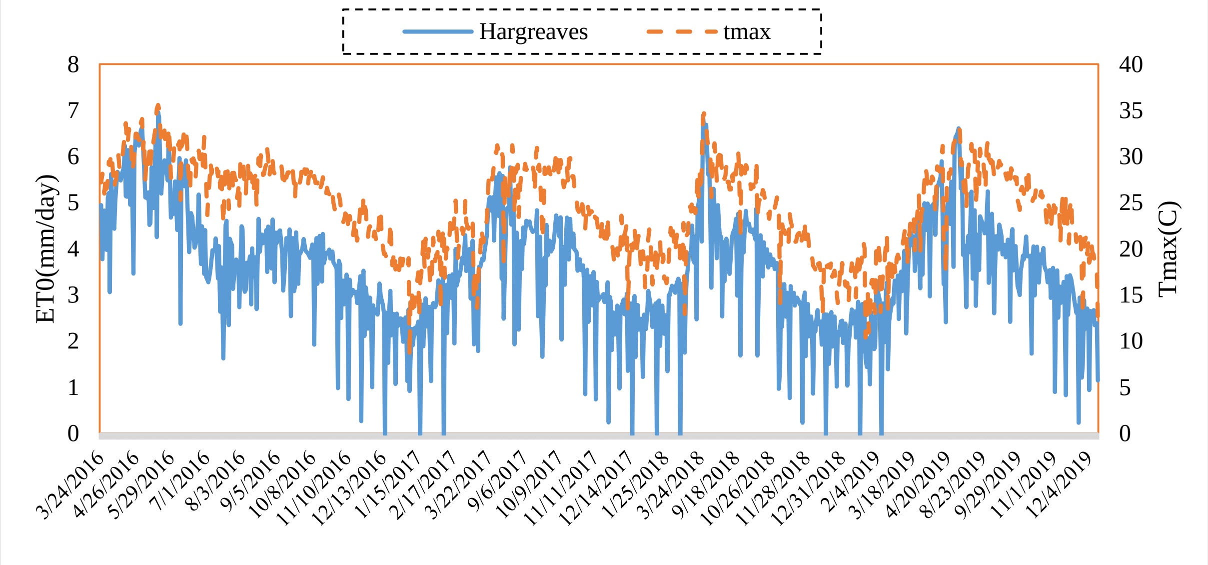

Fig. 5. 2 Variation of ET (Hargreaves method) with maximum temperature (MAR 24, 2016-DEC 12 2019)

5.2.3 Makkink Method

For estimating potential evapotranspiration (mm/day) from grass Makkink (1957) proposed the equation 5.3

$$ET = 0.61\frac{\Delta}{\Delta+\gamma}\frac{R_S}{\lambda} - 0.12 \qquad \ldots (5.3)$$

Where Rs is the total solar radiation (cal/cm2/day), Δ is the slope of saturation vapour pressure curve (mb/oC), γ is psychrometric constant (mb/oC), λ is latent heat (cal/gram), and P is atmospheric pressure (mb). These quantities are calculated using FAO-98 recommended procedure, and units have to be converted to what is required in Makkink equation. In figure 5.3, the pattern of daily ET can be seen that shows ET value starts from minimum (~1.5mm/day) in January month and goes highest (~4mm/day) in mid months (June-July) and it follows the same pattern every year.

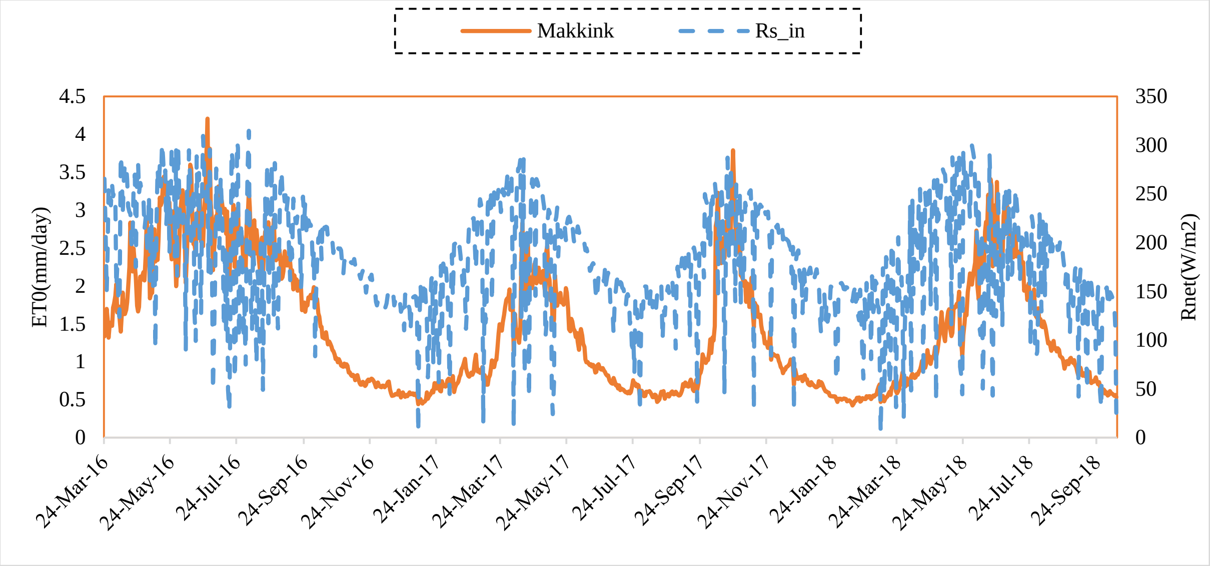

Fig. 5. 3 Variation of ET (Makkink method) with Incoming SW (MAR 24th, 2016 - DEC 12th, 2019)

5.2.4 Priestly-Taylor method

Priestley and Taylor (1972) proposed a simplified version of the equation (Penman, 1948) for use where surface conditions generally were humid, which is a condition required for potential evapotranspiration, ET. The aerodynamic component was removed, and the energy component was modified with a multiplicative coefficient, $\alpha = 1.26$ when the surrounding areas were wet or humid conditions. ET can be expressed as equation 5.4.

$$ET = \alpha \frac{\Delta}{\Delta+\gamma}\frac{R_n - G}{\lambda} \qquad \dots (5.4)$$

In Fig. 5.4, It can be seen that temperature is in good correlation with ET values and there is no proper correlation between ET and relative humidity.

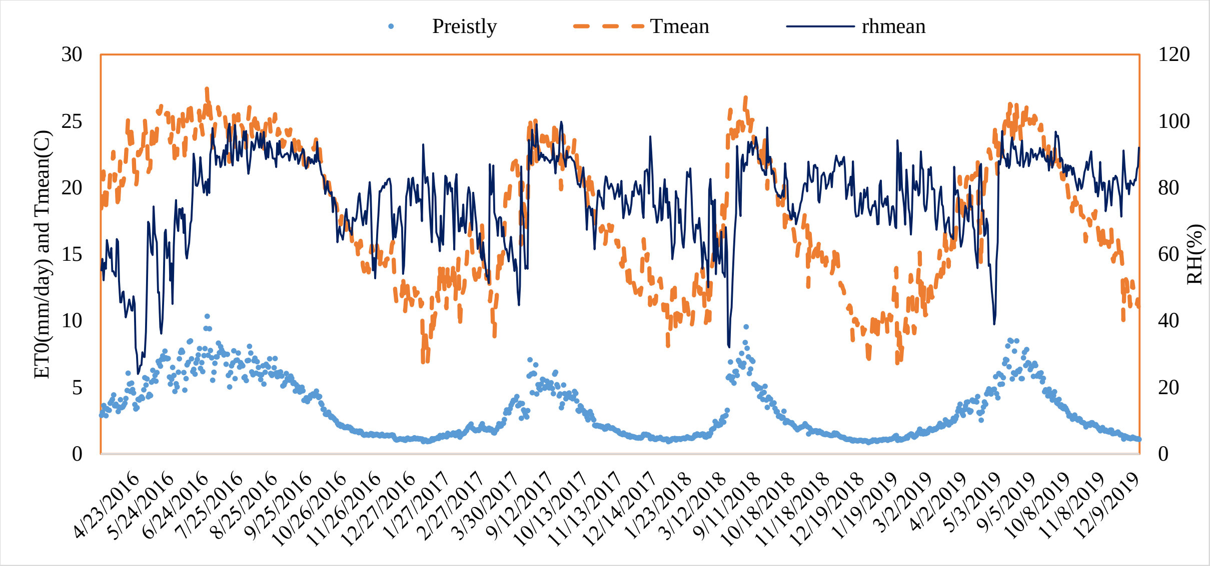

Fig. 5. 4 Variation of ET (Priestly-Taylor method) with mean air temperature and relative humidity (March 24th 2016-Dec. 12th 2019)

5.2.5 Blaney-Criddle (FAO-24 Method)

The Blaney-Criddle (1950) procedure for estimating ET is well known in the western U.S.A. and has been used extensively elsewhere also (Singh, 1989). The usual form of the Blaney-Criddle equation converted to metric units is written as:

$$ET = kp(0.46T_a + 8.13) \qquad \dots (5.5)$$

Where Ta is the mean temperature in °C, p is the percentage of total day time hours for the used period (daily) out of total daytime hours of the year, k monthly consumptive use coefficient, depending on vegetation type, location and season and for the growing season, k varies from 0.5 for the orange tree to 1.2 for dense natural vegetation. In Fig. 5.3, the pattern of daily ET can be seen that shows ET value starts from minimum (~2.5mm/day) in January month and goes highest (~6.5mm/day) in mid months (July-August) and it follows the same pattern every year.

In Fig. 5.6, different scatterplots of Penman-Monteith and other methods are being shown. Fig. 5.6 (d) shows the best correlation with R^2 value 0.93 that is for Blaney-Criddle. Fig.5.6 (a, c) show the second best correlation with R^2 value 0.88 and 0.87 for Priestly-Taylor and Makkink, respectively. Figure 5.6 (b) shows the worst correlation with R^2 value 0.45 among all for Hargreaves-Samani.

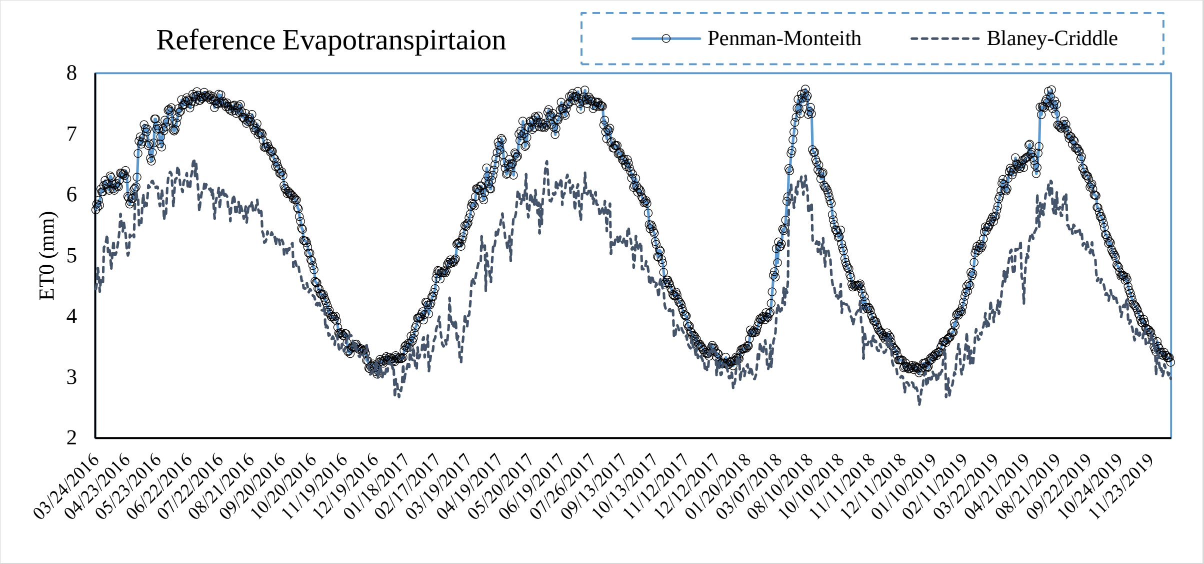

Fig. 5. 5 ET - Blaney-Criddle method (MAR 24, 2016 to DEC 12, 2019)

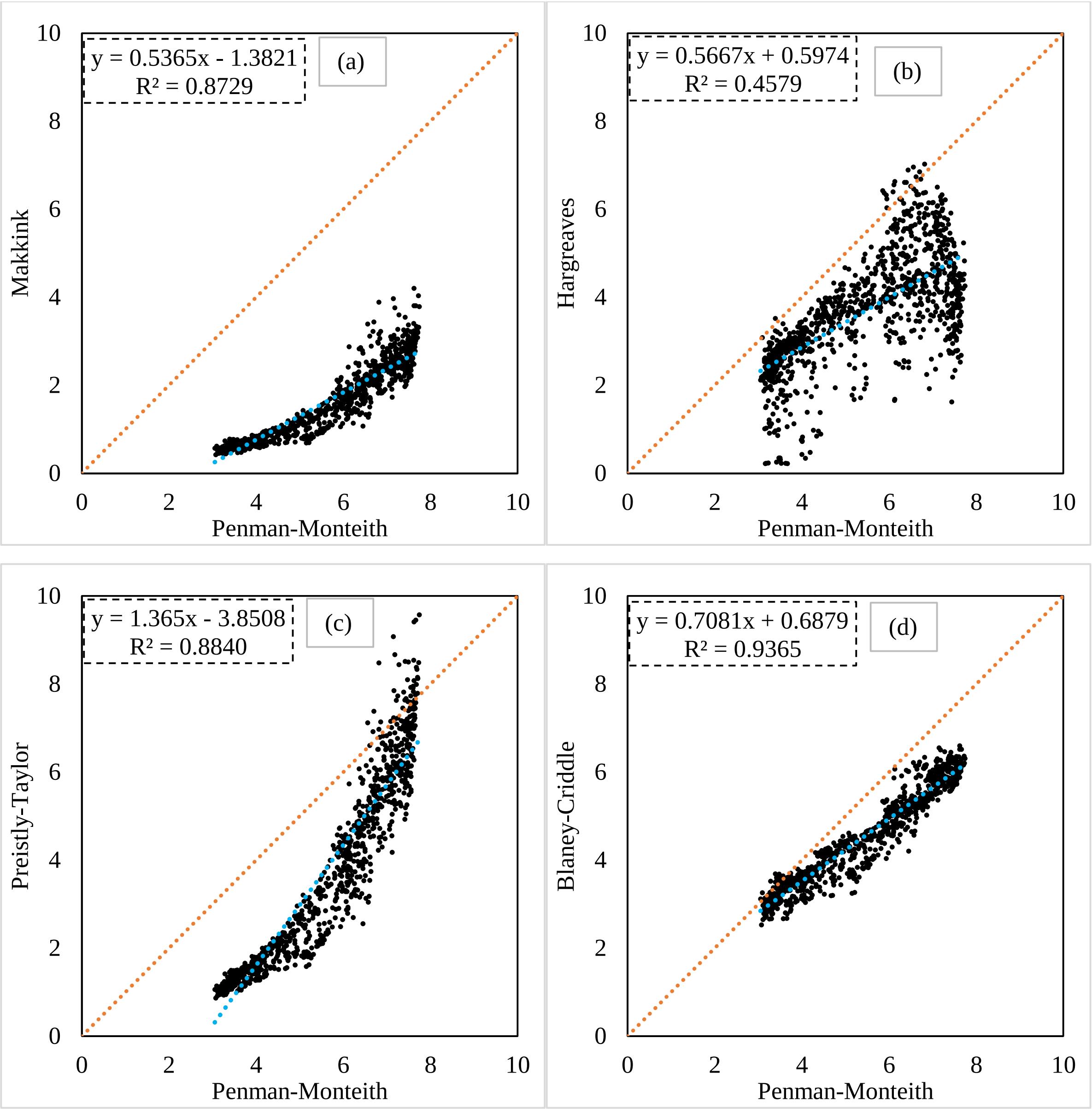

Fig. 5. 6 Correlation plots of a) Blaney Criddle, b) Priestly-Taylor, c) Hargreaves, and d) Makkink methods with FAO 56 Penman-Monteith method

5.3 REMOTE SENSING BASED METHOD

5.3.1 SEBAL Method

Surface Energy Balance Algorithm for Land (SEBAL) is an image processing model that estimates actual ET_0 by solving the terms of the surface energy balance derived from the visible, near-IR, and thermal-IR bands of the electromagnetic spectrum. In the SEBAL model, ET_0 is computed from satellite images and climate data using the surface energy balance. Since the satellite image provides information for the overpass time only, SEBAL computes net radiation (Rn), sensible heat flux (H) and soil heat flux (G) for every pixel and the latent heat flux (LE) is acquired as a residual in energy balance.

$$R_n = LE + H + G \qquad \ldots (5.6)$$

Where *Rn* is net radiation at the surface, *LE* is latent heat flux, *H* is sensible heat flux to the air, and *G* is soil heat flux.

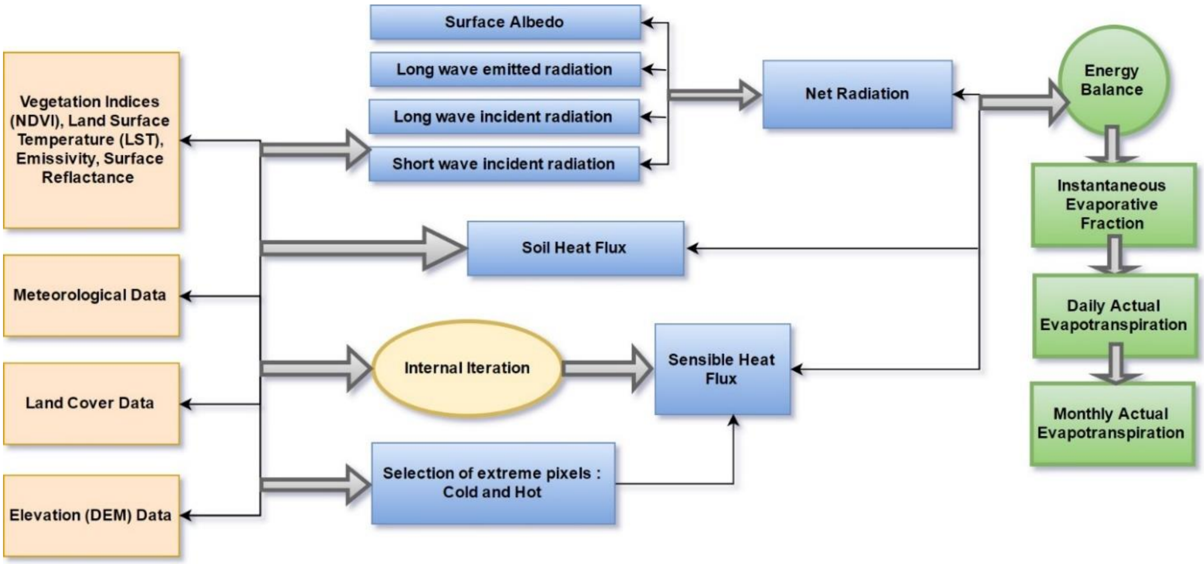

Fig. 5. 7 Flowchart depicting the working of SEBAL model

5.2.1.1 Net Radiation

The first step in the SEBAL procedure is to compute the net surface radiation flux (R_n) using the surface radiation balance equation 5.7.

$$R_n = (1 - \alpha)R_S + R_L \downarrow - R_L \uparrow - (1 - e_0)R_L \downarrow \qquad \ldots (5.7)$$

Figure 5.6. shows the net radiation model. The model has three inputs which are: a corrected Landsat image, land surface temperature, digital elevation model, and climate data as parameters. Then the model calculates surface albedo and NDVI from the corrected satellite image. The land surface temperature was calculated using ArcGIS software, and in the model, it was considered as one of the input data.

After that, the NDVI layer was used to calculate the surface emissivity. The surface albedo was then corrected for the elevation variations using the digital elevation model. Surface emissivity was then used to estimate the outgoing longwave radiation. On the other hand, digital elevation model was used to calculate atmospheric transmissivity and then atmospheric emissivity. At the same time, climate data were used for the near-surface temperature layer establishing to be used after that with atmospheric emissivity to estimate the incoming longwave radiation. The incoming shortwave radiation was estimated based on the atmospheric transmissivity, and the outgoing shortwave radiation was estimated from the corrected surface albedo and the incoming longwave radiation. Finally, the four radiation components, incoming and outgoing, were used to estimate the net radiation. Figure 5.7 shows the land surface temperature and net radiation input for the SEBAL model.

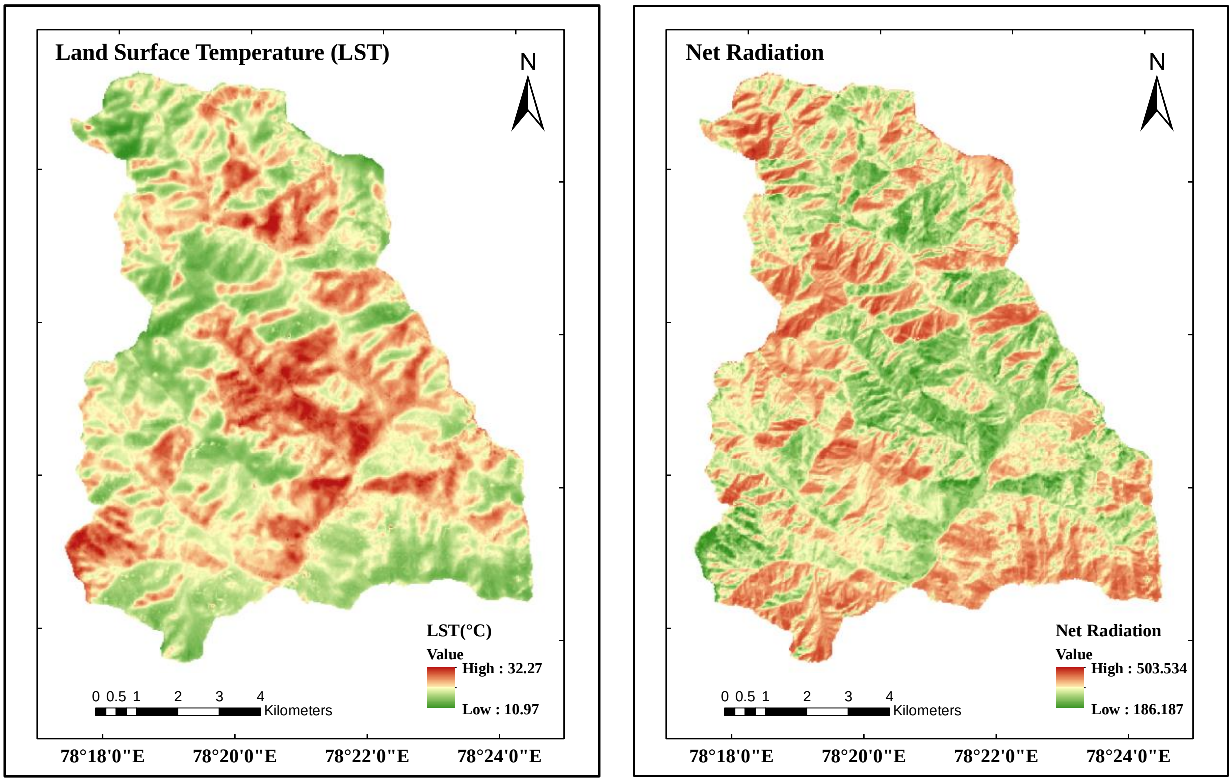

(a) (b)

Fig. 5. 8 a) Land Surface Temperature (LST), b) Net radiation, components of SEBAL input (March 05th 2017)

5.2.1.2 Soil Heat Flux

For soil heat flux calculation firstly the ratio G/R_n is computed using the following equation 5.8 representing values near midday,

$$G/R_n = \left({}^{T_0}/_{\alpha}\right)(0.0038\alpha + 0.007\alpha^2)(1 - 0.98NDVI^4) \qquad \ldots (5.8)$$

where T_0 is the surface temperature (°C), α is the surface albedo, and *NDVI* is the Normalized Difference Vegetation Index. G/R_n for turbid or shallow water bodies will be less than 0.5 due to the absorption of shortwave radiation more near the water surface. Condition of soil heat flux can be seen by the map shown in figure 5.9.

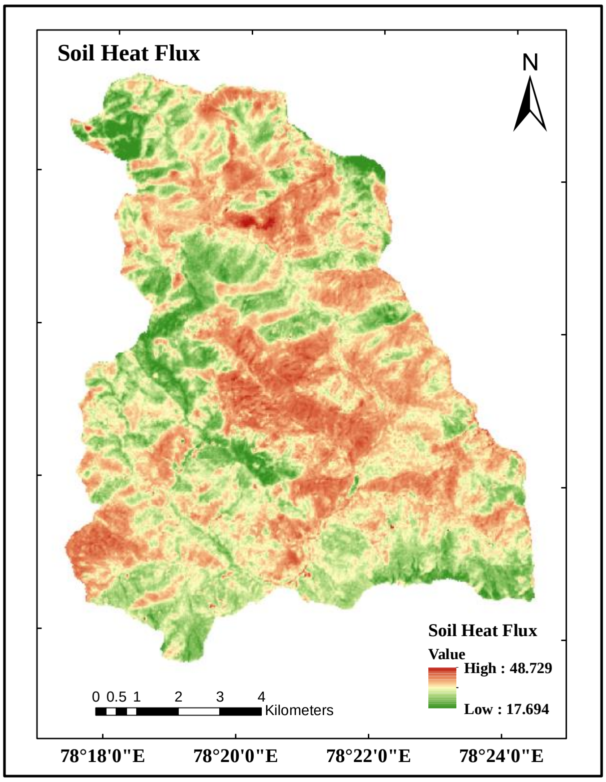

Fig. 5. 9 Soil Heat Flux, component of SEBAL input (March 05th 2017)

5.2.1.3 Sensible Heat Flux

A linear relationship exists between the sensible heat flux (*H*) and the difference between surface temperature and air temperature (*dT*). It is computed using equation 5.9 of heat transport

$$H = \left(\rho \times c_p \times dT\right)/r_{ah} \qquad \dots (5.9)$$

where ρ is air density (kg/m^3), c_p is air specific heat (1004 J/kg/K), dT (K) is the temperature difference ($T_1 - T_2$) air temperature between the evaporating surface and a reference height above the evaporating surface (usually 2 m), and r_{ah} is the aerodynamic resistance to heat transport (s/m). For computing, sensible heat flux (H) near-surface temperature difference (*dT*) for each pixel needs to be defined. The air temperature at each pixel is unknown, along with explicit values for T_{z1} and T_{z2}. SEBAL computes dT for each pixel by assuming a linear relationship between dT and T_0, equation 5.10.

$$dT = b + a\,T_0 \qquad \dots (5.10)$$

In SEBAL, *dT* is calculated at two extreme "indicator" pixels by assuming values for H at the reference pixels (wet and dry). The value of *dT* is presumed to be zero at the wet (T_{cold}) pixel. After the dry pixel is identified, dT of the pixel can be calculated by the equation of sensible heat, assuming an initial value for aerodynamic resistance. Figure 5.10 shows the spatial variation of the sensible heat flux in the catchment.

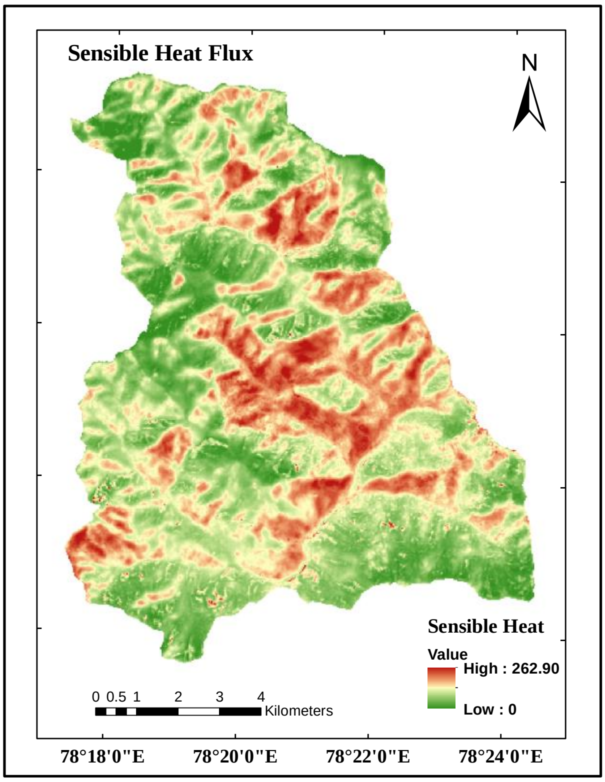

Fig. 5. 10 Sensible Heat Flux, a component of SEBAL input (March 05th 2017)

5.3.2 SEBAL Derived ET$_0$

The data described in the previous section were used to run the SEBAL model to assess ET$_0$ for both the watershed. The ET is estimated for all the pixels of the Henval watershed. The spatial variation of ET over the Henval watershed for all the cloud-free satellite images of Kharif (2016-2018) seasons and Rabi (2017-18) seasons is shown in Fig. 5.11. It can be observed from Fig. 11 that ET values are higher during the Kharif season and later half of the Rabi season. This coincides with a higher temperature in the study area. During the Kharif season, the study area also receives substantial rainfall that contributes to higher ET values.

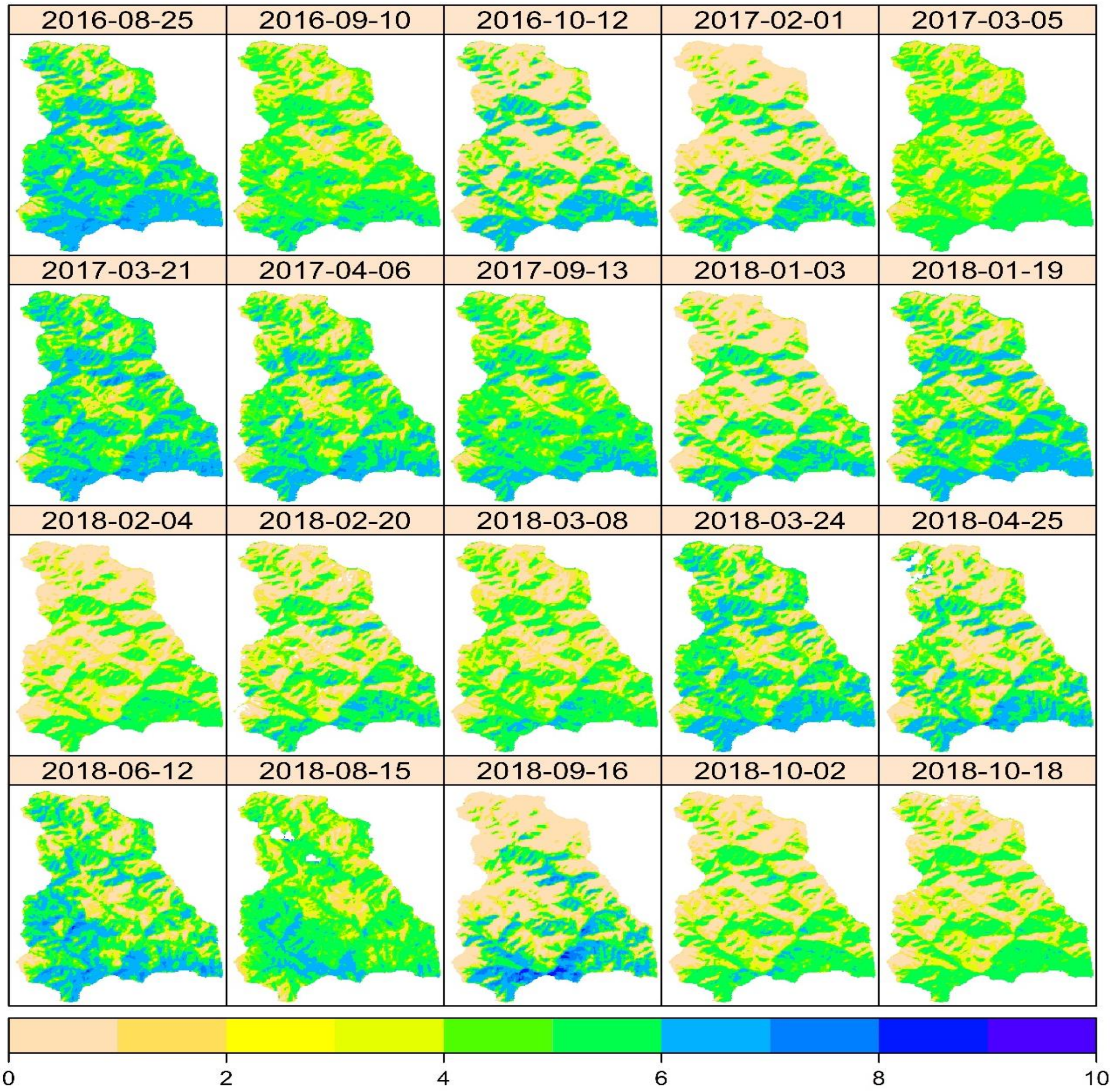

Fig. 5. 11 Daily evapotranspiration (ET) of the catchment area for cloud-free images during 2016-18

The actual ET_0 maps generated from the surface temperature (LST) images using SEBAL model shows the spatial characteristics of evaporation over time. The map shows the spatial variation of ET_0 in the catchment. ET_0 is classified into nine different classes to get an integer value for a particular region of preference. This is very much evident from the maps that zero or close to zero ET_0 portion increases in the winters, and this portion of the catchment is generally the valley region in the catchment. For this aspect also plays a significant role. From the maps, we can say that the south-facing aspect is the one which shows very fewer ET_0 values in the winters, which is a noticeable reduction in the hilly topology.

5.4 DIRECT MEASUREMENT

5.4.1 Eddy Covariance Method

The eddy covariance method provides measurements of gas emission and consumption rates, and also allows measurements of momentum, sensible heat, and latent heat (*e.g.*, evapotranspiration, evaporative water loss, *etc.*) fluxes integrated over areas of various sizes. Eddy covariance method is one of the most accurate, direct and defensible approaches available to date for determining emission and consumption rates of various gases and water vapour over areas with sizes ranging from a few hundred to millions of square meters. The method relies on direct and fast measurements of actual gas transport by a 3-dimensional wind in real-time in situ, resulting in calculations of turbulent fluxes within the atmospheric boundary layer. Airflow can be imagined as a horizontal flow of numerous rotating eddies. Each eddy has 3-D components, including the vertical movement of the air. The situation looks chaotic at first, but these components can be easily measured from the tower. At one moment (time 1), eddy number 1 moves air parcel c1 downward with the speed w1. At the next moment (time 2) at the same point, eddy number 2 moves air parcel c2 upward with speed w2 (Figure 5.12). Each air parcel has its characteristics, such as gas concentration, temperature, humidity, etc. If we can measure these characteristics and the speed of the vertical air movement, we will know the vertical upward or downward fluxes of gas and water vapour concentrations, temperature, and humidity.

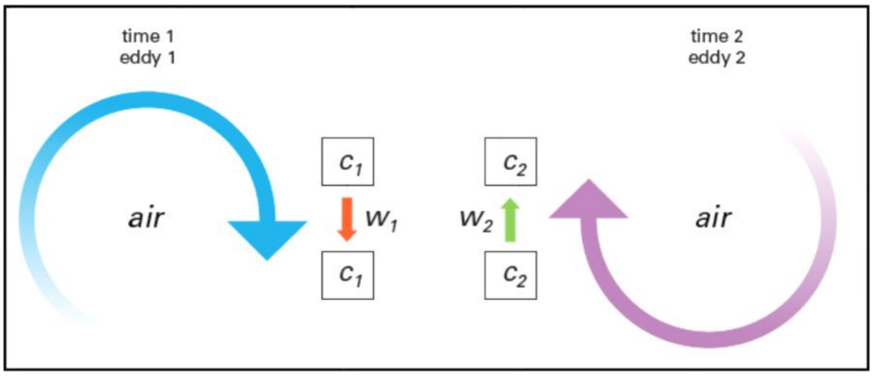

Fig. 5. 12 Eddy movement with time

5.3.1.1 Basic assumptions

Eddy covariance method works under the underlying assumptions stated below:

1. Measurements at a point can represent an upwind area,
2. Measurements are done inside the boundary layer of interest,
3. Flux is fully turbulent, and eddies do most of the net vertical transfer,

4. The terrain is horizontal and uniform, an average of fluctuations of w’ is zero, air density fluctuations, flow convergence and divergence are negligible,
5. Instruments can detect minimal changes at high frequency,
6. The installation structure or the instruments do not distort airflow.

5.3.1.2 Mathematical principle

Vertical flux can be represented as the covariance between measurements of vertical velocity, the upward and downward movements, and the concentration of the entity of interest. Turbulent fluctuations occur very rapidly, so measurements of up-and-down movements and of the number of molecules should be done very rapidly. In turbulent flow, vertical flux can be presented as equation 5.11.

$$F = \overline{\rho_d w s} \qquad \ldots (5.11)$$

s is the dry mole fraction of the gas of interest in the air. Using Reynolds decomposition breaking terms into means and deviations equation 5.12 is obtained.

$$F = \overline{(\overline{\rho_d} + \rho_d{}')(\overline{w} + w')(\bar{s} + s')} \qquad \ldots (5.12)$$

On simplifying the above equation under assumptions stated earlier, eddy flux can be represented as equation 5.13.

$$F \approx \overline{\rho_d}\,\overline{w's'} \qquad \ldots (5.13)$$

The eddy flux is computed from the mean dry air density multiplied by the mean covariance between deviations in instantaneous vertical wind speed and dry mole fraction (e.g., mixing ratio). Sensible heat flux (H) is equal to the mean air density multiplied by the covariance between deviations in instantaneous vertical wind speed and temperature (equation 5.14); conversion to energy units is accomplished by including the specific heat term.

$$\mathrm{H} = \overline{\rho} C_p \overline{w'T'} \qquad \ldots (5.14)$$

The water vapour flux is often computed in energy units (Wm^{-2}) and called latent heat flux (LE). Latent heat flux (equation 5.15) represents the energy used in the process of evaporation, transpiration, or evapotranspiration. Latent heat flux, when converted to volume or mass units, is referred to as evapotranspiration rate (ET), evaporation rate (over wet non-vegetated surfaces), or evaporative water loss.

$$LE \equiv \lambda E = \lambda \frac{M_w/M_a}{\overline{P}} \overline{\rho_d}\,\overline{w'e'} \qquad \ldots (5.15)$$

5.4.2 Data Processing

The data processing of EC flux data can be divided into three segments: data collection (without processing), data processing (after collection), and data collection with on-the-fly processing (simultaneously or within a few seconds after the data collection). It is crucial to distinguish comprehensive software, designed to obtain actual flux from more straightforward covariance calculators. The calculators compute the value of covariance between wind speed and gas concentration. Comprehensive processing software includes free fully supported and documented open-source software such as EddyPro; free partially supported open-source software such as ECO2S, EddyUH, Flux Calculator from JapanFlux, and ECPack; free closed-source packages such as EdiRe, TK3, AltEddy, etc.; customized commercial packages; and many other programs.

One of the latest comprehensive software packages developed explicitly for eddy covariance data processing is **EddyPro**. It is open-source software, fully documented, maintained, and supported by LI-COR Biosciences. EddyPro computes fluxes of energy, momentum, carbon dioxide, water vapour, methane, and other trace gases, and also includes “Biomet” data (e.g., slow bio-meteorological data on incoming, outgoing and net solar radiation, soil temperature and moisture at different levels, weather parameters, etc.). It offers two operational modes **express** and **advanced**. In express mode, very minimal user configuration is required. The data are processed with just a few clicks using default settings, developed to provide reasonable and safe processing assumptions, but not custom-fit to the site conditions. This mode is useful for most standard sites and setups. In advanced mode, a more experienced researcher can pre-configure the software, and fine-tune the entire processing workflow as desired. Advanced mode is useful for non-standard sites and setups. It is also useful in situations when the researcher has particular preferences in data processing; for example, broadening criteria for de-spiking of fast gas concentration, adding angle-of-attack corrections, or using a planar fit rotation instead of double rotation, etc.

Other than the open-source data processing software from Campbell scientific and Licor. There are some sited packages and modules available in Python and R languages developed by different subject experts viz. Fluxpart, ReddyPro, etc. Fluxpart is a python module used in processing the raw input eddy covariance data. It partitions the eddy covariance water vapour and carbon dioxide fluxes into stomatal (transpiration and photosynthesis) and nonstomatal (evaporation and respiration) components (T.H. Skaggs et al. 2018, T.M. Scanlon et al. 2010).

The Fluxpart algorithm processes high-frequency data to determine average interval values for the water vapour and Carbon dioxide fluxes. Some notations are given below in the equations:

$F_q= <w'q'>$ … (5.16)

$F_{qe}= <w'qe'>$ … (5.17)

$F_{qt}= <w'qt'>$ … (5.18)

$F_c= <w'c'>$ … (5.19)

$F_{cr}= <w'cr'>$ … (5.20)

$F_{cp}= <w'cp'>$ … (5.21)

As per the algorithm these equations exist:

$F_q = F_{qe} + F_{qt}$ … (5.22)

$F_c = F_{cr} + F_{cp}$ … (5.23)

$F_{qe} > 0$ … (5.24)

$F_{qt} > 0$ … (5.25)

$F_{cr} > 0$ … (5.26)

$F_{cp} < 0$ … (5.27)

$WUE= F_{cp} / F_{qt}$ … (5.28)

Where, w is the vertical wind component, q is the water vapour mass concentration, c is the Carbon dioxide mass concentration, F_q is Total water vapour flux, F_{qe} is a non-stomatal component of water vapour (evaporation), F_{qt} is a stomatal component of water vapour flux (transpiration), F_c is total CO_2 flux, F_{cr} is a non-stomatal component of CO_2 flux (respiration), F_{cp} is a stomatal component of CO_2 flux (photosynthesis), and WUE is water use efficiency.

The angle brackets in the equations are time averaging period to calculate flux, which is 30 minutes for this study.

The full procedure involves in partitioning is:

- Reading high frequency (10 Hz) data of eddy covariance
- Basic quality assessment and quality checking of data (e.g. Spikes)
- Data transformation (Unit conversion, external effects conversions)

- Seeking a physically acceptable partitioning solution, progressively removing low-frequency components from data as needed to conform with flux variance similarity assumptions

5.3.2.1 Gap filling

The high frequency (10 Hz) eddy covariance data usually is averaged to 30 minutes of time interval to drive logical inferences. The chances of having gaps in data are frequent and it is reported (Hui D et al., 2003) that, 35% of data is usually remain missed due system failure, power failure or others reasons.

Therefore, gap-filling techniques must be applied to get a complete data series. There are many methods available, but most of them need specific ground observed data viz. photosynthetic photon flux density, which is not available for the current study area and also they are site-specific methods. A prevalent and mostly used method is Mean Diurnal Variation (MDV).

5.3.2.2 Mean Diurnal Variation

This method replaces the missing values by the mean of the time period (half hours) based on the next days. Usually, the window size of 4-15 days is used for averaging. Four days often are not enough to determine a mean from measurements because the data may be missing for four or fewer days. Data windows of days 7 and 14 are used for day time and night time, respectively. In this method, two different algorithms are used based on window sizes (1) Independent window, and (2) Gliding window.

Equations for both the algorithm is given below:

Independent window

$$\overline{X_{h,\imath}} = \begin{bmatrix} \overline{X_{1,(k=1,\ldots,n)}} & \overline{X_{2,(k=1,\ldots,n)}} & \cdots & \overline{X_{48,(k=\imath nt\left(\frac{d}{n}\right)n,\ldots,d)}} \\ \overline{X_{1,(k=n+1,\ldots,2n)}} & \overline{\overline{X_{2,(k=n+1,\ldots,2n)}}} & \cdots & \overline{X_{48,(k=\imath nt\left(\frac{d}{n}\right)n,\ldots,d)}} \\ \vdots & \vdots & \cdots & \vdots \\ \overline{X_{1,(k=\imath nt\left(\frac{d}{n}\right)n,\ldots,d)}} & \overline{X_{2,(k=\imath nt\left(\frac{d}{n}\right)n,\ldots,d)}} & \cdots & \overline{X_{48,(k=\imath nt\left(\frac{d}{n}\right)n,\ldots,d)}} \end{bmatrix} \quad \ldots (5.29)$$

where *h* is the index for the half-hour (*h* = {1,2, …48}), *i* the index for the averaging window where *i* = {1, … integer (d /n) +1}, *n* is the window size, *d* is the number of days per year.

Gliding window

$$\overline{X_{h,\iota}} = \begin{bmatrix} \overline{X_{1,(k=1,\ldots,n)}} & \overline{X_{2,(k=1,\ldots,n)}} & \cdots & \overline{X_{48,(k=\iota nt\left(\frac{d}{n}\right)n,\ldots,d)}} \\ \overline{X_{1,(k=n+1,\ldots,2n)}} & \overline{X_{2,(k=n+1,\ldots,2n)}} & \cdots & \overline{X_{48,(k=\iota nt\left(\frac{d}{n}\right)n,\ldots,d)}} \\ \vdots & \vdots & \cdots & \vdots \\ \overline{X_{1,(k=d-n+1,\ldots,d)}} & \overline{X_{2,(k=d-n+1,\ldots,d)}} & \cdots & \overline{X_{48,(k=d-n+1,\ldots,d)}} \end{bmatrix} \qquad \ldots (5.30)$$

where $i = \{1, \ldots d\text{-}n+1\}$, n is the window size, d is the number of days per year, h is the index for the half-hour ($h = \{1,2, \ldots 48\}$).

5.4.3 Actual ET Estimations by Eddy Covariance Method

High-frequency data from EC flux tower for a period of one year (Jan 2018 to Jan 2019) has been used to estimate the actual ET from the Henval valley at Nagani station. Initially, the results are shown without gap-filling; hence the graph has less number of data points in figure 5.13 and also the days (Julian days) are not regular. The gaps were filled with MDV method to get complete data series.

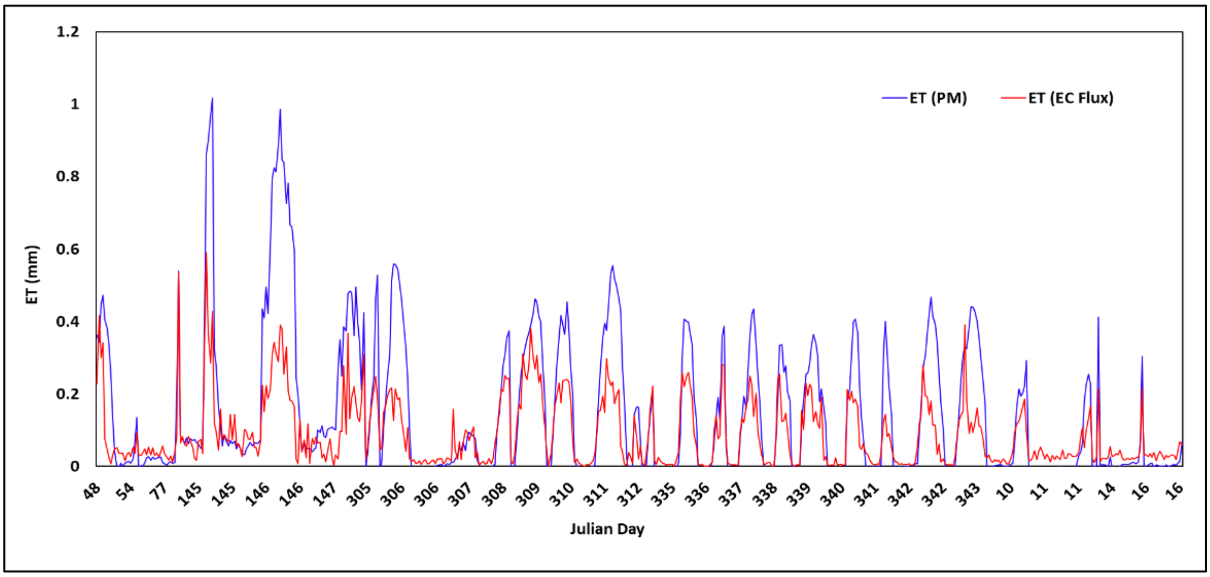

Fig. 5. 13 Half hourly time series of ET (PM) and ET (EC)

In figure 5.14 and 5.15, the results are shown before and after gap filling. In figure 5.14, The R^2 is 0.68, but the actual ET (EC) is under predicting this may due to that the PM ET is reference evapotranspiration. In figure 5.15, after gap-filling, the R^2 has been improved and reached up to 0.74.

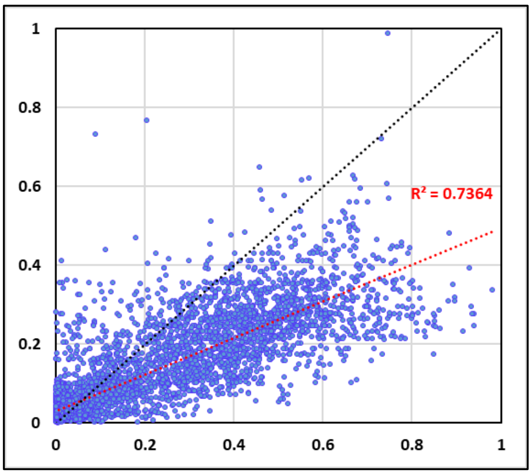

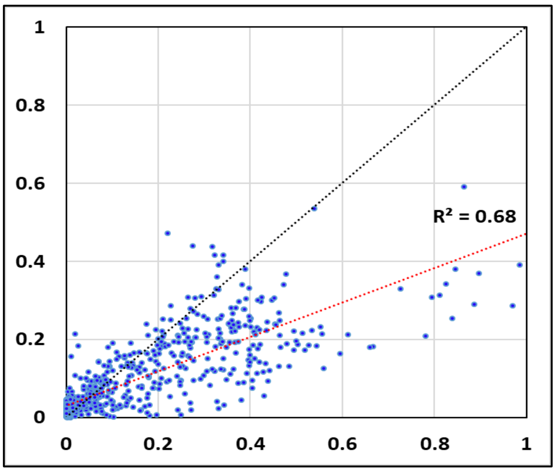

Fig.5. 14 Scatterplot of ET (PM) and ET (EC)
(After gap filling)

Fig.5. 15 Scatterplot of ET (PM) and ET (EC)
(Before gap filling)

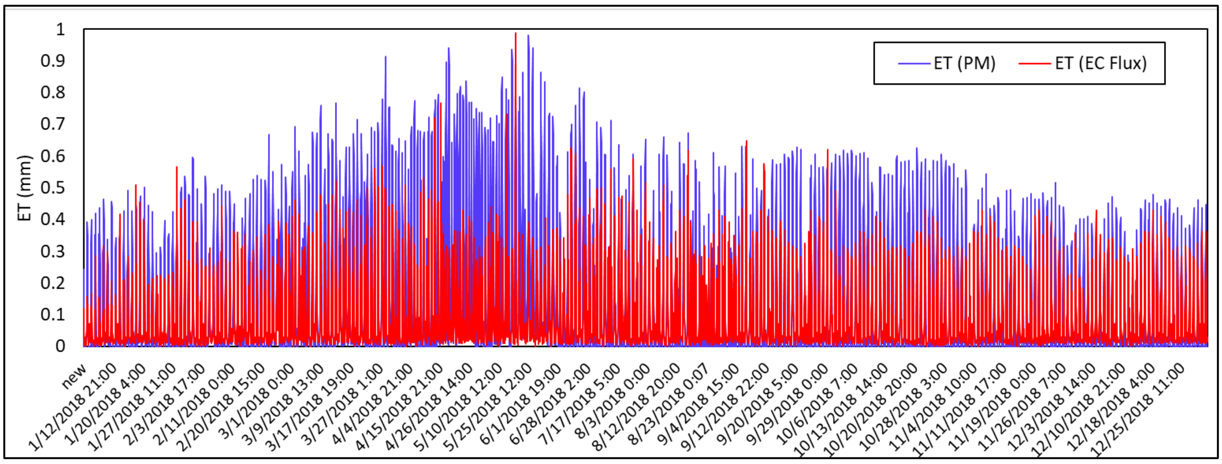

Fig. 5. 14 Half hourly time series of ET (PM) and ET (EC) (with gap filling)

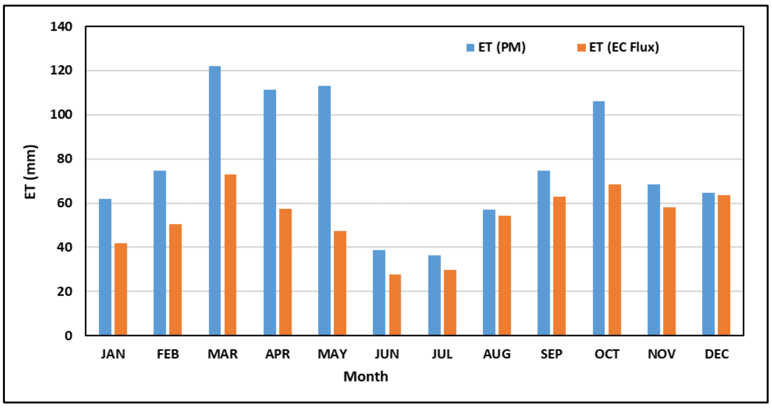

Fig. 5. 15 Monthly variations of ET (PM) and ET (EC) for the year 2018

In figure 5.17, last months of 2018 gave better results specifically in December due to less hourly variation. Overall the Penman-Monteith method has over-predicted ET as compared to the eddy covariance method.

CHAPTER 06: WATER BALANCE

6.1 GENERAL

Water balance of a system or a watershed/ basin can be described by the flow of water in and out of it. It's the closed water cycle system in equation form: precipitation plus incoming groundwater minus the sum of leaving groundwater and runoff equals storage. It puts all together with the inputs and outputs in the watershed "system." Water balance equation uses the principles of conservation of mass in a closed system, wherein any water entering a system (via precipitation), must be transferred into either evaporation, surface runoff (eventually reaching the channel and leaving in the form of river discharge), or stored in the ground. This equation requires the system to be closed, and where it isn't (for example, when surface runoff contributes to a different basin), this must be taken into account. A water balance can be used to help manage water supply and predict where there may be water shortages. It is also used in irrigation planning, water availability assessment, flood control, etc. There are a variety of simple water balance models available to describe runoff (or available water) based on precipitation, and these models have been used with success to help quantify water availability based on monthly precipitation input and estimates of evapotranspiration losses. In this study, a widespread hydrological model Soil and Water Assessment Tool (SWAT) has been used to compute the water balance of the catchment.

6.2 DESCRIPTION OF SWAT MODEL

The SWAT model is a comprehensive, conceptual, continuous-time, distributed river basin and deterministic model that can simulate surface and sub-surface flow, soil erosion and sediment deposition, nutrients and their movement through the watershed. It requires a large number of input parameters varying widely in space and time while transforming input into the output. It is a freely available model which is useful in conducting hydrological assessment studies. This tool can be used in areas like water resource planning, management and decision-making policies.

The hydrologic components of the SWAT model are based on the water balance equation

$$SW_t = SW_0 + \sum_{i=1}^{i}(R_{day} - Q_{surf} - E_a - w_{seep} - Q_{gw}) \quad \text{... (6.1)}$$

where SW_t is the final soil water content (mm H2O), SW_0 is the initial soil water content on the day i (mm H2O), t is the time (days), R_{day} is the amount of precipitation on the day i (mm

H2O), Q_{surf} is the amount of surface runoff on the day i (mm H2O), E_a is the amount of evapotranspiration on the day i (mm H2O), w_{seep} is the amount of water entering the vadose zone from the soil profile on the day i (mm H2O), and Q_{gw} is t

he amount of return flow on the day i (mm H2O). Surface runoff is predicted for the daily rainfall by using SCS curve number method (USDA-SCS, 1972). SCS curve number method is an empirical, conceptual method developed for the computation of surface runoff under varying soil types and land uses.

$$Q_{surf} = \frac{[R_{day} - 0.2S]^2}{R_{day} - 0.8S} \qquad \ldots (6.2)$$

Where, S is the retention parameter (mm of H_2O). I_a is the initial abstraction loss (mm of H2O). The retention parameter S is calculated using the following equation

$$S = 25.4\left(\frac{1000}{CN} - 10\right) \qquad \ldots (6.3)$$

Where CN is the curve number for the day, and it is computed using the following equation 3.

$$CN = \frac{25400}{(S + 254)} \qquad \ldots (6.4)$$

SWAT model requires spatial data like DEM, LULC MAP, SOIL MAP and METEOROLOGICAL DATA. The DEM of the study area was downloaded from https://vertex.daac.asf.alaska.edu/, where elevation data at 12.5 m resolution acquired through ALOS PALSAR is available for the globe. The Land Use data was prepared using the LANDSAT image downloaded from the USGS Archive, http://glovis.usgs.gov/. The image is then projected into proper projection same as the DEM having the same datum using ArcGIS. The land use land cover map of Henval watershed is shown in Fig. (6.2). The soil map with a spatial resolution of 1:5000,000 were obtained from the Food and Agriculture Organization (FAO), as shown in Fig. (6.1).

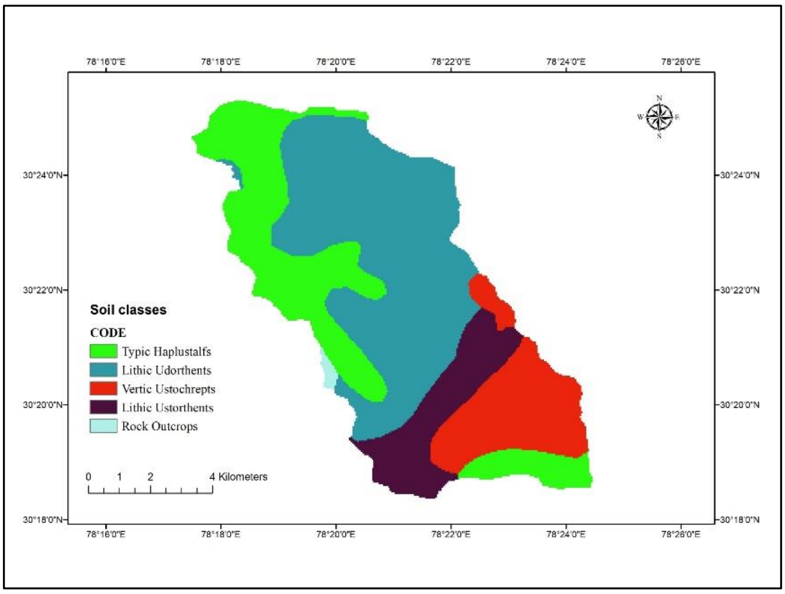

Fig. 6. 1 Soil classes map of Henval Watershed

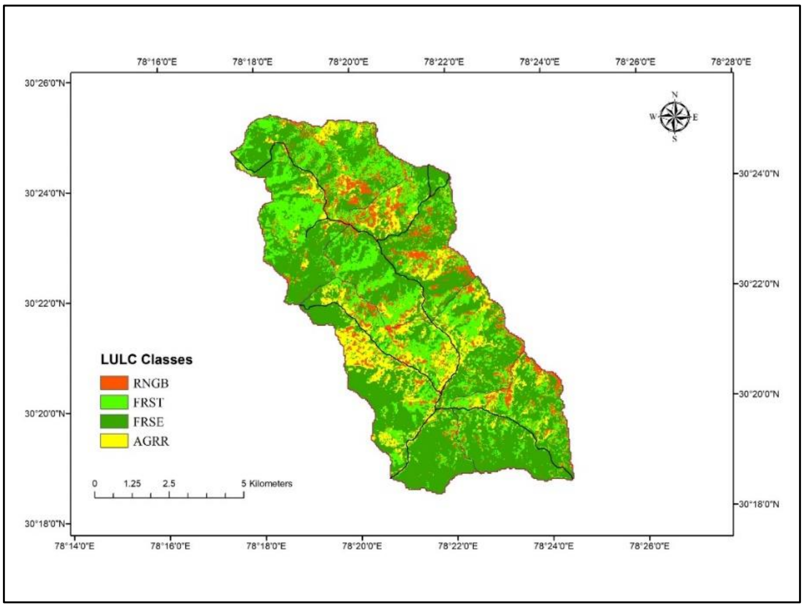

Fig. 6. 2 LULC classes map of Henval watershed

The meteorological and hydrological data required for the study was procured from the AWS tower installed in Nagani village. Temperature, precipitation, wind speed, relative humidity and solar radiation for Henval watershed were obtained from the AWS. The daily discharge for the study was obtained from the broad crested compound rectangular weir constructed at the outlet of Henval stream and an automatic water level recorder installed across the Henval river at the outlet. The cross-sectional diagram of the broad crested rectangular weir is shown in Fig. (6.3). A compound rectangular-rectangular broad crested weir for monitoring of discharge was constructed, and its discharge can be calculated using the following equation

$$Q_t = \frac{2}{3} C_{rd1}\sqrt{2g}(2b_1)h_1^{3/2} + \frac{2}{3} C_{rd2}\sqrt{2g}b_2 h_2^{3/2} \quad \ldots (6.5)$$

$$C_{rd} = \frac{0.611+2.23(\frac{B}{b}-1)^{0.7}}{1+3.8(\frac{B}{b}-1)^{0.7}} + \frac{0.075+0.011(\frac{B}{b}-1)^{1.46}}{1+4.8(\frac{B}{b}-1)^{1.46}}\frac{h}{P} \quad \ldots (6.6)$$

Where, C_{rd}= discharge coefficient of the rectangular weir; g= gravitational acceleration; b = weir length; h = water head on the weir crest; B = channel width and P = weir height.

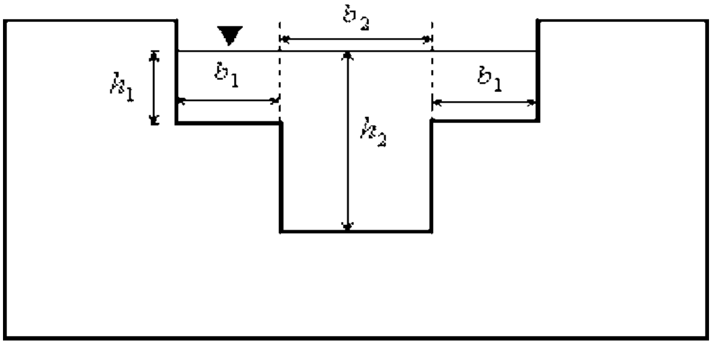

Fig. 6. 3 Cross-section of the compound rectangular-rectangular broad crested weir.

6.3 MODEL SET-UP

SWAT model was set up using ArcGIS SWAT interface. SWAT 2012 was used to divide the watershed into sub-basins and then into HRUs based on the land use, soil type and slope group. Using the DEM, ArcSWAT automatically delineates the watershed with defining the streamlines and the outlet point. Also, the watershed was sub-divided into three sub-basins. The HRU analysis in ArcSWAT reclassifies the land use, soil type and slope of the watershed. After characterization of the land use and soil maps in the basin, multiple slope class were selected. In this study four slope classes are used; they are 0-25%, 25-50%, 50-75% and 75-99.99% respectively. Then the Hydrological response units (HRU) was created by the model. Also, the threshold percentage of the land, soil and slope factors for the creation of the HRU were given as 10%, 10% and 10% respectively. Hence, the whole watershed was divided into 96 HRUs and 10 sub-watersheds. Then, the SWAT model was run for estimation of runoff for Henval watershed for the period January 2016 to December 2018.

6.4 MODEL CALIBRATION AND VALIDATION

For calibration and validation, SWAT Calibration Uncertainty Program (SWAT-CUP) using Sequential uncertainty fitting (SUFI -2) program has been used. SWAT-CUP is a public domain computer program for calibration, validation and uncertainty analysis of SWAT. SUFI-

2 required the minimum number of simulations to obtain better results. The model was calibrated for the period of 01/01/2016 –31/12/2017 (2 years), and validation was done for the period of 01/01/2018 –31/12/2018 (1 year) for the study area. The parameter affecting the model calibration for the model were selected based on the sensitivity analysis involving the parameters. The calibration of the model was performed using the observed data for the period of 01/01/2016 –31/12/2017 by adjusting the most sensitive parameters, as shown in Table 6.1.

Table 6. 1 Range of parameter values used for modelling of Henval watershed

S. No.	Parameter code	Description	Fitted value	Min. value	Max. value
1	CN2	SCS runoff curve number	-0.19	-0.2	0.2
2	ALPHA_BF	Base-flow alpha factor	0.89	0.0	1.0
3	GW_DELAY	Groundwater delay	101.39	30.0	450.0
4	GWQMN	Threshold depth of water in the shallow aquifer required for return flow to occur	0.7	0.0	2.0
5	SOL_AWC	Available water capacity of the soil layer	0.53	0.0	1.0
6	HRU_SLP	Average slope steepness	486.50	50.0	500
7	OV_N	Manning's "n" value for overland flow	1.36	-0.2	2.0
8	SLSUBBSN	Average slope length	0.65	-0.2	2.0
9	ESCO	Soil evaporation compensation factor	0.79	0.0	1.0

Then, the model was calibrated and validated with the observed values. Fig. 6.4 shows the time series plot of observed and predicted runoff for the calibration period for the Henval watershed. The calibration was done for 2 years (2016–2017). The R^2 value for the calibration period was found to be 0.63, and NSE value was to be 0.55. From the time series plot, it can be seen that even though the simulated runoff is underestimated, it follows the same trend as the observed runoff. Also, the rainfall value matches with the observed and simulated runoff. With the calibrated parameter values, the model was validated for the period from 01/01/2018 to 31/12/2018. Fig. 6.5 shows the time series plot of observed and predicted runoff for the validation period for the Henval watershed. The R^2 value for the validation period was found to be 0.58, and NSE value was found to be 0.53. During the validation of the model, the hydrological response is delayed, and from the rainfall-runoff plot, it can be seen that the precipitation over the watershed, at first, saturate the dry surface of the watershed and then the streamflow is initiated.

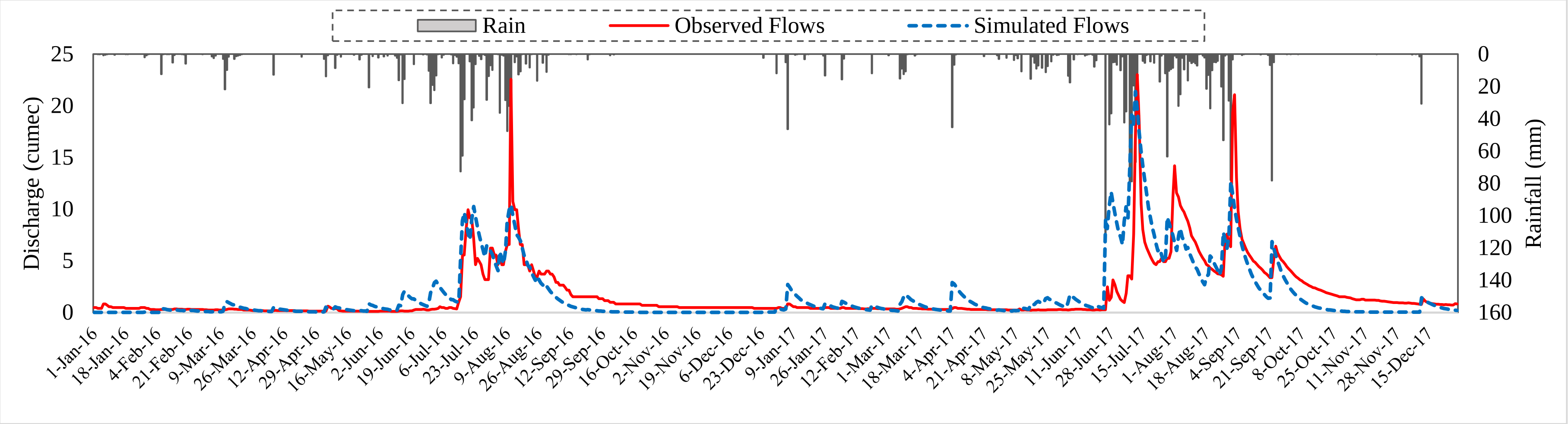

Fig. 6. 4 Time series plot of observed and simulated runoff with its rainfall for the calibration period.

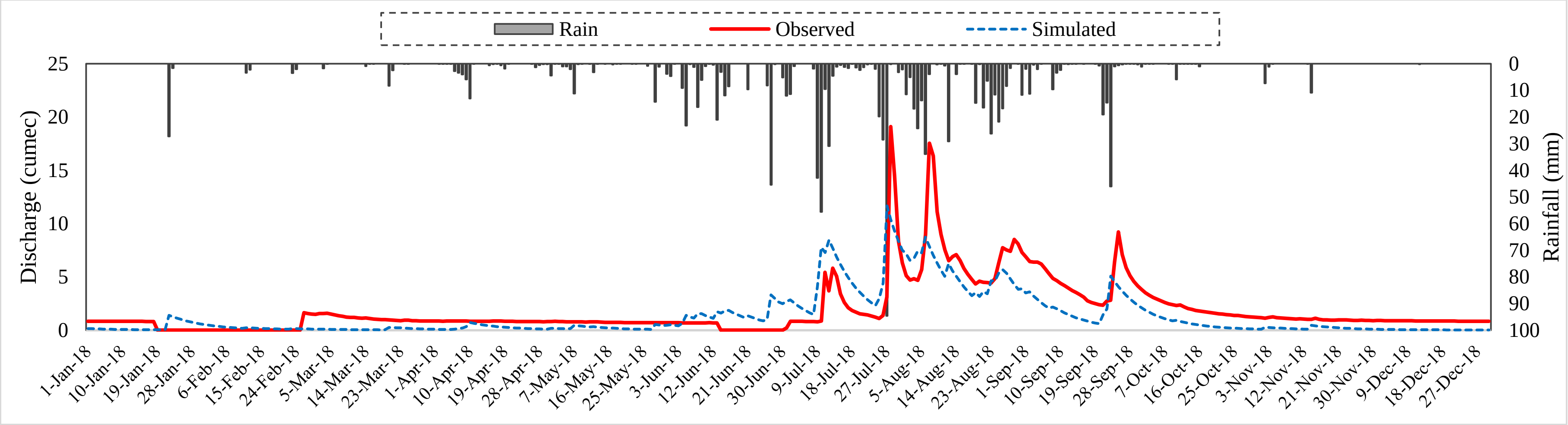

Fig. 6. 5 Time series plot of observed and simulated runoff with rainfall for the validation period.

6.5 WATER BALANCE OF THE WATERSHED

Water Balance is defined as the numerical calculation accounting for the inputs to, outputs from, and changes in the volume of water in the various components (e.g. reservoir, river, aquifer) of the hydrological cycle, within a specified hydrological unit (e.g. river basin) and during a specified time unit (e.g. month/year), occurring both naturally and as a result of the human-induced water abstractions and returns. Water in the catchment is always balanced, and its components are influenced by the morphology of watershed, climatic conditions, soil characteristics and land use land cover. It is simply based on the concept of change in storage of water. It helps in the development of River Basin Management Plans by providing a coherent framework to cross-evaluate the information on drivers, pressures and impacts on water quantity and provides a sound basis to the quantitative management of water resources. Estimation of the water balance components is a complicated task and can be achieved either using water balance models or hydrological models which have been developed at various time scales. The hydrologic processes are very complex, and its understanding of the watershed model is essential. There exist numerous physically-based distributed hydrological models, and among them, SWAT is one of the widely used models (Neitsch et al., 2005).

The essential hydrologic elements from the water management point of view are surface runoff, lateral flow, baseflow and evapotranspiration. In this study, the SWAT model is used to evaluate water balance components, and the model is calibrated and validated as well. The various components of the hydrologic cycle of the Henval watershed are shown in Fig. 6.6.

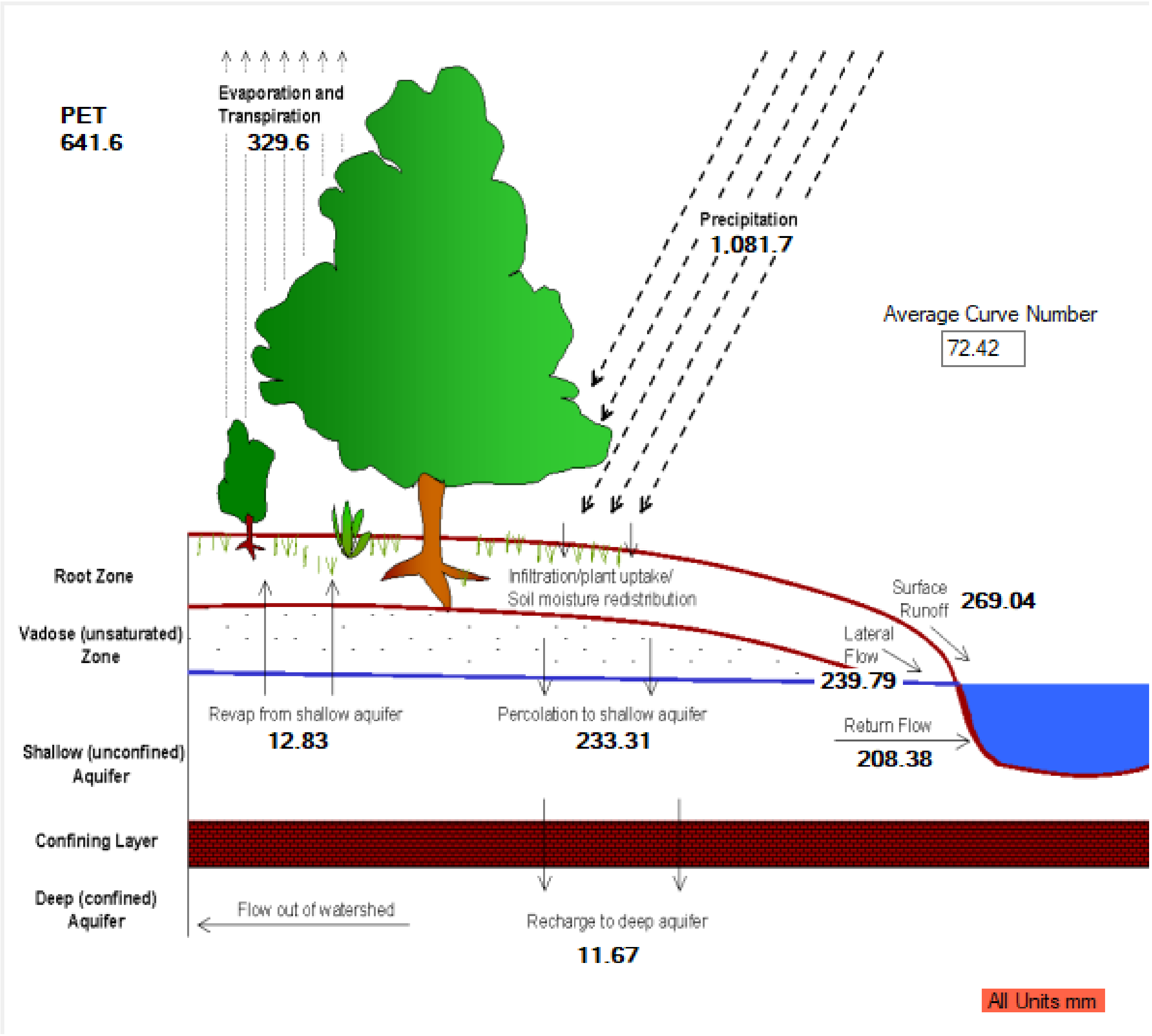

Fig. 6. 6 **Various components of water balance at the Henval catchment**

The ratios among different water balance components of the Henval watershed are given in Table 6.2. It can be seen from the table that the catchment flows heavily depend on the baseflow in the form of springs. The lower values of streamflow to precipitation ratio indicates that the hydrological responses of the catchment are prolonged, despite the highly sloppy landscape. The can be attributed to the 76% of land cover is, and the average curve number is found to be 72.42.

Table 6. 2 Ratios of water balance components

S. No.	Particular Ratio	Value
1	Streamflow/Precipitation	0.66
2	Base flow/ Total flow	0.62
3	Surface runoff/ Total flow	0.38
4	Percolation/Precipitation	0.22
5	Deep recharge/Precipitation	0.01
6	Evapotranspiration/Precipitation	0.30

CHAPTER 07: SUMMARY AND CONCLUSIONS

The Himalayan basins are very critical to the water security of the northern Indian plains. Few studies dedicated to understanding the interaction of hydrological and climatological variable in the Himalayan environment have been reported. Himalaya is a data-sparse region leading to lack of in-depth understanding of the various physical processes. The scanty availability of hydro-meteorological database is further accelerating the complexity to understand the Himalayan hydrology and its interaction with other processes such as orographic forcing. Thorough understanding of the coupling between surface hydrologic systems and the overlying atmospheric system under orographic moisture flow is essential to address this question. An experimental research station with state-of-the-art instrumentation with a long-term research framework is established at the lesser Himalayan region to gain an understanding of these issues. This research station is aimed to produce baseline data of weather and hydrology of the lesser Himalayan mountains leading to a better understanding of climate-hydrology interaction under changing climate of the region. Since the Himalayan tributaries play an essential role in maintaining the hydrologic regime of the River Ganges; sustained research from this experimental station is likely to help in managing the water resources of river Ganges and its Himalayan tributaries better under the climate change scenario.

National Institute of Hydrology has initiated this project in the year 2016 to develop a better understanding of climate-hydrology interaction in the lesser Himalayan experimental catchment with an area of 102km^2. This experimental catchment is set-up in the Upper Ganga basin near Chamba town in Tehri-Garhwal (Uttarakhand). Due to the importance of the project, various sponsoring agencies, including DST and MOES, have supported the project to strengthen the monitoring facilities in the watershed.

All the instrumentation envisaged towards establishing a classical hydro-meteorological field observatory in the Lesser Himalayan environment has been completed in this first phase of the Project-Henval. The data collected from the AWS and other sensors have been analyzed, and results are described.

This first phase of the study was focused on monitoring evapotranspiration (ET) by using the latest available technology of eddy covariance tower and ET modelling for the lesser Himalayan region. The ET estimated using the energy balance method from the flux tower was compared with the ET estimated by using the other methods like Penman-Monteith equation, remote sensing/ SEBAL, and Pan. The daily reference evapotranspiration for the period Mar-2016 and Dec-2019 estimated using temperature-based (Hargreaves-Samani & Blaney-Criddle) and radiation-based (Priestley-Taylor & Makkink) methods have been compared with renowned Penman-Monteith (PM) method (FAO-56). Using the statistical indices like $R^{2,}$ it has been observed that the radiation-based methods perform comparatively well than temperature-based methods. Remote sensing-based evapotranspiration estimation method Surface Energy Balance Algorithm for Land (SEBAL) is being tested for the experimental catchment. SEBAL model estimates actual ET by solving the terms of the surface energy balance derived from the visible, near-IR, and thermal-IR bands of the electromagnetic spectrum. LANDSAT 8 data used in determining land surface temperature (LST) and the normalized difference vegetative index (NDVI).Mapping Evapotranspiration at high Resolution with Internalized Calibration (METRIC) is a remote sensing-based model similar to SEBAL was also attempted for the Henval catchment. It estimates ET as a residual of the surface energy balance to produce ET information over a larger area of interest. One of the latest and direct measurement technique of ET, namely Eddy Covariance (EC) flux analysis was also carried out to estimate the actual ET.

The catchment response to the various hydro-climatic forcing within the lesser Himalayan catchment was evaluated by the water balance study done through the hydrological modelling using Soil and Water Assessment Tool (SWAT) model. Simulations of the streamflows at Devnagar gauging site has been carried out by SWAT model. The modelling results show that the model is underestimating the flows; this may be attributed to the slow hydrological response of the catchment as well as fine-tuning of the model parameters. The results can be improved by incorporating the catchment specific data such as intensive soil parametrization. These need to be done in order to achieve better model efficacy.

The main focus of the project was to establish a state-of-art field hydro-meteorological observatory and ET estimations with various empirical methods and actual field measurements. In the next phase, the main focus shall be on the hydrological modelling and studies of the interaction between the various observed variables.

REFERENCES

Allen RG, Pereira LS, Raes D, Smith M. 1998. Crop evapotranspiration: guidelines for computing crop water requirements. Irrigation and Drainage Paper No. 56. Rome (Italy): Food and Agriculture Organization of the United Nations.

Bhutiyani, M. R., Kale, V. S. and Pawar, N. J.: Climate change and the precipitation variations in the northwestern Himalaya: 1866-2006, Int. Jour. Climatol., 30,535-548 doi: 10.1002/joc.1920,2010.

Bhutiyani, M. R., Kale,V. S. and Pawar, N. J.: Long-term trends in maximum, minimum and mean annual air temperatures across the Northwestern Himalaya during the twentieth century, Climatic Change, 85,159-177, doi: 10.1007/s10584-006-9196-1, 2007.

Hargreaves GH, Samani ZA. 1982. Estimating potential evapotranspiration. J Irrig Drain Div. 108:225–230.

Hargreaves GH, Samani ZA. 1985. Reference crop evapotranspiration from temperature. ApplEng Agric.1:96–99.

Hui D, Wan S, Su B et al. (2003) Gap-filling missing data in eddy covariance measurements by multiple imputation (MI) for annual estimations. Agricultural and Forest Meteorology, 121,93–111.

J. J Mcdonnell, M Sivapalan, K Vache, S Dunn, G Grant, R Haggerty, C Hinz, R Hooper, J Kirchner, M. L Roderick, J Selker, M Weiler. (2007). Moving beyond Heterogeneity and Process Complexity: A new Vision for Watershed Hydrology. Water Resources Research

J. W Kirchner. (2006) Getting the Right Answers for the Right Reasons: Linking Measurements, Analyses, and Models to Advance the Science of Hydrology. Water Resources Research

M Sivapalan, Pattern. (2005) Process and Function: Elements of a Unified Theory of Hydrology at the Catchment Scale. In: Anderson MG (ed.) Encyclopedia of Hydrological Science. John Wiley & Sons

Makkink, G. F.: 1957, 'Testing the Penman Formula by Means of Lysimeters', J. Instit. Water Engineers 11, 277–288.

Neitsch,S.L., Arnold, J.G., Kiniry, J.R., and Williams, J.R. Soil and Water Assessment Tool Theoretical Documentation Version 2005. Grassland, Soil and Water Research Laboratory, Agricultural Research Service 808 East Blackland Road, Temple, Texas 76502; Blackland Research Centre, Texas Agricultural Experiment Station 720,East Blackland, Texas USA

Oncley, S., Foken, T., Vogt, R., Bernhofer, C., Kohsiek, W., Liu, H., &Weidinger, T. (2002, May). The energy balance experiment EBEX-2000. In 15th Conference on Boundary Layer and Turbulence

Penman, H.L., 1948. Natural evaporation from open water, bare soil and grass. Proc. R. Soc. London Ser. A., 193: 120--145.

Priestley, C.H.B. and Taylor, R.J., 1972. On the assessment of surface heat flux and evaporation using large-scale parameters. Mon. Weather Rev., 106: 81--92.

Singh, V. P.: 1989, Hydrologic Systems, Vol. II, Watershed Modelling, Prentice-Hall, Inc.

T. H. Skaggs, R. G. Anderson, J. G. Alfieri, T. M. Scanlon, W. P. Kustas (2018). Fluxpart: Open source software for partitioning carbon dioxide and water vapor fluxes. Agricultural and Forest Meteorology 253–254:218–224, doi:10.1016/j.agrformet.2018.02.019.

T. M. Scanlon, W. P. Kustas. 2010. Partitioning carbon dioxide and water vapor fluxes using correalation analysis. Agricultural and Forest Meteorology 150(1):89–99, doi:10.1016/j.agrformet.2009.09.005.

Thayyen, R. J., &Dimri, A. P. (2014). Factors controlling Slope Environmental Lapse Rate (SELR) of temperature in the monsoon and cold-arid glacio-hydrological regimes of the Himalaya. The Cryosphere Discussions, 8(6), 5645-5686, doi:10.5194/tcd-8-5645-2014.

Wei-ZuGu, Jiu-Fu Liu, Jia-Ju Lu and Jay Frentress (2013). Current Challenges in Experimental Watershed Hydrology, Current Perspectives in Contaminant Hydrology and Water Resources Sustainability, Dr. Paul Bradley (Ed.), ISBN: 978-953-51-1046-0.

*****

STUDY TEAM

Director	:	Dr J. V. Tyagi
Head	:	Dr Sanjay K. Jain, Scientist 'G'
Investigators	:	Dr Manish K. Nema, Scientist 'D' (PI)
		Dr Sharad K. Jain, Ex. Director, NIH
		Dr Sanjay K. Jain, Scientist 'G'
		Dr Renoj J. Thayyen, Scientist 'E'
		Dr P. K. Mishra, Scientist 'C'
		Mr Hitesh P. Thakur, JRF